Behaviour of Perovskite Solar Cells Under Reverse Bias and Interface Engineering for Efficient and Stable Solar Cells

Keqing Huang

February 2024

A thesis submitted for the degree of
Doctor of Philosophy
of The Australian National University

© Copyright by Keqing Huang, 2024
All Rights Reserved

Declaration

I certify that this thesis does not incorporate without acknowledgement any material previously submitted for a degree or diploma in any university, and that, to the best of my knowledge, it does not contain any material previously published or written by another person except where due reference is made in the text. The work in this thesis is my own, except for the contributions made by others as described in the Acknowledgements.

Keqing Huang

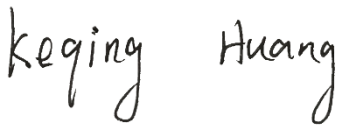

February 2024

Acknowledgements

Due to the COVID-19 pandemic and travel restrictions, I was trapped in the mainland of China until October 2021. This period was marked by difficulties and uncertainties, but the unwavering support from those around me transformed the situation. Therefore, I extend my heartfelt appreciation to my supervisors, friends, and family members.

Firstly, I would like to express my great gratitude to Prof. Klaus Weber. The research direction, analysis and discussion of experimental results, and the research articles are supervised by Klaus Weber. Additionally, he gave me invaluable assistance and confidence to let me go ahead during the covid epidemic and travel restrictions, so my sincere gratitude goes out to him. During the remote enrolment period, Prof. Junliang Yang not only offered me an experimental platform enabling the continuation of my research but also provided significant guidance and help. I express my gratitude to Junliang Yang. Dr. The Duong played a vital role in lab training, characterization, manuscript preparation, and revision, offering timely and enthusiastic assistance. Special thanks to The Duong. I extend my appreciation to Prof. Kylie R. Catchpole, Assoc. Prof. Thomas P. White, and Dr. Heping Shen for their selfless contributions to experimental characterization and result analysis.

I also want to acknowledge my research collaborators, including Assoc. Prof. Yuxia Duan, Xiangxiang Feng, Weiqi Li, Caoyu Long, and Ning Wang for their great contributions in acquiring experimental data, analysing experimental results, and writing and revising the manuscript. Dr. Olivier Lee Cheong Lem, Dr. Anh Dinh Bui, Wenzhong Ji, Dr. Azul Osorio Mayon, and Thanh Tran-Phu provided significant support for characterization, which has enabled the research to be carried out successfully. Thanks to Dr. Hengyue Li, Grace Dansoa Tabi, and Lichun Chang for revising the manuscript, which is of great help in improving the manuscript. Also, I would like to express my gratitude to my friends including Wei Wang, Xuesi Liu, Zhongshu Yang, Yihui Hou, Dr. Wensheng Liang, Dr. Leiping Duan, Erming Feng,

Yang Ding, Caoyu Long, Yuanji Gao, and Dang-Thuan Nguyen for their enduring companionship and support throughout these years.

Finally, I express deep gratitude to my family members for their continuous support. It is their patience and encouragement that provided me with the confidence to persist in my studies and personal development. Thanks to everyone who has helped or shared good memories with me.

Abstract

Perovskites have drawn tremendous attention due to their excellent optoelectronic properties, low-cost and versatile solution-processibility. The power conversion efficiency of single-junction perovskite solar cells (PSCs) has reached 26.1%, showing promising prospects for commercialization. Herein, we mainly focus on the behaviour of PSCs under reverse bias and the interface engineering for efficient and stable PSCs. The results are summarized as follows:

(1) An in-situ temperature and current measurement technique was developed. Intriguingly, some hot spots were observed and then quickly disappeared in the reverse biased PSCs, along with the simultaneous increase in the current and local temperature. Also, the potential mechanism has been revealed and analysed. An abnormal bulge in the perovskite film was found at the hot spot. Accordingly, the appearance and disappearance of hot spots were perfectly explained by band bending and tunnelling current caused by ion accumulation. Additionally, statistical analysis suggested that sparkling hot spots were related to reverse voltage and efficiencies of PSCs. These results are significant as they provide insights into the dynamic behaviour of PSCs under reverse bias, which is crucial for improving device stability. Besides, the technology proposed here shows promise for the inspection of perovskite modules.

(2) It is found that the device performance can be improved by manipulating the migration of iodine ions via reverse-biasing, for example, at -0.4 V for 3 min in dark. Characterizations suggest that reverse bias can increase the charge recombination resistance, improve carrier transport, and enhance built-in electric field. Iodine ions including iodine interstitials in perovskites are confirmed to migrate and accumulate at the tin dioxide (SnO_2)/perovskite interface under reverse-biasing, which fill iodine vacancies at the interface and interact with SnO_2. First-principles calculations suggest that the SnO_2/perovskite interface with less iodine vacancies has a stronger interaction and higher charge transfer, leading to larger built-in electric field and improved charge transport. Iodine ions that may pass through the SnO_2/perovskite interface are also confirmed to be able to interact with Sn^{4+} and passivate oxygen vacancies on the surface

of SnO_2. Consequently, an efficiency of 23.48% with the open-circuit voltage of 1.16 V is achieved for PSCs with reverse-biasing. The improvement highlights the potential of reverse-biasing as a practical technique to enhance the efficiency, and even stability of PSCs by optimizing ion migration and interfacial properties.

(3) Due to the limited interface contact and weak interfacial interaction, planar heterojunction PSCs have space for further improvement. Herein, a structural and chemical crosslinking interface is proposed and constructed by introducing an extra layer, which blends SnO_2 nanoparticles with chloride salts. Since the incorporated materials can be dissolved during the fabrication of perovskite, the quality of perovskite films was improved, leading to larger grain size and reduced trap-state density. Also, more chloride ions at the SnO_2/perovskite interface were observed and the interaction between Cl^- and Sn^{4+} was confirmed. It results in more pronounced n-type SnO_2 with better conductivity and deeper conduction bands, leading to preferable energy level alignment between SnO_2 and perovskite. Consequently, the open-circuit voltage and fill factor of the devices increased, and target cells presented better stability, retaining 98% of initial efficiencies after more than 10000 h storage in dry air (5% relative humidity) and maintaining 85.50% of the initial efficiency after 1000 h of operation under light. This strategy enabled the achievement of 25.28% efficiency with a low bandgap (1.53 eV) perovskite composition, and it has been confirmed to be universal when other related materials are utilized. These results offer a robust approach to enhance both the performance and stability of PSCs, making them more viable for commercial applications.

Table of Contents

Acknowledgements i
Abstract iii
Introduction 1
1 Perovskite solar cells 4
1.1 Global warming and renewable energy 4
1.2 Development of perovskite solar cells 7
1.2.1 Perovskite materials 7
1.2.2 The emergence of perovskite solar cells 9
1.2.3 Structure and charge transport layers of perovskite solar cells 9
1.2.4 Application of perovskites in tandem solar cells 11
1.3 The stimuli inducing degradation of perovskite solar cells 12
1.3.1 Humidity 13
1.3.2 Illumination 13
1.3.3 Heat 14
1.3.4 High-energy radiation 14
1.3.5 Strain 15
1.3.6 Reverse bias 16
2 Sparkling hot spots in perovskite solar cells under reverse bias 20
2.1 Introduction 20
2.2 Solar cell fabrication and characterization 21
2.3 Results and discussion 22
2.4 Conclusion 29
3 Manipulating the migration of iodine ions via reverse-biasing for boosting photovoltaic performance of perovskite solar cells 31
3.1 Experimental section 31
3.1.1 Materials 31
3.1.2 Device fabrication 32
3.1.3 Reverse-biasing experiment 33
3.1.4 Characterization 33
3.1.5 Computational methods 34

3.1.6 Statistical analysis 34
3.2 Results and discussion 35
3.3 Conclusion 47
4 Universal strategy with structural and chemical crosslinking interface for efficient and stable perovskite solar cells 48
4.1 Introduction 48
4.2 Experimental section 50
4.2.1 Materials 50
4.2.2 Device fabrication 50
4.2.3 Characterization 53
4.2.4 Statistical analysis 54
4.3 Results and discussion 55
4.4 Conclusion 70
5 Summary and Outlook 71
5.1 Summary 71
5.1.1 Sparkling hot spots in perovskite solar cells under reverse bias 71
5.1.2 Manipulating the migration of iodine ions via reverse-biasing for boosting photovoltaic performance of perovskite solar cells 71
5.1.3 Universal strategy with structural and chemical crosslinking interface for efficient and stable perovskite solar cells 72
5.2 Outlook 72
Bibliography 76
Achievements 95

Introduction

Thesis motivation

Up to date, the certified efficiency of single-junction perovskite solar cells (PSCs) has exceeded 26%. However, the application of perovskite solar panels in the fields still faces some problems, including the stability under reverse bias. The magnitude of reverse bias and the duration of reverse bias treatment can affect the behaviour of PSCs. Generally, it leads to the degradation of PSCs, including the formation of highly conductive shunts, ion migration within the cells, and degradation of perovskite absorbers. As a consequence, the device performance will decrease after reverse bias treatment and current-voltage curves turn to be S-shape or linear. Moreover, reverse bias is directly applied to the complete PSCs, making it difficult to explore the mechanism behind. Therefore, further research is needed to investigate the behaviour of PSCs under reverse bias. This is of great significance for the application of perovskite modules.

Apart from that, planar heterojunctions are widely used in highly efficient single-junction PSCs. However, the shortcomings of planar structures, including limited contact area and weak interface interaction, have not obtained enough attention. Thus, it is necessary to tailor the interfaces in PSCs to enhance interface stability and cell stability.

Thesis outline

In Chapter 1 shows the necessity of developing technologies related to renewable energy, especially solar photovoltaics. An overview of perovskite materials, development of charge transport layers, the structure of perovskite solar cells, and perovskite/silicon tandem solar cells has been provided. Finally, stimuli leading to the

degradation of perovskites and perovskite solar cells have been discussed, including humidity, illumination, heat, high-energy radiation, strain, and reverse bias.

In Chapter 2, sparkling hot spots are found in reverse biased PSCs. During the measurement, current and temperature change in PSCs under reverse bias are measured by a non-destructive and in-situ testing system containing infrared micro-thermography and digital source meter. The sparkling hot spots in PSCs under reverse bias are investigated by using a layer-by-layer exfoliation method and characterization such as optical microscopy, step profiler, and energy dispersive X-ray (EDX) analysis. Bulges are found in perovskite films and PbI_2 films, which accounts for the sparkling hot spots. The mechanism of sparkling hot spots is revealed by the drift-diffusion model and accumulated ions at the interface between perovskites and the hole transport layer. The relationship between device performance and sparkling hot spots under reverse bias is discussed.

In Chapter 3, reversible enhancement in device performance is found by precise control of reverse bias and loading time of reverse bias. Characterization results indicate that reverse bias treatment improves the charge carrier dynamics in PSCs. Further results and first-principles calculations suggest that the improvement in device performance is attributed to iodine ion migration caused by reverse bias, which can fill the iodine vacancies at the SnO_2/perovskite interface. The influence of iodine ions on SnO_2 layers is also investigated by first-principles calculations, suggesting that iodine ions will be attached to the surface of SnO_2 nanoparticles and passivate the oxygen vacancies of SnO_2.

In Chapter 4, a structural and chemical crosslinking interface between SnO_2 and perovskite is proposed, which is constructed by introducing an additional layer containing SnO_2 nanoparticles and chloride salt (namely methylenediammonium dichloride). This strategy enables the achievement of efficient PSCs with over 10000 h self-stability (kept under dark conditions and dry air with ~5% relative humidity). Results suggest that the introduced chloride salt not only affects the SnO_2 layer, but also improves the perovskite layer. To be specific, our proposed strategy results in enhanced conductivity of SnO_2 films, larger perovskite grain size, and better energy level alignment between SnO_2 and perovskite. Other chloride salts (including methylammonium chloride, caesium chloride, and 4-methylphenethylammonium

chloride) are utilized along with the strategy, confirming that the structural and chemical crosslinking interface is universal for the improvement of cell performance.

In Chapter 5, we summarize the phenomena we found, characterization results, and the change in device performance. Additionally, we have given some suggestions in terms of these two research directions in the thesis, namely reverse biased PSCs and interface engineering, to further deepen our existing research knowledge. Finally, an outlook focusing on three key issues for perovskite solar cells has been provided, including degradation of perovskites and PSCs induced by external stimuli, large-area printing of PSCs, and toxicity of lead-based perovskite (or the oxidation of divalent tin).

Work contributions

Chapter 2 - Keqing Huang, Weiqi Li, Jianhui Chang, and Caiqi Hu were involved in device fabrication and characterization. Hai Zhang, Xavier Maldague, and Yuxia Duan provided characterization technique. Keqing Huang, Weiqi Li, Caiqi Hu, Yuxia Duan, and Junliang Yang contributed to the result analysis. Keqing Huang and Weiqi Li wrote the draft of the manuscript. All co-authors were involved in the revision of the manuscript. The entire work was supervised by Yuxia Duan and Junliang Yang.

Chapter 3 - Keqing Huang conceived and designed the overall experiments. Xiangxiang Feng and Biao Liu contributed to the first-principles calculations. Jiangjian Shi and Qingbo Meng were involved in carbon electrode-based PSCs. Keqing Huang, Xiangxiang Feng, Klaus Weber, The Duong, and Junliang Yang contributed to the result analysis. Keqing Huang and Xiangxiang Feng wrote the draft of the manuscript. All co-authors were involved in the revision of the manuscript. The entire work was supervised by Klaus Weber, The Duong, and Junliang Yang.

Chapter 4 - Keqing Huang conceived and designed the overall experiments. Keqing Huang, Yihui Hou, Wenzhong Ji, Thanh Tran-Phu, Anh Dinh Bui, Azul Osorio Mayon, Wei Wang, Olivier Lee Cheong Lem, and The Duong were involved in characterization. Keqing Huang, Lichun Chang, Junliang Yang, Kylie R. Catchpole, Klaus Weber, and The Duong contributed to the result analysis. Keqing Huang wrote the draft of the manuscript. The revision of the manuscript was supported by all co-authors. The entire work was supervised by Klaus Weber and The Duong.

CHAPTER 1

1 Perovskite solar cells

1.1 Global warming and renewable energy

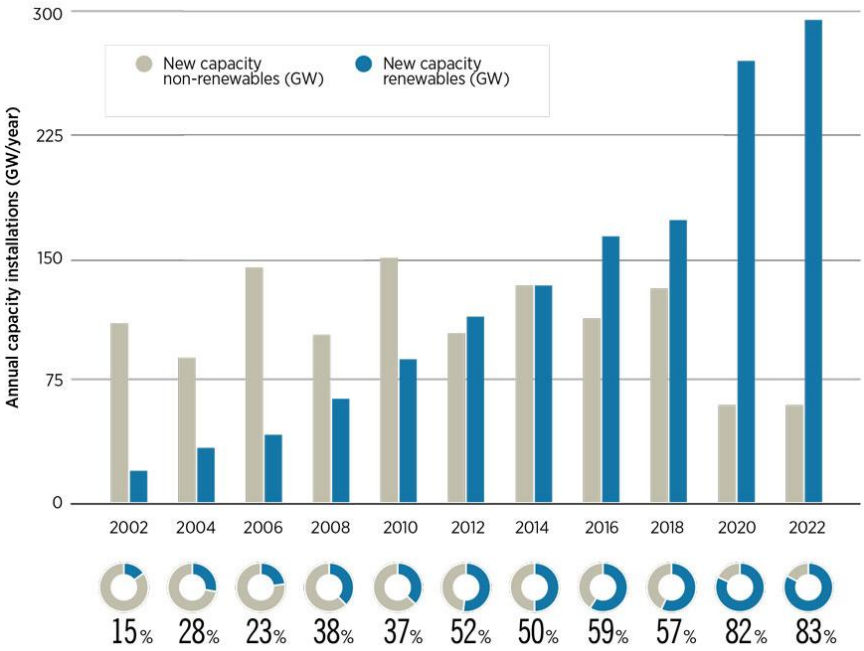

Figure 1.1. *Annual power capacity expansion, 2002-2022. The result is from World Energy Transitions Outlook 2023.*[2]

Due to the usage of fossil fuels, global warming and environmental pollution have become severe. The Paris Agreement, a legally binding international treaty on climate change, was adopted by 196 Parties at the United Nations Climate Change Conference in 2015. It aims to bring global warming well below 2 ºC and preferably to 1.5 ºC compared to pre-industrial levels.[1] Accordingly, greenhouse gas emissions must peak before 2025 and decline 43% by 2030. Cutting carbon dioxide (CO_2) emissions by around 37 gigatonnes from 2022 levels and achieving net-zero emissions in the energy sector by 2050 are needed to limit global warming to 1.5 °C, according to World Energy

Transitions Outlook 2023.[2] It requires energy transition from fossil fuel-based energy to renewable energy, including solar energy, wind power, hydropower, geothermal energy, bioenergy and so on.

The energy sector has made significant strides in installing renewable capacity and generation. Renewables constituted 83% of the capacity additions and a 40% share of installed power generation capacity in 2022, resulting from the addition of 295 gigawatts (GW) of renewables (Figure 1.1). This marked the most significant annual increase in renewable energy capacity to date. Solar photovoltaic installations experienced the most rapid growth among renewable technologies, witnessing a twenty-sixfold increase over the 13 years from 2010 to 2022.[2] By the end of 2022, the cumulative installed capacity of solar photovoltaics globally reached 1,047 GW. Notably, 191 GW was added in 2022 alone, with Asia accounting for 59% of these installations.[2]

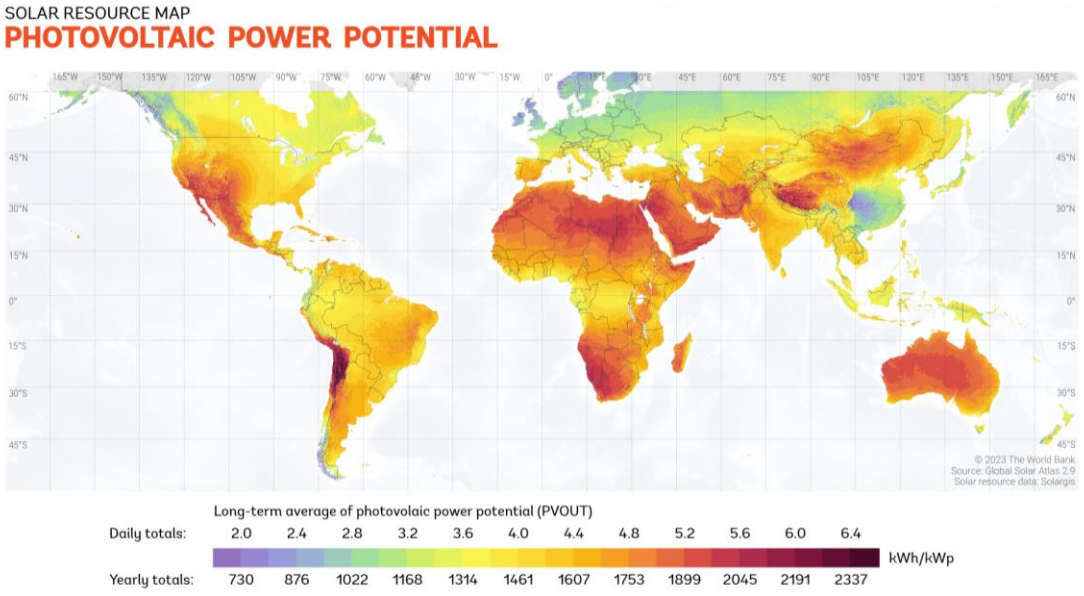

Figure 1.2. *Global distribution of photovoltaic power potential. The map is from 2020 The World Bank, Source: Global Solar Atlas 2.0, Solar resource data: Solargis.*[3]

Solar energy has become the most promising renewable energy due to its wide distribution, as shown in Figure 1.2.[3] It is estimated that the total energy flow of solar radiation is 4×10^{26} J/s, with approximately 1.8×10^{17} J/s transported to the Earth. Areas with an annual direct normal irradiation of more than 1,800 - 2,000 kWh/m²/a are generally considered as suitable for concentrated solar thermal technologies, and the value for solar photovoltaics should be much lower.[4] It is estimated that electricity

will account for over 50% of total final energy consumption and become the main energy carrier by 2050.[2] The direct integration of solar photovoltaics into buildings and end-use sectors offers greater advantages, significantly reducing energy losses caused by transportation.

Many solar cell technology routes have been developed with different active layers, including crystalline silicon, cadmium telluride (CdTe), gallium arsenide (GaAs), copper indium gallium selenide (CIGS), dye-sensitized, and organic solar cells. Generally, they can be classified into three generations. The first generation includes traditional solar cells made from materials like GaAs and crystalline silicon, such as monocrystalline and polycrystalline silicon. Second generation solar cells (thin-film solar cells) use semiconductor layers like amorphous silicon (a-Si), CdTe, and CIGS. These cells are valued for their lightweight, flexibility, and potential cost advantages over crystalline silicon. Third generation solar cells are based on photovoltaic technologies with new chemical compounds, including organic photovoltaics, PSCs, and dye-sensitized solar cells. Each generation has its own advantages and challenges, with ongoing research and development to improve efficiency, reduce costs, and expand the applications of solar photovoltaics. The silicon solar cell technology is currently dominant in the solar photovoltaics with 95% of market share.[5] The record efficiency of silicon solar cell has reached 27.1%.[6,7] However, silicon solar cells require an extremely high purity for the silicon absorber, and the manufacturing process involves energy-intensive steps at temperature of ~1000 °C.[8-10] Besides, silicon has a lower absorption coefficient (10^3-10^5 cm^{-1}) at visible light range, as compared to the absorbers (10^5-10^6 cm^{-1}) of thin-film solar cells.[11] A thick silicon absorber (> 100 μm) is typically required to capture incident light effectively,[12,13] leading to heightened demand for raw materials and an increase in the weight of silicon solar panels. Therefore, it is necessary to explore and develop alternative solar cells that are both cost-effective and highly efficient.

Perovskite solar cells were first introduced in 2009, experiencing a remarkable surge in power conversion efficiency (PCE) from the initial 3.8% to the current 26.1%.[6] PSCs can be solution-processed and the required thickness of the perovskite film for PSCs is only 400-800 nm. Additionally, the adjustable bandgap of perovskite makes it compatible with silicon in tandem solar cells. In these cells, sunlight can be utilized more efficiently, resulting in a higher PCE. This means more energy output per surface area (W m^{-2}), providing a more effective strategy for reducing the cost of photovoltaic

electricity than merely lowering the cost of the photovoltaic cells. Nowadays, PSCs are attracting more and more attention in academic community, and the industry with many companies is in progress to commercialize the technology.

1.2 Development of perovskite solar cells

1.2.1 Perovskite materials

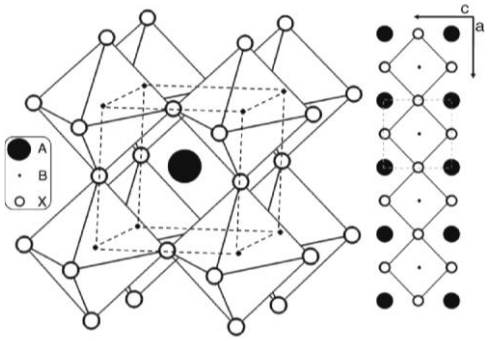

Figure 1.3. *Schematic of the commonly used perovskite structure ABX_3 ($A = CH_3NH_3^+$, $HC(NH_2)_2^+$, Cs^+; $B = Pb^{2+}$, Sn^{2+}; $X = I^-$, Cl^-, Br^-). The right image is the two-dimensional schematic of perovskite structure.*[14]

Perovskites are hybrid organic-inorganic metal halide materials (general formula was denoted as ABX_3), and their crystal structure is shown in Figure 1.3.[14] The B-site ions and X-site ions form octahedral structures, while the A-site ions fill the gaps of these octahedral structures. The A-site can be methylamine ion ($CH_3NH_3^+$), formamidine ion ($HC(NH_2)_2^+$), and caesium ion (Cs^+); the B-site ions mainly include Pb^{2+}or Sn^{2+}; the X-site is mainly occupied by halogen ions such as I^-, Br^-, and Cl^-. The tolerance factor determines the structure of perovskites, and it can be obtained by Equation (1.1):

$$t = \frac{R_A + R_X}{\sqrt{2}(R_B + R_X)} \quad (1.1)$$

where R is the ionic radius of the corresponding ion, and t is the tolerance factor. The tolerance factors between 0.8-1.0 are generally beneficial to the stability of perovskite crystal structure.[15]

Perovskite materials have many advantages, such as high absorption coefficient ($\sim 10^5$ cm^{-1}),[11] long electron and hole-diffusion length (up to 1 mm),[16] low exciton binding energy (~16 meV),[17] and low-cost solution processibility.[18,19]

Methylammonium lead triiodide ($MAPbI_3$) was the most commonly used material for the active layer of PSCs from the beginning, due to its simplicity and stable performance. Given the lower and more suitable bandgap of formamidinium lead iodide ($FAPbI_3$) perovskite (1.47 eV for $FAPbI_3$ versus 1.55 eV for $MAPbI_3$),[19] $FAPbI_3$ can be used to extend the light absorption range and produce higher efficiency according to the Shockley−Queisser limit of *p-n* junction solar cells.[20] However, the black phase α-$FAPbI_3$ is unstable and transitions to yellow phase at ambient temperature. Therefore, triple cations including MA^+, FA^+, and Cs^+ can be used to stabilize perovskite crystal structure and are widely used for high-performance PSCs. Monolithic tandem solar cells require current matching of the sub-cells to achieve the optimal performance,[21,22] and the bandgap of the top cell can be tuned via compositional engineering of the perovskite. For example, more Br^- anions and Cs^+ cations will be mixed into the X-site and A-site respectively, to achieve wider and more suitable bandgap of perovskite. However, wider bandgap perovskite suffers from light-induced halide phase segregation, in which Br-rich and I-rich phases in perovskites can form under continuous illumination.[23-25]

Apart from the hybrid organic-inorganic perovskites, all-inorganic perovskites, such as $CsPbI_3$, $CsPbI_2Br$, and $CsPbBr_3$, possess excellent thermal stability.[26] However, as the content of iodine ions in perovskites increases, perovskites can transition from cubic structure (black phase) to orthorhombic nonperovskite structure (yellow phase),[26] especially under ambient air. When all A-site ions are occupied by organic spacer cations such as phenylethylammonium (PEA^+) and butylammonium (BA^+), two-dimensional (2D) layered perovskites can be obtained. According to the structure of 2D perovskites, they can be divided into Ruddlesden-Popper perovskites and Dion-Jacobson perovskites.[27] Due to the hydrophobicity of organic spacer cations, these perovskites generally have better environmental stability. However, the steric effect and intermolecular interactions affect the crystallization process and charge transport properties of perovskites,[28-30] so the performance of 2D perovskite solar cells is limited. Nonetheless, the 2D perovskites can be used to passivate defects on the surface of 3D perovskites to enhance the photovoltaic performance and stability of PSCs.

With the development of hole transport layers (HTL) and electron transport layers (ETL), the efficiency of PSCs has surpassed those of dye-sensitized solar cells, organic solar cells, and multicrystalline silicon solar cells,[6] showing broad application prospects. Furthermore, perovskites have shown good performance in photodetector,

light-emitting diodes, X-ray detectors, and gamma-ray spectrum detectors, becoming a research hotspot in the interdisciplinary fields of optoelectronic physics, material science, and chemistry.

1.2.2 The emergence of perovskite solar cells

The application of perovskites in solar cells has been over a decade. Initially, Miyasaka and co-workers first used perovskite materials ($CN_3NH_3PbI_3$, $CN_3NH_3PbBr_3$) as sensitizers for dye-sensitized photovoltaic cells in 2009 and achieved an efficiency of 3.8%.[31] In 2011, Park and co-workers deposited perovskite materials in the form of quantum dots (size 2-3 nm) on nanocrystalline TiO_2 surface and achieved an efficiency of 6.54%.[18] The above studies all used the liquid electrolyte, which gradually dissolves the perovskite materials especially under illumination, resulting in poor device stability. In 2012, Park and co-workers introduced 2,2′,7,7′-tetrakis(N,N-dipmethoxyphenylamine)-9,9′-spirobifluorene (spiro-OMeTAD) as the HTL and obtained all-solid-state perovskite solar cells.[32] During the same period, Snaith and co-workers reported solution process to prepare $CH_3NH_3PbI_{3-x}Cl_x$ perovskite material, which boosted the efficiency of PSCs to 10.9%.[14] In the initial research, mesoporous TiO_2 was widely used to structure the perovskite absorber, but Snaith and co-workers reported that the complex nanostructure is not necessary to achieve high efficiencies with perovskites.[33] Accordingly, planar heterojunction PSCs were obtained in 2013. Perovskite solar cells were picked as one of "Top 10 Breakthrough of the year 2013" by journal of *Science*,[34] and then PSCs developed rapidly.

1.2.3 Structure and charge transport layers of perovskite solar cells

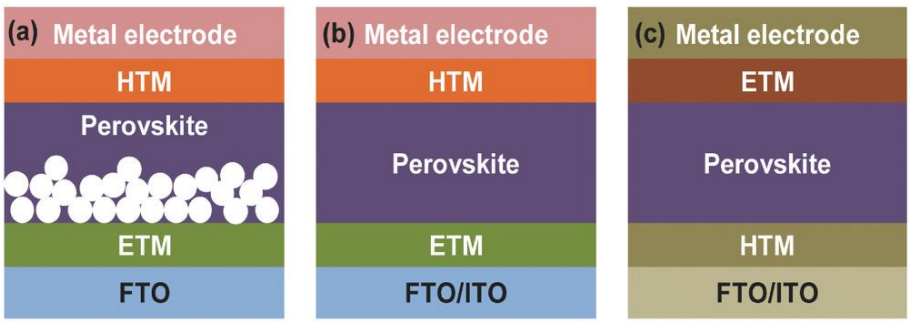

Figure 1.4. *Schematic of PSC structures: (a) mesoporous, (b) planar n-i-p (regular), and (c) planar p-i-n (inverted) structure.*[36]

After the development of fifteen years, the efficiency of perovskite solar cells has reached 26.1%, which is comparable to the record efficiency (27.1%) of silicon heterojunction solar cells.[6] With the optimization of perovskite materials, as well as the design of electron and hole transport layers, the cell configuration is divided into planar and mesoporous structures (Figure 1.4a,b). Mesoporous TiO_2 increases the contact area between the perovskite and the ETL, thereby increasing the extraction and transport of electrons in mesoporous PSCs. Also, other metal oxides with mesoscopic nanostructures including Al_2O_3 and ZrO_2 can be used to support perovskite materials.[35,36] However, mesoporous TiO_2 generally requires a high-temperature annealing process,[37,38] so other charge transport layers with low-temperature annealing have been introduced. Accordingly, mesoporous structure can be removed from PSCs and planar heterojunction PSCs were achieved. Planar PSCs exhibit more advantages in low-cost fabrication and flexible photovoltaics,[39,40] due to a simpler structure and versatile fabrication routes. The works in this thesis are based on planar heterojunction structure, and the behaviour of n-i-p single-junction PSCs under reverse bias are investigated. Additionally, a universal strategy with structural and chemical crosslinking interface is proposed to improve the device performance and stability.

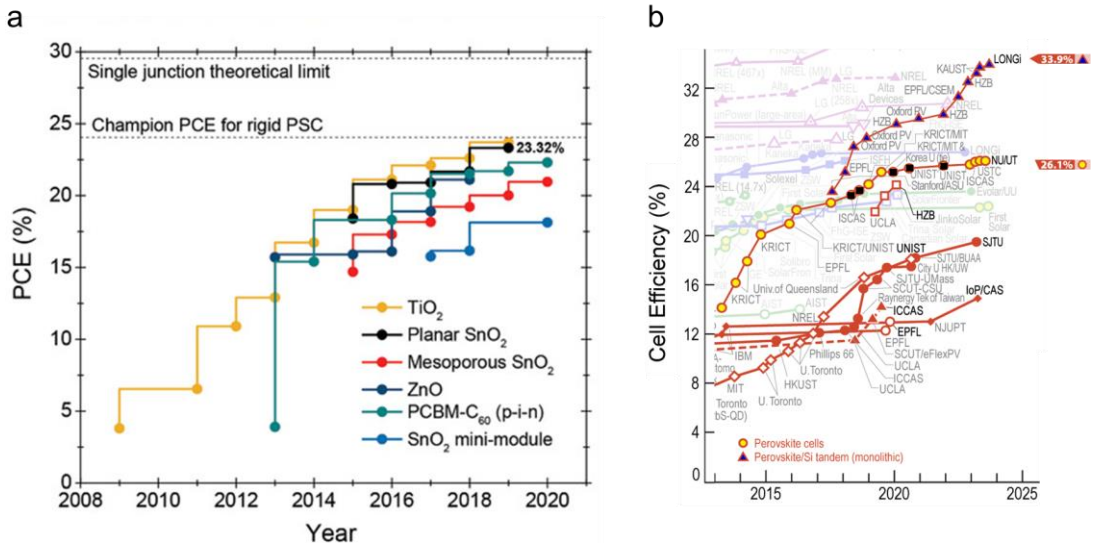

Figure 1.5. *(a) Evolution of PCE values for PSCs using different electron transport materials;[47] (b) Best Research-Cell Efficiency Chart from National Renewable Energy Laboratory (The black dots on perovskite cells indicate that the specific perovskite cell was based on SnO_2; the latest four points with certified efficiency for perovskite solar cells have not been published).[6]*

High transparency is required for the charge transport layer close to window electrode, so that more incident light can reach the perovskite absorber and the optical

loss of PSCs is reduced. The process to fabricate the charge transport layer, particularly with solution, must be compatible with perovskite materials to ensure no damage to the pre-deposited perovskites. Therefore, the PSCs can be divided into n-i-p (regular) and p-i-n (inverted) architecture, depending on the positions of ETL or HTL relative to the transparent conductive electrode where the light strikes first, as shown in Figure 1.4b,c.[36] So far, both types of PSCs have achieved the efficiency of over 25%.[41-43] It can be attributed to the development of perovskites, electron transport materials, and hole transport materials. In recent years, nickel oxide and self-assembled monolayers exhibit excellent performance in inverted PSCs.[44-46] Spiro-OMeTAD is generally used as hole transport material in n-i-p PSCs, while electron transport layers include TiO_2, SnO_2, ZnO, and Nb_2O_5.[47] Among them, SnO_2 is widely adopted in high-performance PSCs (Figure 5), due to its excellent optical and electrical properties, feasible preparation process, and excellent stability under illumination. Initially, the application of SnO_2 ETL in PSCs was introduced by Fang and co-workers via spin-coating precursor solutions of $SnCl_2 \cdot 2H_2O$.[48] Subsequently, Hagfeldt and co-workers introduced atomic layer deposition and chemical bath deposition to prepare SnO_2 layers in planar PSCs.[49] In 2017, You and co-workers introduced a commercial dispersion of SnO_2 nanoparticles and achieved a certified efficiency of 19.9%.[50] Due to the simple spin-coating process, it is widely used in PSCs. So far, PSCs based on SnO_2 have obtained the efficiency of 26.1% (certified 25.6%),[51] and flexible counterparts reached 24.61% (certified 23.51%).[52] One of important contribution of this thesis is to adjust the properties of SnO_2/perovskite interface and enhance its stability. Accordingly, the cell performance and stability are dramatically improved.

1.2.4 Application of perovskites in tandem solar cells

Due to the tuneable bandgap via halide and cation replacement, perovskites exhibit excellent performance in tandem solar cells, including perovskite/silicon, perovskite/organic, perovskite/perovskite, and perovskite/CIGS tandem solar cells. Among them, the perovskite/silicon tandem achieves much more attention, as silicon solar cells have been commercialized and certified efficiency reach 27.1%.[6,7] Also, absorbed incident light covers a wide spectral range from 300 to 1100 nm, which depends on the bandgap of crystalline silicon. According to the connection between perovskite top cell and silicon bottom cell, mechanically-stacked (4-terminal) and monolithic (2-terminal) perovskite/silicon tandem solar cells can be achieved

respectively. In 2014, Löper and co-workers introduced 4-termianl perovskite/silicon tandem solar cells by sputtering indium tin oxide (ITO) on top of the spiro-OMeTAD with the protection of a 30 nm MoO_x layer.[53] During the same period, Bailie and co-workers used transferred layers of silver nanowires as semi-transport electrodes for 4-termianl perovskite/silicon tandem solar cells and reached an efficiency of 17.0%.[54] In 2015, Werner and co-workers directly sputtered an amorphous indium zinc oxide (IZO) layer on spiro-OMeTAD as broadband transparent rear electrode, which reduced the sputter damage and series resistance caused by MoO_3 interlayers.[55] Consequently, the four-terminal tandem efficiency was increased to 18.2%.[55] It is noted that the commonly used spiro-OMeTAD in n-i-p single-junction PSCs leads to seriously parasitic absorption in perovskite/silicon tandem solar cells, limiting the current density.[56]

In 2015, Mailoa and co-workers realized monolithic 2-terminal perovskite/silicon tandem solar cells for the first time by using a n^{++}/p^{++} tunnel junction,[57] which contains heavily doped n^{++} hydrogenated amorphous silicon (a-Si:H), a 2–3 nm-thick intrinsic a-Si layer, and the p^{++} emitter. The dopant concentration at the n^{++}/p^{++} Si interface after the dopant activation anneal is 10^{19}–10^{20} cm^{-3}, so it can work as a high-quality interband tunnel junction. Nowadays, a transparent conducting oxide (TCO) recombination layer is generally used between Si and the perovskite sub-cells.[58,59] Photons with higher energy are absorbed by the perovskite sub-cell without significant losses from thermalization. Infrared photons pass through the perovskite and TCO, and lead to photon absorption and generation of excitons in the silicon sub-cell. Thus, the parasitic absorption and resistive loss caused by the TCO recombination layer should be regulated carefully. In recent years, mechanically-stacked and monolithic perovskite/silicon tandem solar cells developed rapidly, and both of them have achieved the efficiency of over 30% with the optimization of perovskites,[60,61] recombination layers,[62] and charge transport layers.[63,64] Dual-junction tandems stacking two sub-cells have a detailed balance limit of over 40%,[65] exceeding the Shockley–Queisser limit of single-junction PSCs (31-33%) and showing more excellent prospect for commercialisation.[66,67]

1.3 The stimuli inducing degradation of perovskite solar cells

Although tremendous progress has been made in improving the efficiency of PSCs, the commercialisation prospect of the technology still faces a major challenge - stability.

Perovskites and PSCs can be affected by external stimuli, including humidity, light, heat, high-energy radiation, strain, and reverse bias, leading to degradation of device performance. The mechanisms of device performance degradation caused by these stimuli have been reported, respectively.

1.3.1 Humidity

Interfacial hydration and bulk hydration caused by humidity can lead to the collapse of perovskite crystal structure, thus significantly affecting the stability of perovskite and PSCs. However, it has been reported that the ambient environments with controlled relative humidity during the annealing and storage processes can improve the surface morphology of perovskite films and increase the perovskite grain size.[68] Considering that perovskite modules will be protected by encapsulation in actual field, the instability of perovskites caused by humidity can be avoided by encapsulation. However, the large-scale fabrication of perovskite modules requires bypassing glove boxes, while the moisture in the air significantly affects the morphology of perovskite films.[69,70] It is because the moisture can cause rapid and directional precipitation of lead iodide during the fabrication of perovskites.[71,72] This may be an obstacle to the commercialization of PSCs, but lead acetate and lead thiocyanate can be used as the lead source in perovskite precursor solution to avoid this problem.[73,74] Due to the limited photovoltaic performance of PSCs based on non-halide lead sources,[73-75] related work needs further study.

1.3.2 Illumination

Perovskite films would degrade under full spectrum sunlight as well. Tang and co-workers found that $CH_3NH_3PbI_3$ converted to lead iodide and metallic lead (Pb^0) when exposed to vacuum and light illumination.[76] Fang and co-workers further confirmed that Pb^0 impurities were decomposition byproducts of residual PbI_2 in perovskites under light, while perovskites without excess lead halides hardly induce Pb^0 impurities and have a much better stability under light.[77] Metallic lead would act as carrier recombination centres in perovskites, which reduces device performance and accelerates the degradation of PSCs.[77] Adachi and co-workers have confirmed that the operational stability of PSCs under light can be improved via precise control of the unreacted PbI_2 crystals in perovskite films.[78] In addition, illumination can cause halide

phase segregation in perovskites, especially in wide bandgap perovskites. In 2015, Hoke and co-workers reported reversible, light-induced transformations in $(CH_3NH_3)Pb(Br_xI_{1-x})_3$, namely halide segregation into iodide-rich minority and bromide-enriched majority domains.[23] Slotcavage and co-workers found that the phase segregation is induced by halide migration and lattice strain.[25] The issue may be solved by tailoring the perovskite composition and lattice structure, and reducing defect concentrations.[79-81]

1.3.3 Heat

The thermal effect results from the exposure of perovskite modules to sunlight. When a concentrator is used, the issue becomes more serious. Perovskite will decompose into PbI_2 at elevated temperature. Even though lead iodide has been confirmed to be able to passivate defects in perovskite films,[82,83] excessive lead iodide is not beneficial to carrier transport due to the high bandgap of lead iodide and the operational stability of PSCs will be deteriorated.[77,82-84] In addition, MA^+ cations have higher volatile nature as compared to other cations such as FA^+ and Cs^+, creating more ion vacancies in perovskites.[85,86] Apart from that, the electron/hole transport layers can be affected by heat, especially spiro-OMeTAD that is widely adopted in high-performance n-i-p PSCs. Specifically, heat can lead to the crystallization and a severe morphological deformation of spiro-OMeTAD.[87,88] Therefore, charge transport materials with better thermal stability are of great significance for improving the operational stability of PSCs.

1.3.4 High-energy radiation

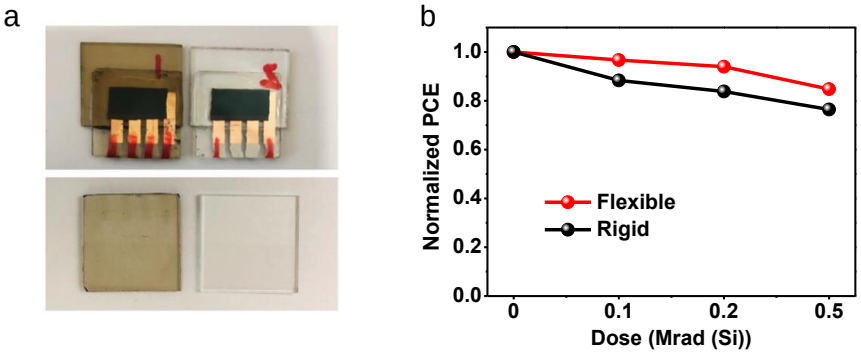

Figure 1.6. *(a) photographs of PSCs (top) and ITO substrates (bottom) before (right) and after (left) gamma-ray irradiation;*[91] *(b) normalized PCEs of PSCs based on rigid and flexible substrates as a function of irradiation dose.*[93]

PSCs have high power-to-weight ratio and they are vulnerable to moisture, so space without moisture and oxygen is suitable for the application of PSCs. It is necessary to explore the influence of the high-energy radiation including gamma rays, proton radiation, and electron radiation on the PSCs. For example, Miyazawa and co-workers found that PSCs with MA-based perovskites demonstrated sufficiently high durability against 1-MeV electron irradiation with high fluence up to 1×10^{16} cm^{-2}.[89] Lang and co-workers reported that $CH_3NH_3PbI_3$ perovskite could withstand proton doses up to 10^{12} p cm^{-2}, exceeding the damage threshold of crystalline silicon by almost three orders of magnitude.[90] However, the colour centres in the glass substrate will be caused by proton radiation, decreasing the transmittance of glass substrate.[90] Also, the influence of gamma ray on PSCs has been reported. Yang and co-workers showed that the glass substrate used in PSCs was easily affected by gamma rays (Figure 1.6a), leading to obvious loss of substrate transmittance and a decrease in the short-circuit current density (J_{sc}), but the perovskite films were relatively stable under gamma-ray irradiation.[91] Yang and co-workers reported similar results, but they found that perovskite films could decompose to lead iodide under gamma rays, especially at grain boundaries.[92] Huang and co-workers found that flexible PSCs with PEN/ITO [PEN: poly(ethylene naphthalate)] presented better gamma-ray radiation tolerance, as compared to rigid counterparts (Figure 1.6b).[93] It is attributed to that PEN/ITO substrate was less affected by radiation than rigid counterparts. The above results indicate that the stability of perovskite under high-energy radiation needs to be further investigated.

1.3.5 Strain

The strain in perovskite films mainly results from two aspects: (1) the distortion within the perovskite lattice, which leads to the strain inside the perovskite crystallites, but it can be eliminated by carefully adjusting the cations and anions of perovskites;[94] (2) due to the mismatched thermal expansion coefficient of perovskite films and substrates, the shrinkage between perovskite and substrate is different during cooling process, which results in in-plane tensile strain in perovskite films. Huang and co-workers showed that the in-plane tensile strain accelerated the degradation of perovskite films under illumination.[95] Chen and co-workers identified the gradient distribution of in-plane strain component perpendicular to the substrate, by depth-dependent grazing incident X-ray diffraction (GIXRD) measurements.[96] The tensile strain led to energy

bands bending of the perovskite film and hindered the hole carrier transport at the interface between perovskite and HTL. The residual stress of perovskite films can be released by A site cation alloying,[97] and interface modification.[98] Additionally, compressive strain in perovskites can be used to stabilize α-$FAPbI_3$ phase and change the crystal structure and bandgap of perovskite.[99]

1.3.6 Reverse bias

In actual field, some sub-cells may be shaded by external factors such as chimney, birds, and snow (Figure 1.7a). Given series connection between sub-cells in perovskite modules, the shaded part needs to withstand the reverse bias generated by other sub-cells exposed to light, as shown in Figure 1.7b. The bypass diode can be used to avoid the degradation of solar cells induced by reverse bias, but it will increase the fabrication cost and weight of solar panels. Therefore, it is necessary to investigate the behaviour and stability of PSCs under reverse bias.

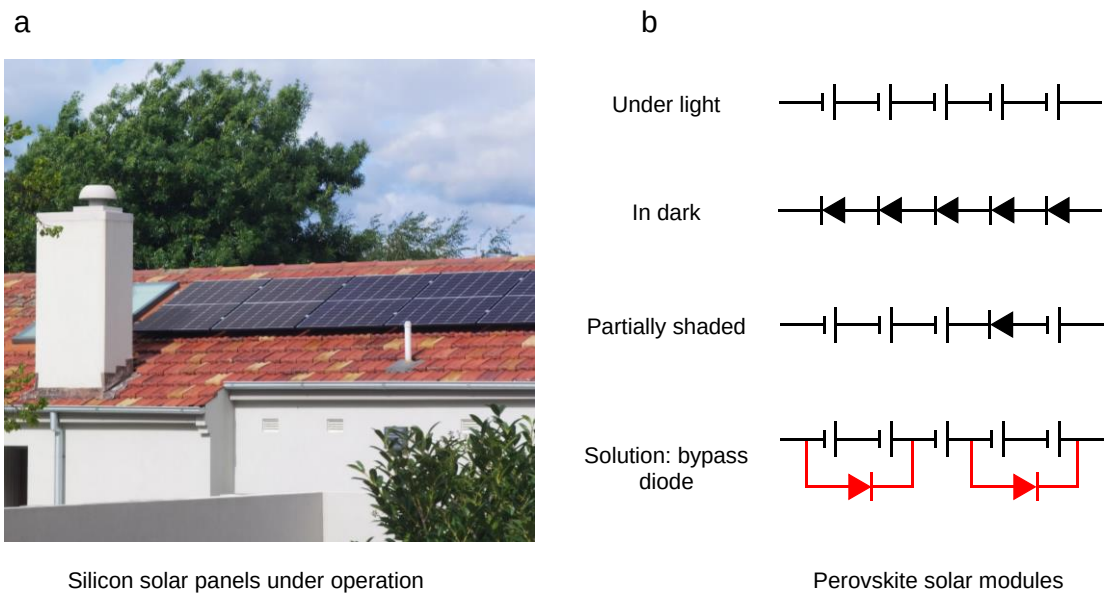

Figure 1.7. *(a) Silicon solar panels under sunlight; (b) schematic of perovskite solar modules under different conditions.*

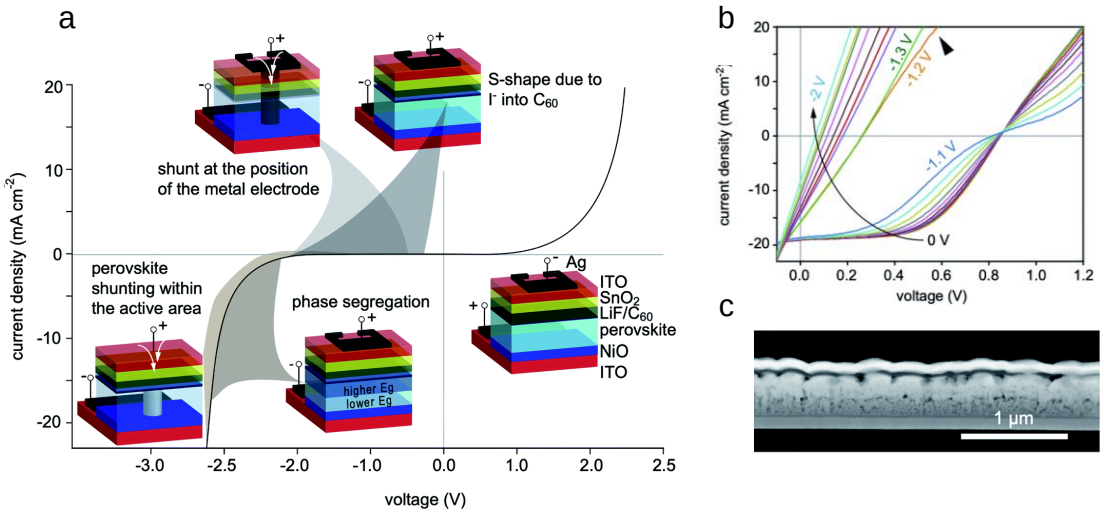

Figure 1.8. *(a) Schemic of degradation of p–i–n single-junction perovskite solar cells during reverse biasing as a function of the voltage range; (b) J-V curves taken immediately after reverse biasing the cell at different reverse voltages; (c) scanning transmission electron microscopy (STEM) high-angle annular dark-field image of the PSC degraded at -5 V, showing a double layer structure in the perovskite film.*[100]

As shown in Figure 1.8, Razera and co-workers found that the reverse bias could cause several issues for p-i-n PSCs, including the formation of highly conductive shunts, an S-shape in the current density-voltage (*J-V*) curve, and degradation of perovskite into iodide- and bromide-rich sub-layers.[100] The results depend on the reverse voltage applied, the duration of the treatment, and the device structure. McGehee and co-workers found that reverse bias could cause a partially recoverable loss in PCE and open-circuit voltage (V_{oc}).[101] Additionally, they reported that the tunnelling holes into the perovskite due to sharp band bending can trigger the oxidation of halides to form neutral halogens.[102] The resulting halogens could work as bulk recombination centres, which account for the losses in the cell performance.[102] The interaction between the iodide interstitials and injected holes at the interface between perovskite and electron transport layer, which triggers the degradation of PSCs under reverse bias, has been confirmed by drive-level capacitance profiling (DLCP) technique.[103] Considering that the *J-V* hysteresis in PSCs is generally attributed to the carrier accumulation and defects at the interfaces,[104] the ion migration induced by external stimuli can also affect the hysteresis. For instance, Jen and co-workers found that reverse bias could result in abnormal hysteresis, which is similar to tunnel diode current-voltage characteristics.[105]

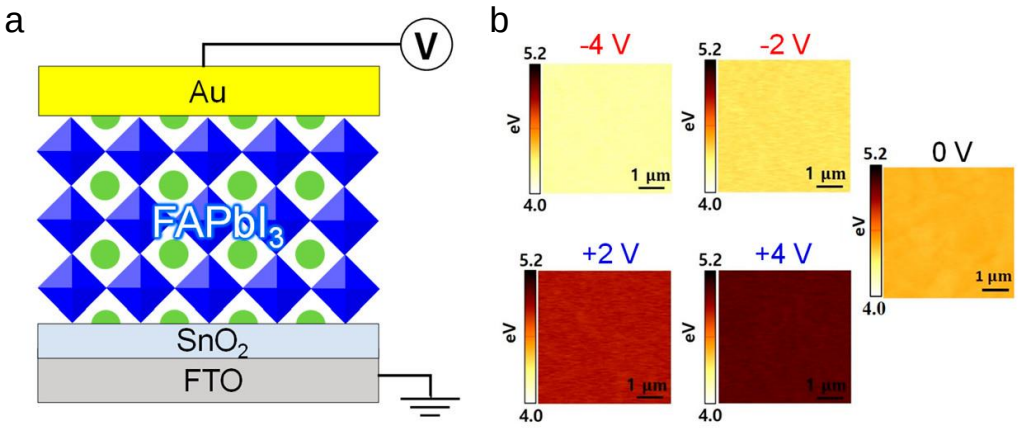

Figure 1.9. *(a) Schematic device structure, where the voltage was applied on the Au electrode. (b) Surface work function map of the perovskites with applied voltages of −4, −2, 0, +2, and +4 V obtained from kelvin probe force microscope (KPFM) measurements. It is noted that the Au electrode was removed by Scotch tape before KPFM measurements.*[106]

Nonetheless, ion movement and charge transfer in perovskite or devices under electric field are not always harmful, especially when the process is controlled within a recoverable range. For example, continuous tuning of the work function and varying the polarity of $FAPbI_3$ perovskite films could be realized by the negative and positive applied voltages, as shown in Figure 1.9.[106] In addition, n-doped $CsPbBr_3$ nanocrystal thin films could be achieved via electrochemical doping, leading to an increased photoluminescence intensity.[107] Meng and co-workers found the improved device performance during maximum power point tracking (MPPT) or under forward bias, which was attributed to the filled traps by moving ions during the operation.[108] Recently, Choi and co-workers applied a pulsatile reverse pulse (30 s) in the middle of MPPT to eliminate accumulated charges and ions, which can revive the degraded PSC and improve the stability of the working device.[109] Generally, the dark recovery phenomenon after continuous illumination and MPPT should be closely related to the ion migration in the perovskite layer.[110-112] Huang and co-workers found that the efficiency of PSCs can increase and partially recover during gamma-ray radiation, which would be closely related to the self-healing induced by ion-migration behaviour.[91] These results above provide a possibility that ion migration can be utilized via external stimuli to adjust the properties of perovskites and performance of PSCs.

These results above show that the reverse bias can cause a series of phenomena in PSCs, which may depend on the device structure, perovskite composition and so on, so it is necessary to further investigate the behaviour of PSCs and improve their stability under reverse bias. In Chapter 2, sparkling hot spots in PSCs under reverse bias will be

presented, and its mechanism will be discussed. Reversible enhancement in cell performance induced by reverse bias will be shown in Chapter 3, which is attributed to iodine ion migration and accumulation of iodine ions at the SnO_2/perovskite interface.

CHAPTER 2

2 Sparkling hot spots in perovskite solar cells under reverse bias

In this chapter, we analyse the behaviour of perovskite solar cells under reverse bias, focusing on the appearance and disappearance of localized sparkling hot spots within the active area. Employing an in-situ temperature monitoring technique, we observe these transient hot spots alongside changes in temperature and current. Our investigation unveils a novel phenomenon and sheds light on the underlying mechanisms, namely ion accumulation-induced band bending and tunnelling current. Furthermore, we investigate the influence of bulges in perovskite films on device performance under illumination. These results enhance the understanding of reverse-bias stability in PSCs.

2.1 Introduction

PSCs have attracted much attention and shown tremendous potential over the decade due to their rapidly increasing PCE and many other strengths, such as solution processability and relatively low process costs. Given the fact that the PCE for single-junction and perovskite/silicon tandem solar cells has reached 26.1% and 33.9%, respectively,[6] the critical limit for PSCs commercialization is no longer the photovoltaic output but their long-term stability.

Currently, the research on the stability of PSCs mainly focuses on preventing the degradation caused by external stimuli such as humidity, oxygen and ultraviolet light.[113-115] Numerous strategies, including but not limited to composition engineering, additive engineering and encapsulation, have been proposed to improve PSC stability.[116,117] Nonetheless, studies on PSCs under reverse bias are still limited. In the field, individual cells in photovoltaic modules are frequently subject to reverse bias.

This is mainly due to external factors (birds, cleaning and maintenance personnel, tree trunks, etc.) that will shade part of the module, and these shaded cells will be subject to the reverse bias induced by other cells exposed to sunlight. Such reverse bias has the potential to damage the cell and deteriorate the performance of whole photovoltaic module.[118] The impact of reverse bias on PSCs has been presented in Chapter 1, but the in-situ characterization on PSCs under reverse bias is still absent.

Herein, the infrared micro-thermography, a non-destructive and in-situ temperature measurement technique, was adopted to investigate the reverse-bias behaviour of PSCs. It was found that sparkling hot spots occurred in PSCs under reverse bias. Meanwhile, the current increased abruptly along with the temperature ascending at the hot spots. Through layer-by-layer investigation within the cell, an abnormal bulge in the perovskite film was observed at the hot spot. A potential mechanism for the generation and disappearance of the sparkling hot spots was analysed thoroughly. Also, the relationship between the hot spots and the photovoltaic performance of the PSCs has been revealed. These results show a reference for improving the reverse-bias stability of PSCs.

2.2 Solar cell fabrication and characterization

The PSCs were fabricated according to our previous report.[119] It is necessary to point out that a two-step spin-coating process (also called sequential deposition) was used here for perovskite films. Specifically, a PbI_2 layer (with caesium iodide as an additive) was first prepared by spin-coating and annealing, followed by spin-coating of halide organic salts ($HC(NH_2)_2I$, CH_3NH_3Cl, and CH_3NH_3Br). The perovskite was formed during the subsequent annealing process. Digital Source Meter (Keithley, Model 2420) and infrared micro-thermography (FLIR A615) were utilized to monitor the current and temperature of reverse-biased devices, respectively. The resolution of the infrared micro-thermography is 640 × 480, with a recording frame rate of 12.5 fps, and the thermal sensitivity is less than 50 mK. The spatial resolution of the microscope lens is 25 pm. The measurement was carried out in ambient air with controlled relative humidity (~40%) and temperature (22-30 ºC). Photovoltaic performance of PSCs was obtained by a digital Source Meter (Keithley, Model 2420) under a Xenon-lamp-based solar simulator (Newport 91160s, AM 1.5G) with a light intensity of 100 mW cm^{-2}, which was calibrated by a standard silicon solar cell. The scanning direction was from +1.2 V to 0 V with 60 points and a 50 ms scanning delay. Dektak XT stylus profiler and

optical microscope (Caikon, CK-300) were utilized to characterize the surface morphology of spiro-OMeTAD, perovskite and SnO_2 layers. The spiro-OMeTAD, perovskite and SnO_2 layers were exposed step by step via removing the anti-reflective tape and cleaning the samples with chlorobenzene and *N,N*-dimethylformamide. Anti-reflective tape is a commonly used transparent frosted tape (white), which was from Guangning County Xidangdang Trading Co., Ltd.

2.3 Results and discussion

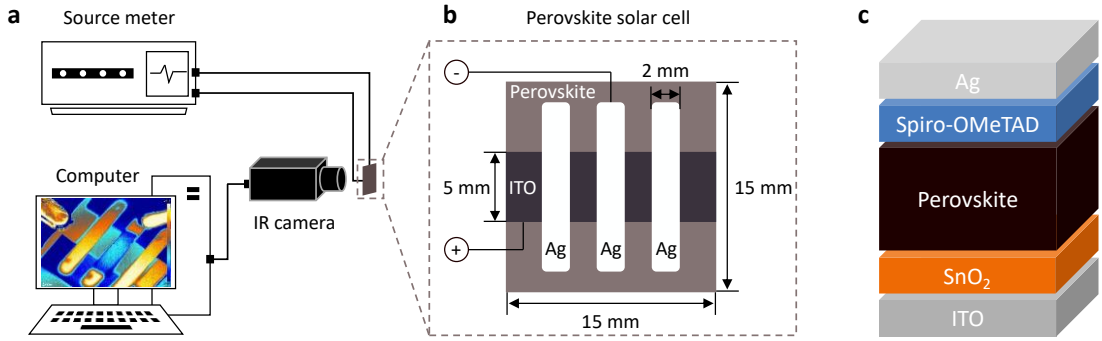

Figure 2.1. *(a) Experiment schematic; (b) top-view schematic of the PSC; (c) device structure adopted in this study.*

The schematic diagram of the test system is shown in Figure 2.1a. A digital Source Meter provided reverse bias for PSCs and collected the data of current. The infrared micro-thermography was utilized to monitor the temperature of reverse-biased devices under ambient air without external light sources. Figure 2.1b shows the top-view schematic of the sample, and the active area is the overlap of silver electrode and ITO. Planar heterojunction PSCs with a structure of ITO/SnO_2/ $FA_{0.945}MA_{0.025}Cs_{0.03}Pb(I_{0.975}Br_{0.025})_3$/spiro-OMeTAD/Ag were adopted, as shown in Figure 2.1c, which were fabricated according to our previous report.[119] This type of PSCs shows much stronger competitive edges in photovoltaic performance and stability.[120,121] In addition, an anti-reflective tape with good thermal conductivity was pasted on the silver surface to reduce the reflection of the rear electrode and improve the accuracy of temperature measurement.

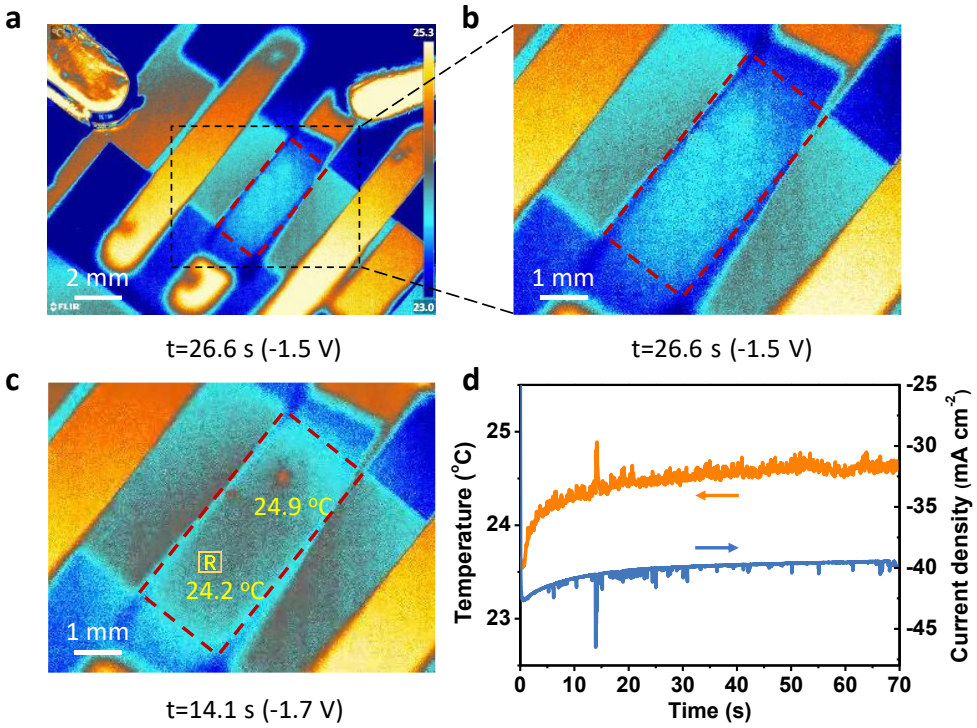

Figure 2.2. *(a) Thermal image of the PSC reverse biased at -1.5 V for 26.6 s; (b) enlarged image of the area marked by the black dotted line; (c) enlarged thermal image of the PSC reverse biased at -1.7 V for 14.1 s; (d) temperature change on hot spot location and current change in the cell under reverse bias.*

Figure 2.2a shows the thermal image of a typical PSC under reverse bias of -1.5 V. Obviously, the temperature distribution is uniform within the active area marked with red dash box, even in the enlarged image (Figure 2.2b). However, a hot spot was observed and then quickly disappeared when the cell was stressed up to -1.7 V. Figure 2.2c shows the snapshot of the temperature distribution after -1.7 V reverse bias loading for 14.1 s, in which the sparkling hot spot appeared.

Apart from that, the temperature of the hot spot and the current of the cell were recorded during the test, as shown in Figure 2.2d. The temperature of the hot spot increased slightly at the beginning, which should be attributed to the thermal effect caused by current, and showed a rapid growth to almost 24.9 °C at 14.1 s, after which it stabilized gradually despite the fluctuation. When it comes to the current, there was a sharp increase in the first second, followed by an exponential decrease in the following 10 s, which was consistent with the result in literature.[101] Also, the current experienced a drastic increase at 14.1 s before remaining stable. The results suggest that a local breakdown occurred in the hot spot area at 14.1 s.

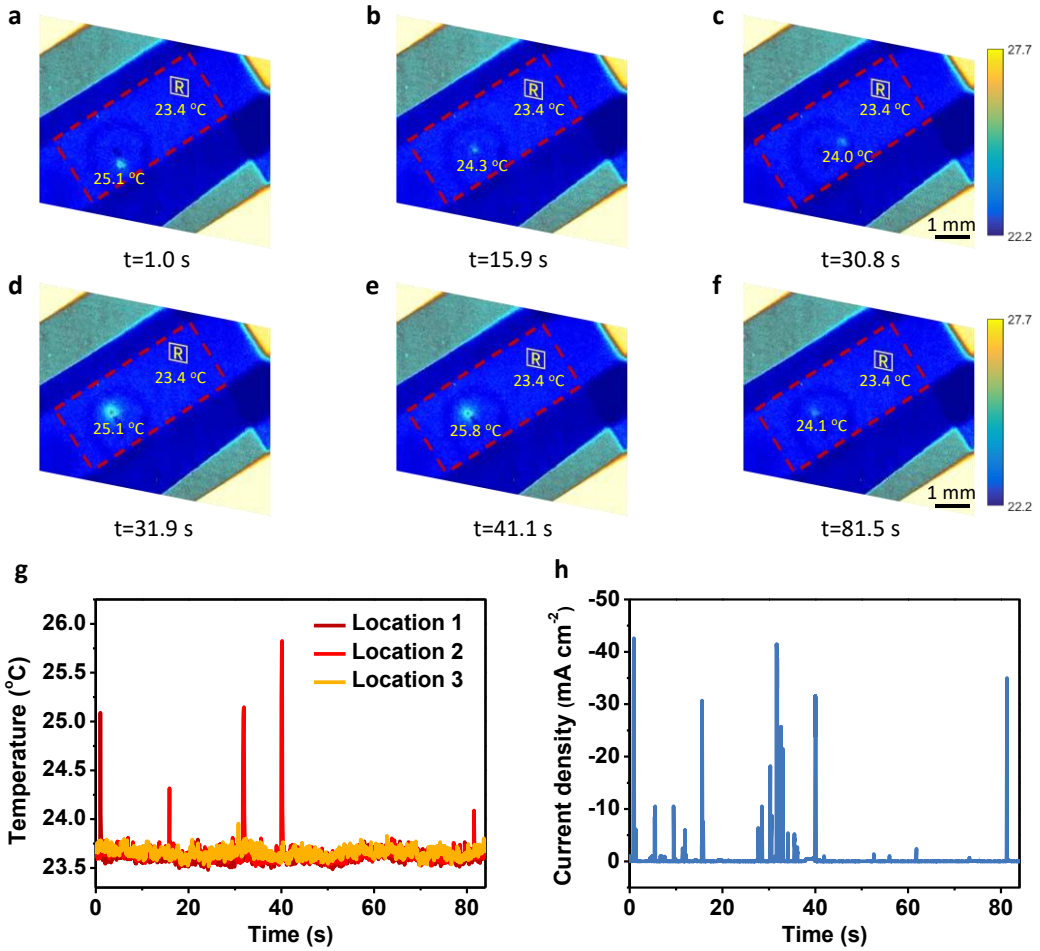

Figure 2.3. *Thermal images of a typical PSC under reverse bias for (a) 1.0 s, (b) 15.9 s, (c) 30.8 s, (d) 31.9 s, (e) 41.1 s, (f) 81.5 s. Note that the hot spots at 1.0 s, 15.9 s and 30.8 s are denoted as Location 1, 2 and 3, respectively. (g) Temperature change of different hot spot as a function of time; (h) current change in the reverse biased cell as a function of time.*

In effect, normal hot spots have been discovered previously, which are ascribed to the formation of shunts due to silver melting or metal migration induced by reverse bias.[100,101] However, the proposed mechanism is hard to explain the phenomenon here that the current and temperature return to normal after the hot spot. More importantly, multiple hot spots and frequently flashing hot spots on the reverse-biased PSC were also observed (Figure 2.3).

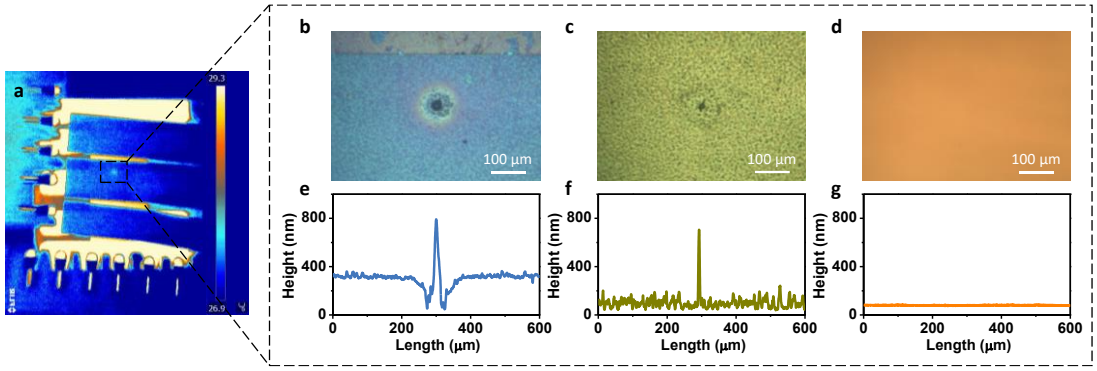

Figure 2.4. *(a) Thermal image of the PSC with a sparkling hot spot; optical microscope images of the (b) spiro-OMeTAD layer, (c) perovskite layer, (d) SnO_2 layer at the hot spot; step-profiler diagram of the (e) spiro-OMeTAD layer, (f) perovskite layer, (g) SnO_2 layer at the hot spot.*

To investigate the origin of sparkling hot spots, the PSC was characterized layer by layer (see more experimental details in 2.2 Solar cell fabrication and characterization). As shown in Figure 2.4a, a typical sparkling hot spot was observed. The surface morphology of spiro-OMeTAD, perovskite and SnO_2 layers at the hot spot was measured and shown in Figure 2.4b, Figure 2.4c and Figure 2.4d, respectively. It indicates that there was an obvious anomaly on spiro-OMeTAD and perovskite films, but the SnO_2 layer was smooth. Also, the profiles of these three layers at the hot spot were measured by a step profiler to show the height of the film surface. As shown in Figure 2.4e-g, there was a clear bulge on the HTL and the perovskite layer, corresponding to the anomaly mentioned above. On the contrary, the surface of the SnO_2 film is extremely flat. These results suggest that the sparkling hot spot should be ascribed to the abnormal bulge in the perovskite film.

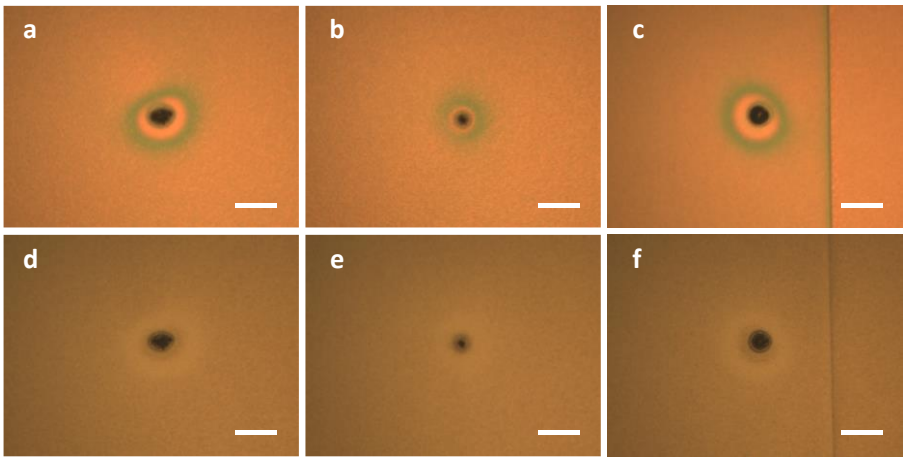

Figure 2.5. *Optical microscope images of PbI_2 layers at the (a) first, (b) second, (c) third bulge; optical microscope images of perovskite layers at the (d) first, (e) second, (f) third bulge. It is noted that (d), (e), and (f) originate from corresponding locations in (a), (b), and (c), respectively. Scale bar: 100 μm.*

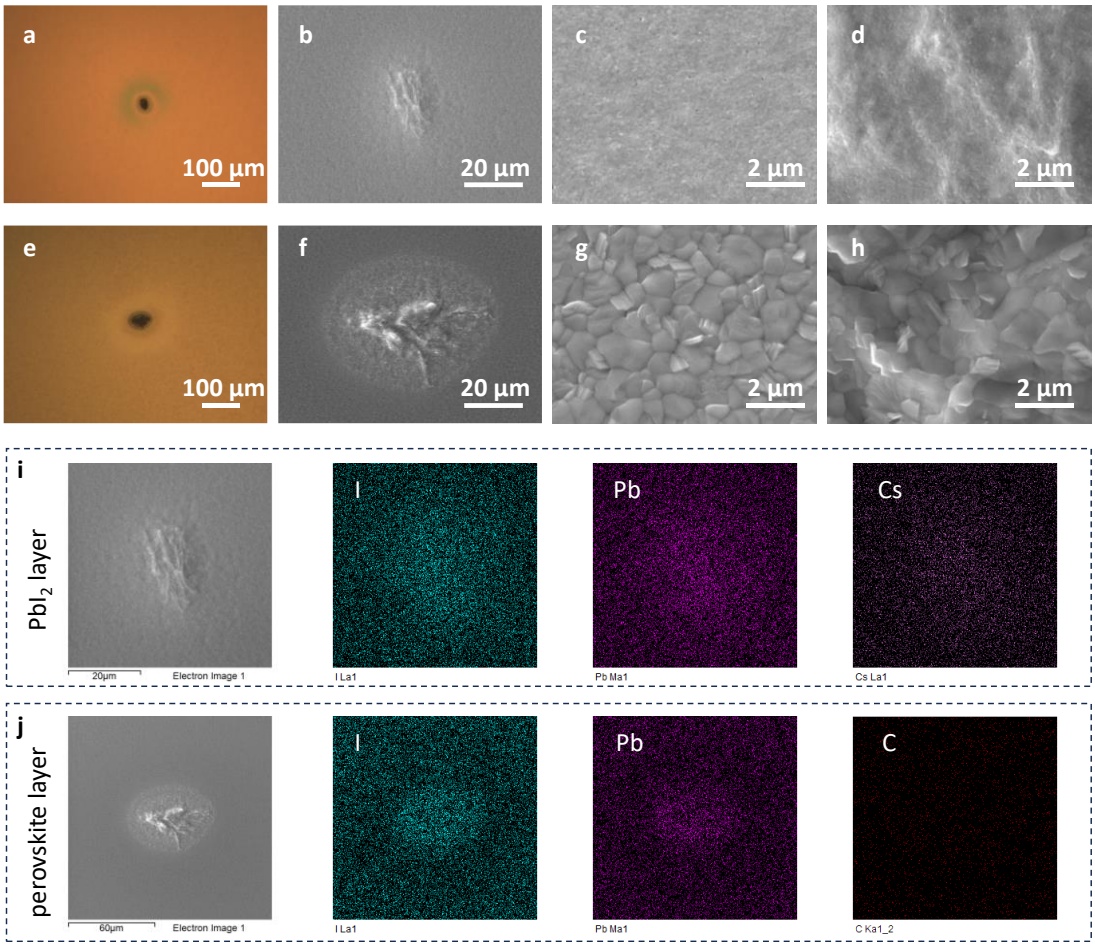

Figure 2.6. *(a) Optical microscope image and (b) SEM image of the PbI_2 layer at the bulge; SEM images of the PbI_2 layer in (c) the part outside the bulge and (d) the centre of the bulge. (e) Optical microscope image and (f) SEM image of the perovskite layer at the bulge; SEM images of the perovskite layer in (g) the part outside the bulge and (h) the centre of the bulge. SEM-EDX analysis of the (i) PbI_2 and (j) perovskite layer at the bulges.*

To investigate what the bulge in the perovskite film is and where it comes from, more characterization was carried out. First, optical microscope images of PbI_2 layers were measured. It was found that abnormal bulges were observed in PbI_2 layers as well (Figure 2.5). Importantly, these strange bulges were still observed in accordingly fabricated perovskite layers. It is noted that two-step spin-coating was utilized to fabricate perovskite films here. The bulges in lead iodide and perovskite films were characterized by scanning electron microscopy (SEM). It is found that the centre of the bulges and the part outside the bulges show highly similar morphologies (Figure 2.6a-h). It is necessary to point out that the SEM images were obtained after a reverse bias experiment of the cell, but the perovskite didn't decompose obviously at the bulge and at the outside of the bulge (Figure 2.6g,h). These results suggest that the perovskite will not decompose into PbI_2 under reverse bias, which should be attributed to the minor

bias voltage used in the experiments. EDX analysis further confirms that the bulge in the PbI_2 and perovskite layers should be PbI_2 cluster and perovskite, respectively (Figure 2.6i,j). These results suggest that the bulge in the perovskite film should result from the lead iodide cluster in the PbI_2 film, rather than impurity particles from the external atmosphere. It is speculated that the lead iodide clusters are formed before or during first-step spin-coating, but the problem may be solved by additive or solvent engineering.[122,123]

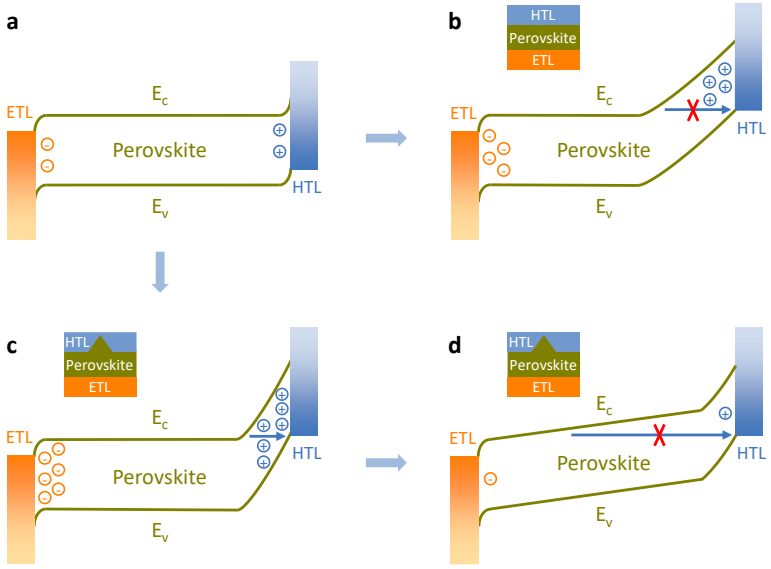

Figure 2.7. *Band diagrams of (a) the PSC in dark equilibrium at 0 V, (b) the bulge-free PSC under reverse bias, (c) the PSC with abnormal bulges under reverse bias, (d) the reverse biased PSC with bulges after the hot spot.*

It is still important to explore the mechanism how the abnormal bulge in the perovskite layer causes the emergence and disappearance of hot spots. McGehee and co-workers proposed that the reverse bias current more likely resulted from tunnelling rather than avalanche multiplication, according to the drift-diffusion model (DDM).[101] The phenomenon here may be explained by DDM combined with the hypothesis that mobile ions accumulate at the perovskite/HTL interface.[124] Figure 2.7a shows the band diagram of the perovskite solar cell in dark equilibrium at 0 V. After applying reverse bias, the anions and cations of perovskite drift to ETL and HTL respectively, and gradually accumulate at the interfaces. During this process, the temperature of full active area increased slightly, and was higher than other areas (Figure 2.2b,d). The ion accumulation leads to band bending, but it is not sufficient to cause tunnelling current (Figure 2.7b) due to homogeneous accumulation over the full active area. If there are some bulges in the perovskite film, more mobile ions will gather together rather than

uniformly distributed at the interface, leading to severer band bending in the local area (Figure 2.7c). Since perovskite at the bulge protrudes from the entire perovskite plane, more mobile ions at the bulge or at the outside of the bulge would preferentially accumulate at the bulge. When the band bending at the bulge is significant enough, electrons tunnel from HTL to the conduction band of perovskite, and the accumulated cations diffuse from the absorber to HTL.[101] Subsequently, the local temperature increases and the hot spot appears, due to the extra current. Ion diffusion is also accelerated by the slightly elevated temperature. However, the band bending will become insufficient to cause tunnelling after ion diffusion (Figure 2.7d). Accordingly, the reverse bias current descends and the hot spot disappears.

It is necessary to point out that the bulge on the perovskite film leads to thinner HTL in local area (Figure 2.4b,e). It will promote the generation of tunnelling current as electron tunnelling is more likely to occur in areas with thinner HTL. This interprets why sparkling hot spots are observed at the bulges. Apart from that, it is noteworthy to mention that the mobile ions will accumulate again at the interface under reverse bias, especially at the bulge in the perovskite film, leading to the appearance of hot spots. Given that the heavy reverse current may degrade the perovskite absorber,[100] the upcoming hot spot will appear randomly, and the location of the sparkling hot spot may also change if there are multiple bulges in the perovskite film (Figure 2.3). All in all, the dual effects of ion accumulation and diffusion across the interface trigger the hot spots to appear and quickly disappear.

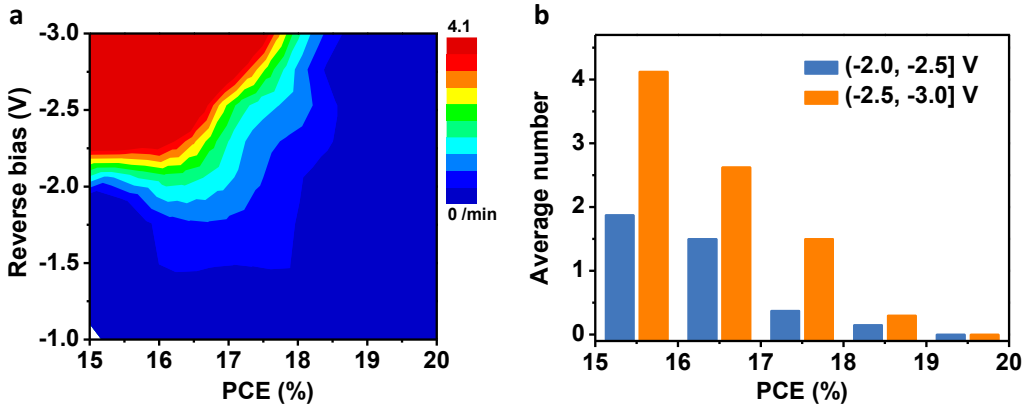

Figure 2.8. *(a) Average frequency of hot spots in PSCs with different PCE and reverse bias; (b) average frequency of the hot spot as a function of the cell efficiency and reverse bias.*

The relationship between the photovoltaic performance of PSCs and the hot spots was investigated. Some sparkling hot spots appeared repeatedly in the same place, so

the average frequency of the hot spots in PSCs based on different PCE and reverse bias was statistically analysed. Figure 2.8a shows the result of twenty PSCs from one batch and each cell was measured under different reverse voltage ranging from -1.0 V to -3.0 V. It suggests that hot spots barely appear under low reverse bias or in efficient PSCs with high PCEs (> 19%). In general, hot spots were frequently observed in PSCs with low PCEs and under heavy reverse bias (Figure 2.8b). Since the hot spot is closely related to the abnormal bulge in perovskite, Figure 2.8a implies that the perovskite films in highly efficient PSCs are bulge-free and the limited performance of PSCs with 16-18% efficiency may result from the bulges. Although charge carriers can be effectively extracted under illumination and will not accumulate at the interface, these bulges still affect the morphology of HTL and eventually deteriorate the device performance. Additionally, hot spots rarely appeared in PSCs with extremely low efficiency (< 16%) under low voltages less (in magnitude) than -2.0 V. Only when reverse bias (absolute value) increased to over 2.0 V would the hot spot emerge in these PSCs. It indicates that extremely low performance of PSCs should not result from the abnormal bulges in perovskite, but other factors such as pinholes in the perovskite absorber or charge transport layer, which lead to severe shunting current.

In fact, the test system proposed here cannot only be utilized to study the reverse-bias behaviour of PSCs, but also achieve defects recognition and localization. Combined with healing techniques in local areas, it can realize the rapid detection and repair of large-area modules.

2.4 Conclusion

In summary, in-situ temperature technique was carried out to monitor the PSCs under reverse bias. Localized sparkling hot spots were observed in the active area, along with the increase of the temperature and current. Also, both of them became normal immediately as the hot spots disappeared. The phenomenon here is firstly reported, and it is well explained by experimental characterization, band bending and tunnelling current caused by ion accumulation. With the presence of bulges in perovskite films, the band bending at the interface induced by ion accumulation is significant enough to allow tunnelling current. Nonetheless, the diffusion of accumulated ions is accelerated as well, which weakens band bending and ends tunnelling, leading to the disappearance of hot spots. In addition, it was found that the photovoltaic performance of PSCs under illumination might be affected by the bulges in perovskite films. These results are of

great significance to improve the reverse-bias stability and performance of the cells.

CHAPTER 3

3 Manipulating the migration of iodine ions via reverse-biasing for boosting photovoltaic performance of perovskite solar cells

Due to the ion migration induced by electric field, the stability of perovskites can be affected by external bias voltage. Therefore, reverse bias often leads to deterioration of device performance.[100-102] Given the presence of undercoordinated Pb^{2+} ions at the surface of perovskite, deep energy level traps can be introduced and work as charge carrier recombination centres, which limits the device performance.[104] Previous reports show that the surface properties of perovskite can be adjusted by external bias voltage.[106,109] Herein, the improvement in cell performance was achieved by precise control of reverse bias and its loading time. Iodine ions including iodine interstitials would migrate and ultimately accumulate at the SnO_2/perovskite interface under reverse bias, which fill iodine vacancies at the interface and interact with SnO_2. More details are presented below.

3.1 Experimental section

3.1.1 Materials

All materials were used directly without any purification: tin oxide precursor (SnO_2, 15% in H_2O colloidal dispersion, Alfa Aesar), $HC(NH_2)_2I$ (FAI, 99.5%, Xi'an Polymer Light Technology Corp.), [6,6]-phenyl-C61-butyric acid methyl ester ($PC_{61}BM$, Xi'an Polymer Light Technology Corp.), lead iodide (PbI_2, 99.999%, Sigma-Aldrich), CH_3NH_3Cl (MACl, 99.5%, Xi'an Polymer Light Technology Corp.), CH_3NH_3Br (MABr, 99.5%, Xi'an Polymer Light Technology Corp.), caesium iodide

(CsI, 99.999%, Sigma-Aldrich), 2,2',7,7'-Tetrakis-(*N,N*-di(4-methoxyphenyl)amino)-9,9'-spirobifluorene (spiro-OMeTAD, 99.5%, Xi'an Polymer Light Technology Corp.), isopropanol (IPA, 99.5%, J&K Scientific), *N,N*-dimethylformamide (DMF, 99.8%, Sigma-Aldrich), chlorobenzene (99.8%, Sigma-Aldrich), dimethyl sulfoxide (DMSO, 99.9%, Sigma-Aldrich), acetonitrile (99.95%, Sigma-Aldrich), lithium bis-(trifluoromethanesulfonyl)imide (Li-TFSI, 99.95%, Sigma-Aldrich), and 4-tert-Butylpyridine (tBP, 98%, Sigma-Aldrich).

3.1.2 Device fabrication

The substrate (glass/ITO) was cleaned by sonication in acetone, detergents/H_2O, distilled water and isopropanol for 25 min sequentially, which was then dried by N_2 blowing and treated by UV-ozone for 25 min. The SnO_2 colloidal solution was diluted by H_2O to 2.67% and filtered by a nylon filter (0.22 μm) before use. For ETL, SnO_2 precursor solution was spin-coated at 3000 rpm for 30 s and then annealed at 150 ℃ for 30 min. The resultant SnO_2 layers were treated by UV-ozone for 15 min before the deposition of perovskite films. Note that all of the steps above were carried out under ambient air without controlling temperature and relative humidity of the environment. Then the samples were transferred to a glove box to prepare perovskite films. 1.3 M PbI_2 and 0.13 M CsI were dissolved in mixed solvent (DMF: DMSO, volume ratio = 0.95: 0.05) and stirred at 75 ºC for 8 h. The precursor solution was spin-coated at a speed of 1500 rpm for 30 s and then annealed at 70 °C for 30 min. The solution of FAI:MABr:MACl (60 mg:6 mg:6 mg in 1 ml isopropanol) was spin-coated at 1500 rpm for 30 s, followed by annealing at 150 °C for 20 min in ambient air (40% relative humidity). Subsequently, the spiro-OMeTAD solution in chlorobenzene (90 mg ml^{-1}), in which 10 μl tBP and 45 μl Li-TFSI/acetonitrile (170 mg ml^{-1}) were added, was spin-coated at 3500 rpm for 30 s on the perovskite film. Finally, a 100 nm Ag electrode was prepared via thermal evaporation at 8×10^{-6} mbar, resulting in an active area of 0.1 cm^2.

For the fabrication of PSCs with $FA_xMA_yCs_{1-x-y}Pb(I_zCl_{1-z})_3$ and $FA_xMA_{1-x}Pb(I_zBr_kCl_{1-z-k})_3$ perovskite films, MABr, and CsI are removed from the perovskite precursor solution, respectively. For the fabrication of PSCs with the PEDOT:PSS and $PC_{61}BM$ films as the HTL and ETL, respectively, the PEDOT: PSS solution was spin-coated at 3000 rpm for 30 s and then annealed at 150 °C for 15 min, and the $PC_{61}BM$ solution (15 mg ml^{-1} in chlorobenzene) was spin-coated onto perovskite films at a speed of 3000 rpm for 30 s. For the fabrication of $MAPbI_3$ layer, the perovskite precursor

solution with a concentration of 550 mg ml^{-1} (molar ratio between CH_3NH_3I and PbI_2 is 1: 1) was spin-coated at 4000 rpm for 40 s, during which 65 μl chlorobenzene was dropped to improve the crystallization process. Subsequently, the deposited perovskite layer was annealed at 100 ºC for 10 min. For the fabrication of $PC_{61}BM$ modification layer between SnO_2 and perovskite, the $PC_{61}BM$ solution (10 mg ml^{-1} in chlorobenzene) was spin-coated onto SnO_2 film at 2000 rpm for 30 s and then annealed at 100 ºC for 10 min in a glove box. The carbon electrode was prepared by press transfer technique reported in the literature.[125]

3.1.3 Reverse-biasing experiment

In order to obtain the improvement in device performance, the PSCs were reverse biased for several minutes in dark. Note that the PSCs should be self-stable under ambient air and under repeating *J-V* scans. The whole process was carried out under ambient air (~25 ºC) with controlled relative humidity of ~40%.

The perovskite and SnO_2 films that are used for characterizations, including SEM, X-ray diffraction (XRD), absorption spectra and X-ray photoelectron spectroscopy (XPS), are derived from the PSCs with and without reverse-biasing. Specifically, the silver electrode and spiro-OMeTAD layer are removed by the Scotch type and spin-coating of chlorobenzene for three times, respectively. To expose underneath SnO_2 layers, DMF was subsequently spin-coated on the samples for three times.

3.1.4 Characterization

The absorption properties of perovskite films were measured by UV-vis spectrophotometer (Puxi, T9, China). X-ray diffraction (Rigaku D, Max 2500, Japan) was employed to characterize the crystallographic properties of perovskite. Scanning electron microscope (FEI Helios Nanolab 600i SEM) was utilized to characterize the surface morphology of perovskite films and cross section of the PSC. Electrochemical impedance spectroscopy (EIS, CHI606D, Chenhua, Shanghai) was employed to investigate the electrical dynamics of PSCs. X-ray photoelectron spectroscopy (XPS, Al Kα X-ray source, 1486.6 eV) was used to characterize elemental changes of perovskite and SnO_2 films. Capacitance-voltage (C-V) curves were measured under dark at a frequency of 5 kHz. Transient photovoltage (TPV, Keysight DSO-X 3104A, NL100, 500 nm) decay and photocurrent (TPC, Keysight DSO-X 3104A, 1 MW and

50 W) decay were utilized to investigate the carrier transport and recombination properties. External quantum efficiency (EQE) spectra were measured using a Saifan (Beijing) EQE measurement system. *J-V* curves of the cells were measured from +1.2 V to 0 V (50 ms scanning delay, 60 points, about 100 mV s^{-1} scan rate) by a digital Source Meter (Keithley, model 2420). A Xenon-lamp-based solar simulator (Newport 91160s, AM 1.5G) with a light intensity of 100 mW cm^{-2} was calibrated by a standard silicon solar cell before the measurements.

3.1.5 Computational methods

The first-principles calculations were performed using the Vienna Ab initio Simulation Package (VASP) based on density functional theory (DFT) with generalized gradient approximation (GGA) of a Perdew Burke Ernzerhof (PBE) functional.[126,127] Valence Core interactions were described by projector-augmented-wave (PAW) pseudopotentials.[128] The simulations used 350 eV plane-wave energy cutoff and Gamma point representing the Brillouin zone integrations. All Atomic positions were fully relaxed, until the total force on each atom was less than 0.03 eV/Å and the total energy change was less than 1×10^{-4} eV. We used a 4×2 supercell of (110)-plane rutile SnO_2, and a 2×2 supercell of (001)-plane cubic $FAPbI_3$ surfaces. A vacuum space was set to about 15 Å in the Z direction to minimize the artificial interlayer interactions.

3.1.6 Statistical analysis

No pre-processing was used for data of statistical analysis. Data presentation was exhibited as the mean ± SD. Sample size (n) was shown in the corresponding table. Statistical analysis was performed using Origin 2021.

3.2 Results and discussion

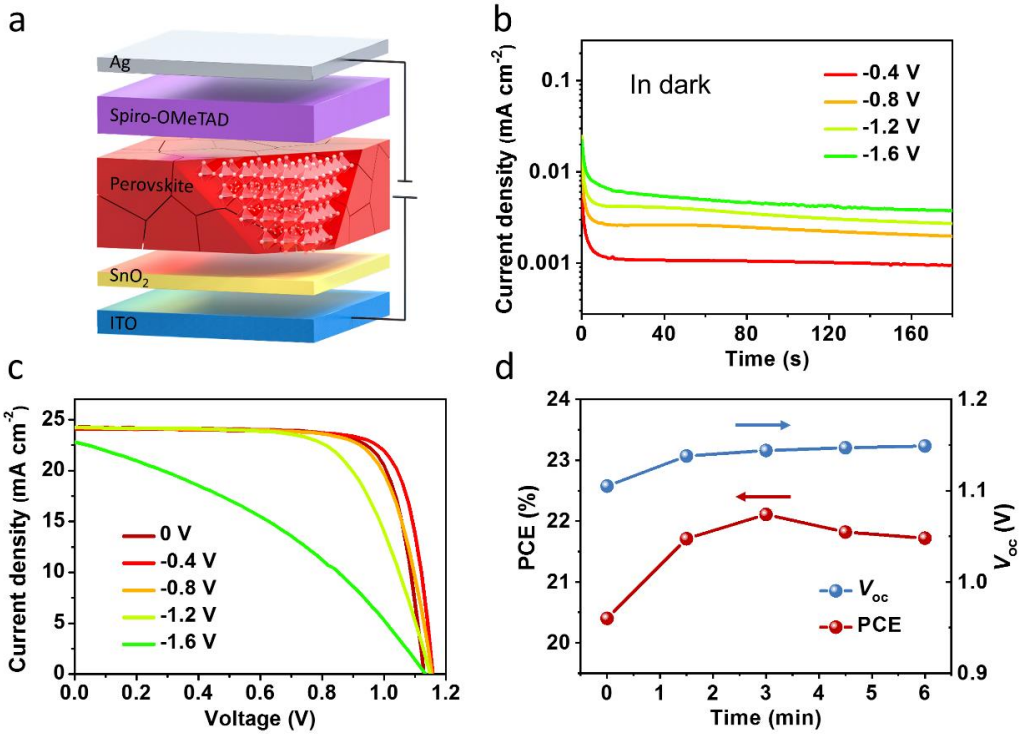

Figure 3.1. *(a) Schematic of the PSC under reverse bias, with a planar heterojunction structure of ITO/SnO_2/Perovskite/spiro-OMeTAD/Ag; (b) monitoring of current densities of the PSC under different reverse bias voltages in dark; (c) reverse scanned J-V curves of the PSC after reverse-biasing at different voltages for 3 minutes; (d) PCE and V_{oc} of a PSC after reverse-biasing at -0.4 V for the different time.*

Figure 3.1a shows the cell configuration in this work, namely ITO/SnO_2/$FA_{0.945}MA_{0.025}Cs_{0.03}Pb(I_{0.975}Br_{0.025})_3$/spiro-OMeTAD/Ag, which is a typical high-performance planar heterojunction PSC.[129,130] While the PSC is under reverse bias, the front ITO and rear Ag electrode contacts are connected to positive and negative terminals of external power supply, respectively. As shown in Figure 3.1b, the reverse current first decreases and then tends to be stable, which is consistent with the published result and will be discussed later.[131] In addition, the current grows with the increase of the reverse voltage due to enhanced electronic and ionic currents under higher electric field. Moreover, it is found that the photovoltaic performance of PSCs is changed obviously after the devices are subjected to reverse bias for 3 minutes in dark. As shown in Figure 3.1c, the device performance is improved after the reverse-biasing at -0.4 V for 3 minutes, mainly coming from the enhancement in V_{oc}. Overall, the efficiency (V_{oc}, J_{sc} and fill factor (FF)) of the PSC increases from the initial 20.50% (1.11 V, 24.24 mA

cm^{-2} and 76.02%) to 21.95% (1.16 V, 24.09 mA cm^{-2} and 78.78%).

However, when the reverse bias exceeds -0.8 V, the device performance gradually decreases. This result is consistent with previous reports, in which ion migration, phase segregation and the formation of highly conductive shunts due to silver melting or metal migration induced by reverse bias reduce the performance of PSCs.[100,101] The statistical results of device performance after reverse-biasing at the different voltages further confirm the tendency above (Table 3.1). Besides, the effect of loading time under reverse bias is investigated. As shown in Figure 3.1d, the V_{oc} first increases with the time under -0.4 V reverse bias, and it becomes stable after 3 minutes. The efficiency also increases with the time under -0.4 V reverse bias, but it peaks at 3 minutes and then decreases over time. Although the changes in J_{sc} and FF are not remarkable during the whole period, prolonged reverse-biasing results in a decrease in FF. It should be attributed to the degradation of the perovskite triggered by ion migration under electric field.

Table 3.1. *Performance data for PSCs before and after reverse-biasing at different voltage for 3 min. The statistics are based on 10 cells.*

Voltage (V)	V_{oc} (V)	J_{sc} (mA cm^{-2})	FF	PCE (%)	R_s (kΩ)	R_{sh} (kΩ)
0	1.12 ± 0.02	23.83 ± 0.37	0.764 ± 0.018	20.38 ± 0.56	0.04 ± 0.01	43.41 ± 29.33
-0.4	1.15 ± 0.01	23.84 ± 0.29	0.780 ± 0.011	21.41 ± 0.30	0.03 ± 0.01	127.37 ± 179.79
-0.8	1.14 ± 0.01	23.56 ± 0.46	0.688 ± 0.060	18.55 ± 1.92	0.10 ± 0.07	21.55 ± 10.38
-1.2	1.11 ± 0.05	22.90 ± 1.22	0.565 ± 0.097	14.48 ± 3.54	0.90 ± 1.22	31.28 ± 46.84
-1.6	1.07 ± 0.06	19.59 ± 2.08	0.359 ± 0.034	7.55 ± 1.32	4.83 ± 11.35	2.15 ± 1.22

As mentioned before, the negative effect of reverse bias on PSCs has been reported in the literature.[100-103] However, in this work, the positive effect of reverse bias is discovered. Therefore, this work will mainly focus on the unique and interesting phenomenon and try to explore the potential mechanism. Considering that the device performance can be greatly improved by reverse-biasing at -0.4 V for 3 min, these parameters for reverse-biasing are adopted in subsequent parts, unless otherwise specified.

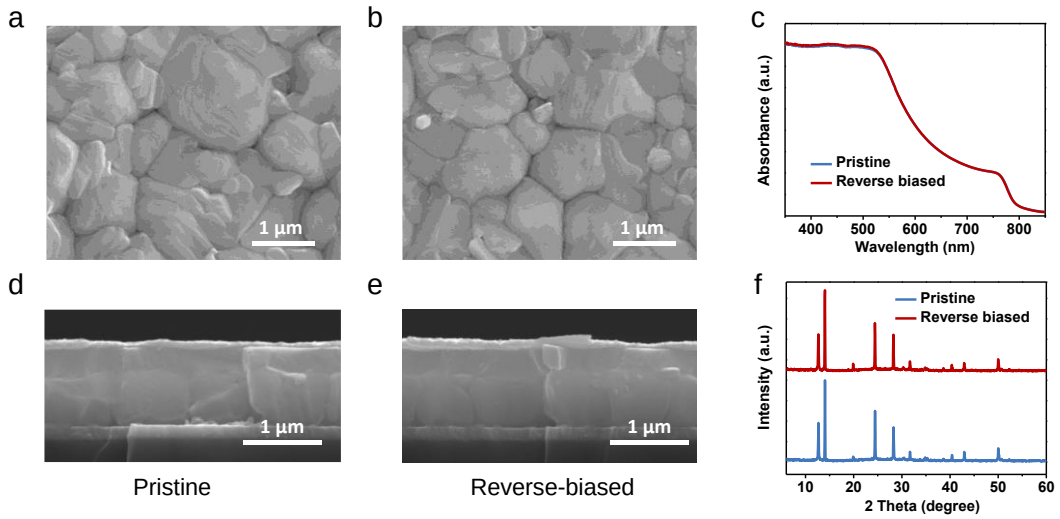

Figure 3.2. *SEM images of the perovskite films (a) without and (b) with reverse-biasing at -0.4 V for 3 min; (c) UV–vis absorption spectra of the perovskite films without and with reverse-biasing at -0.4 V for 3 min; SEM cross-section images of PSCs (d) without and (e) with reverse-biasing at -0.4 V for 3 min; (f) XRD patterns of the perovskite films without and with reverse-biasing at -0.4 V for 3 min. Note that the perovskite films are derived from the PSCs with and without reverse-biasing. Specifically, the silver electrode and spiro-OMeTAD layer are removed by the Scotch type and washing with chlorobenzene, respectively.*

Accordingly, a series of characterizations were carried out. Given the vital role of the perovskite absorber in PSCs, the perovskite layers before and after reverse-biasing were characterized. It is found that the SEM images, absorption spectra and XRD patterns of the perovskite layers are barely changed after reverse-biasing at -0.4 V for 3 min (Figure 3.2). These results suggest that the relatively low reverse voltage does not deteriorate the surface morphology, absorbance, and crystal lattice structure of perovskite. SEM cross-section images of the PSCs indicate that reverse bias has negligible effect on the stack structure and each layer of the cells as well (Figure 3.2d,e).

Electrochemical impedance spectroscopy (EIS) is employed to study carrier dynamics in PSCs. As shown in Figure 3.3a, recombination resistance (R_{rec}) assigned to low-frequency increased in PSCs after reverse-biasing. It indicates that the charge carrier recombination within the cell is suppressed. Additionally, it is found that the charge transfer resistance (R_{tr}) is hardly changed after reverse-biasing. These results are consistent with the change in series resistance (R_s) and shunting resistance (R_{sh}) obtained from *J-V* curves (Table 3.1). Figure 3.3b shows V_{oc} versus light intensity of the PSC before and after reverse-biasing. It suggests that the V_{oc} values increase obviously after reverse-biasing, irrespective of the light intensity. More importantly, the deviation between the slope and the value of (kT/q) decreases significantly after reverse-

biasing, indicating that the trap-assisted recombination is suppressed.[132] In contrast, the slopes between J_{sc} and light intensity are almost identical and very close to 1 (Figure 3.3c), suggesting that the bimolecular recombination is negligible and not affected by the reverse bias.[132]

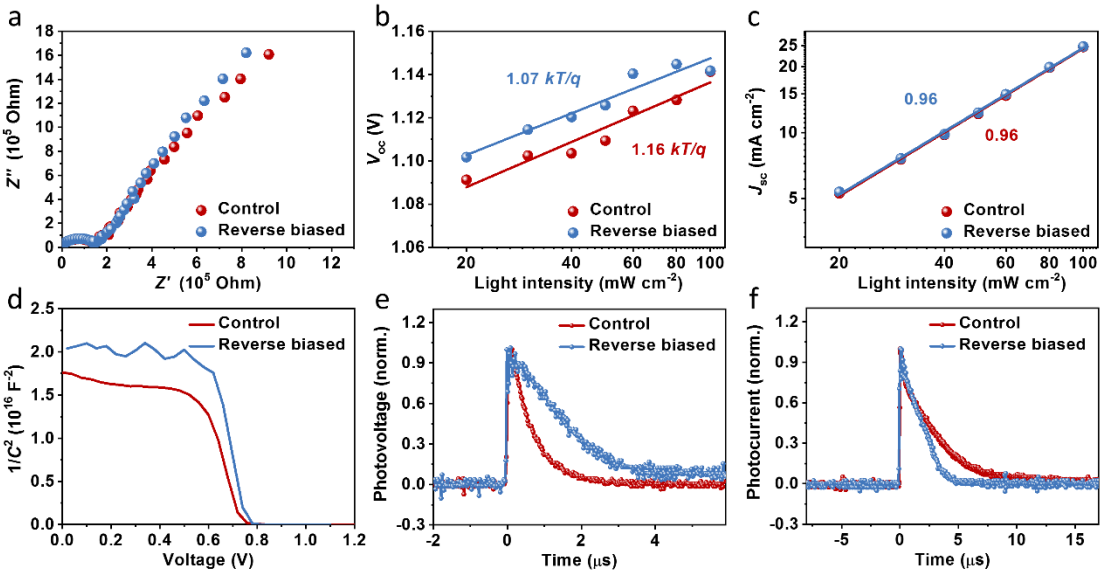

Figure 3.3. *(a) Nyquist plots of the PSC before and after reverse-biasing at -0.4 V for 3 min; the light-intensity dependence of (b) V_{oc} and (c) J_{sc} measurement related to pristine and reverse biased PSCs; (d) Mott-Schottky curves, (e) transient photovoltage decay curves and (f) transient photocurrent decay curves of the PSCs before and after reverse-biasing.*

In addition, the Mott-Schottky curves are obtained in dark via capacitance-voltage measurement to reveal the mechanism for improved V_{oc} and efficiencies. As shown in Figure 3.3d, the built-in field (V_{bi}) of the reverse biased cell is much higher than its initial value, indicating an increased driving force for charge separation and extended depletion region for suppressing the carrier recombination. The larger slope indicates the decreased interfacial charge density, which has an inversely proportional relationship to the slope.[98,133] It should be attributed to the ion migration, improved energy level alignment and accordingly reduced interfacial defects, which will be discussed below. Besides, the transient photovoltage and photocurrent decays are measured at open and short circuit, respectively. It is apparent that the photovoltage decay is slowed down, but the decay of photocurrent is accelerated after reverse-biasing (Figure 3.3e and Figure 3.3f). It suggests that the recombination of charge carriers is suppressed, and the charge extraction and transport are improved.

The results above show that the reverse bias has negligible effect on each layer in PSCs, but improves the device performance and charge carrier dynamics. However, the

mechanism for the improvement in device performance is still not clear. Given that perovskites are ionic materials, ion migration under the external electric field may change the energy band alignment between perovskite and charge transport layers,[106] thus improving device performance. In order to confirm the hypothesis, a series of PSCs based on different structures have been fabricated, and their photovoltaic performance was measured before and after reverse-biasing at -0.4 V for 3 min. The results show that the composition of perovskite does not affect the change in device performance after reverse-biasing (Table 3.2). It indicates that device performance based on this cell configuration can be improved, regardless of the perovskite composition. In contrast, the device performance is deteriorated when $PC_{61}BM$ is used as ETL or to modify SnO_2. Furthermore, the deterioration of device performance is observed in ETL-free PSCs, while the efficiency is still improved in HTL-free PSCs. These results suggest that the SnO_2 or SnO_2/perovskite interface plays a vital role in the improvement of device performance.

Table 3.2. *Performance parameters for PSCs with different structure before and after reverse-biasing at -0.4 V for 3 min. Each result with a specific cell configuration is derived from at least three PSCs.*

Cell configuration	ΔV_{oc} (V)[a]	ΔJ_{sc} (mA cm^{-2})[b]	Δ FF[c]	Δ PCE (%)[d]
ITO/SnO_2/$FA_xMA_yCs_{1-x-y}Pb(I_zBr_kCl_{1-z-k})_3$/spiro-OMeTAD/Ag	0.03	0.01	0.016	1.03
ITO/SnO_2/$FA_xMA_yCs_{1-x-y}Pb(I_zCl_{1-z})_3$/spiro-OMeTAD/Ag	0.03	-0.34	0.007	0.5
ITO/SnO_2/$FA_xMA_{1-x}Pb(I_zBr_kCl_{1-z-k})_3$/spiro-OMeTAD/Ag	0.06	0.28	0.02	1.67
ITO/PEDOT: PSS/$FA_xMA_yCs_{1-x-y}Pb(I_zBr_kCl_{1-z-k})_3$/$PC_{61}BM$/Ag	-0.55	0.073	-0.102	-3.64
ITO/PEDOT: PSS/$MAPbI_3$/$PC_{61}BM$/Ag	-0.34	-2.69	-0.131	-3.67
ITO/SnO_2/$PC_{61}BM$/$FA_xMA_yCs_{1-x-y}Pb(I_zBr_kCl_{1-z-k})_3$/spiro-OMeTAD/Ag	-0.02	-0.13	-0.014	-0.84
ITO/$FA_xMA_yCs_{1-x-y}Pb(I_zBr_kCl_{1-z-k})_3$/spiro-OMeTAD/Ag	-0.02	-0.33	-0.012	-0.34
ITO/$FA_xMA_yCs_{1-x-y}Pb(I_zCl_{1-z})_3$/spiro-OMeTAD/Ag	-0.02	-0.39	-0.024	-0.84
ITO/$FA_xMA_{1-x}Pb(I_zBr_kCl_{1-z-k})_3$/spiro-OMeTAD/Ag	-0.04	-0.29	-0.031	-1.00
ITO/SnO_2/$FA_xMA_yCs_{1-x-y}Pb(I_zBr_kCl_{1-z-k})_3$/Carbon	0.03	0.83	0.049	1.35

a) $\Delta V_{oc} = V_{oc\ pristine} - V_{oc\ reverse\ biased}$

b) $\Delta J_{sc} = J_{sc\ pristine} - J_{sc\ reverse\ biased}$

c) Δ FF= $FF_{pristine} - FF_{reverse\ biased}$

d) Δ PCE = $PCE_{pristine} - PCE_{reverse\ biased}$

Figure 3.4a shows the current change of the PSCs under -0.4 V and different temperature in dark. They can be well fitted by the following equation.

$$I = I_0 + I_1 exp(-k_1 t) + I_2 exp(-k_2 t) \quad (3\text{-}1)$$

It has been reported that the capacitance of PSCs is very small (~10^{-2} μF).[134] Therefore, the rapid decrease at the beginning of the *I-t* curves should be attributed to the capacitive effect of PSCs, corresponding to the small value of k_1. The following part of the slow decay should result from ion migration under reverse bias. Accordingly, the Arrhenius plot of current decay velocity k_2 and the inverse time constant calculated from the *I-t* curves are shown in Figure 3.4b. The activation energy calculated from the slope of the curve is 0.17 eV. It only matches the activation energies of iodine ions and iodine interstitials, while the activation energy of other mobile ions in perovskites is much higher than this value (Figure 3.4c).[135-137] It further confirms the speculation that iodine ion migration occurs in PSCs under reverse bias in dark.

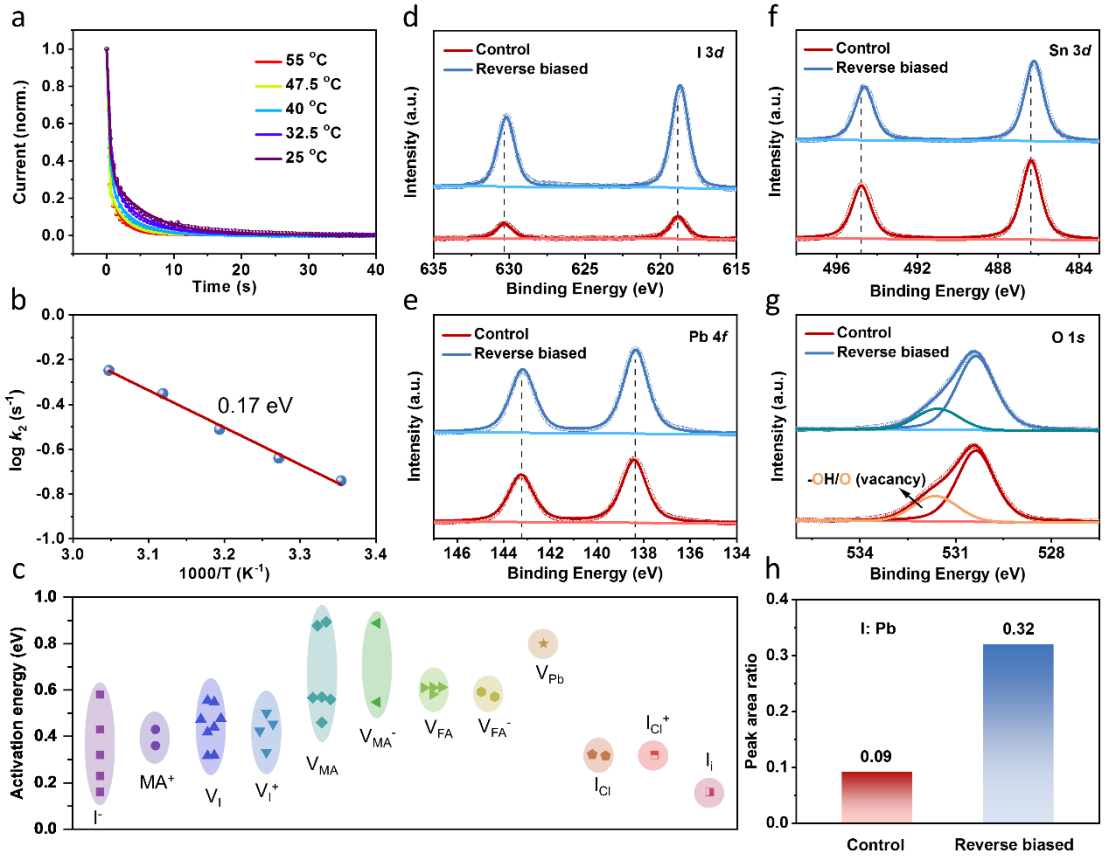

Figure 3.4. *(a) Current change of the PSCs under -0.4 V and different temperature in dark; (b) the Arrhenius plot of the time constant; (c) activation energy of different type of ions in perovskite; XPS spectra of (d) I 3d, (e) Pb 4f, (f) Sn 3d and (g) O 1s of SnO_2 films; (h) peak area ratio between I 3d and Pb 4f of SnO_2 films before and after reverse-biasing at -0.4 V for 3 min.*

Figure 3.4d-g show the XPS spectra of the SnO_2 layers before and after reverse-biasing. It is noticed that the SnO_2 films are derived from complete PSCs (see more details in 3.1.3 Reverse-biasing experiment). The result shows that the intensity of I 3d peaks in reverse biased sample is much stronger than that of control sample, while the differences in the intensities of Pb 4f and Sn 3d peaks between the control and reverse-biased sample are negligible, leading to the increase in the ratio of I:Pb (Figure 3.4h). It is assumed that I 3d and Pb 4f peaks in the control sample should be attributed to residual perovskite or lead iodide. The results suggest that reverse bias contributes to the increase of iodine content in SnO_2 layers or SnO_2/perovskite interface. It should be ascribed to the directional migration of iodine ions within PSCs under the electric field caused by reverse bias. Also, the shift of peak locations of I 3d and Sn 3d is observed after reverse-biasing. It further confirms that the migrated iodine ions would interact with SnO_2, which is similar to the newly formed F-Sn and Cl-Sn bonds.[138-140] O 1s peaks show the suppressed oxygen vacancies in the SnO_2 layers after reverse-biasing, due to formed I-Sn bonds (Figure 3.4g).[139,140] The XPS spectra of other elements including C, N, Br, Cl, Li and Na have hardly changed after reverse-biasing. XPS spectra of the perovskite layers before and after reverse-biasing are also measured. No obvious changes can be observed in these XPS spectra, indicating that the influence of reverse bias on the upper surface of perovskite and perovskite/spiro-OMeTAD interface is negligible.

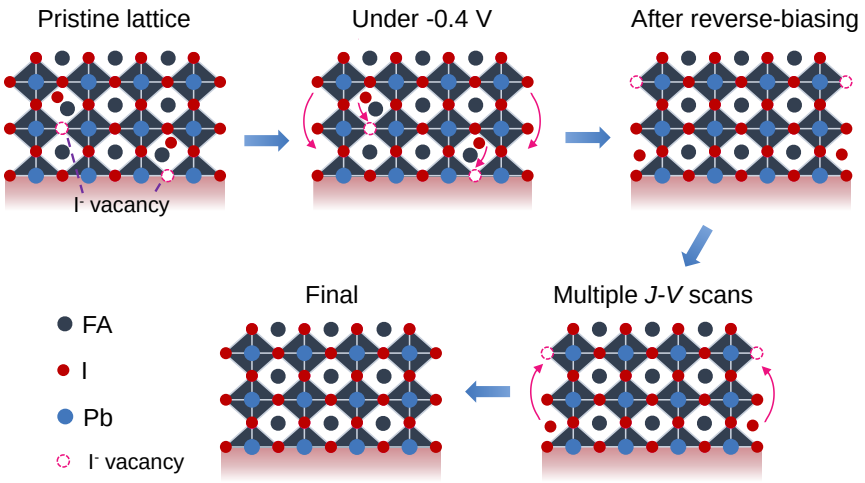

Figure 3.5. *Schematic illustration of ion migration within perovskites under reverse bias and subsequent J-V scans.*

It is assumed that iodine ions including iodine interstitials migrate and ultimately accumulate at the SnO_2/perovskite interface under reverse bias. During this period,

parts of these iodine ions will fill the iodine vacancies at the interface, as shown in Figure 3.5. Although most of the ions will return to the perovskite bulk after reverse-biasing, the iodine ions filling the vacancies will be anchored by these traps due to lower energy position. The interaction with SnO_2 also makes these iodine ions at the interface more stable. It means these ions will stay at the interface and help to reduce interfacial trap-state density and suppress charge carrier recombination. It is important to point out that multiple *J-V* scans are necessary after reverse-biasing to stimulate the return of excessive ions accumulated at the interface back to the perovskite bulk (Figure 3.5). However, *J-V* scans do not enhance the device performance without prior reverse-biasing treatment. More data and discussion related to this will be presented later.

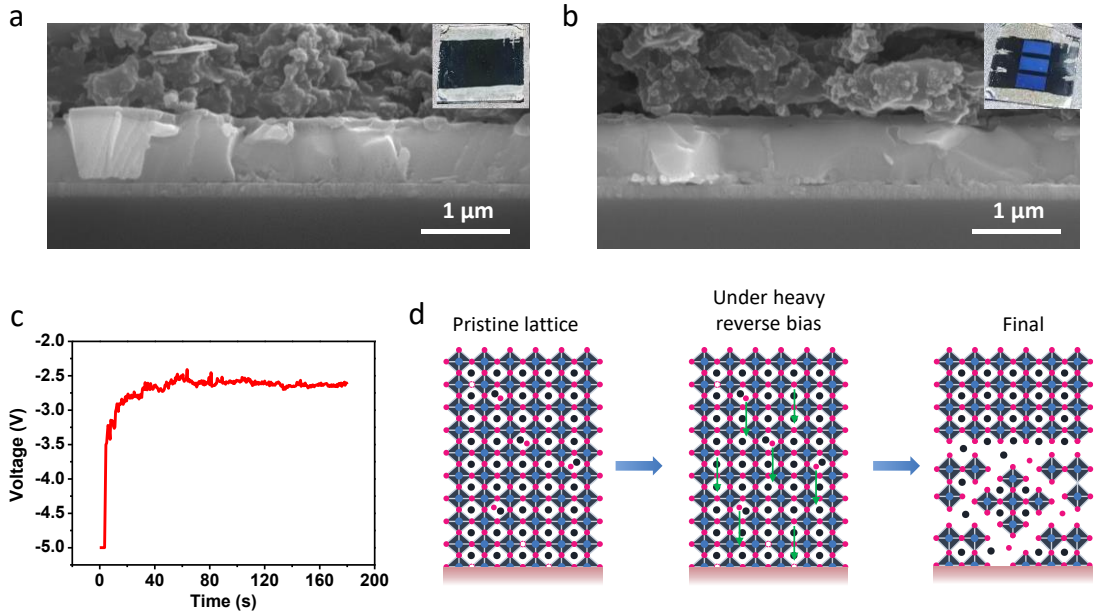

Figure 3.6. *SEM cross-section images of the PSCs (a) without and (b) with reverse-biasing under constant reverse current density of -10 mA cm^{-2} for 3 min; (c) voltage of the PSCs under constant reverse current density of -10 mA cm^{-2} for 3 min (the limiting voltage is 5 V); (d) schematic illustration of the evolution of perovskites under heavy reverse bias. Insets in (a) and (b) show the photographs of the PSCs without and with reverse-biasing, respectively. Note that cell configuration of ITO/SnO_2/$FA_{0.945}MA_{0.025}Cs_{0.03}Pb(I_{0.975}Br_{0.025})_3$/spiro-OMeTAD/Carbon is adopted to avoid the effect of Ag electrode during reverse-biasing. Also, the thickness of spiro-OMeTAD is decreased to obtain better device performance.*

When the PSCs are subjected to heavy reverse voltage, a large number of iodine ions will accumulate at the SnO_2/perovskite interface, leading to the degradation of perovskite into tiny particles at the interface (Figure 3.6). These accumulated ions would weaken the bond bonding between FA^+ cations and I^- anions within the perovskite lattice, which is deemed to be significant for the stability of the perovskite

structure.[141] These results may account for the deterioration of device performance after reverse-biasing at -1.2 V and -1.6 V.

The above experimental results confirm the positive effect of reverse-biasing at -0.4 V. Accordingly, the champion PSC is achieved by using this strategy, in which the efficiency increases from the initial 22.13% (V_{oc}=1.10 V, J_{sc}=24.91 mA cm^{-2} and FF=0.806) to 23.48% (V_{oc}=1.16 V, J_{sc}=24.85 mA cm^{-2} and FF=0.816), as shown in Figure 3.7a. The integrated current density (23.94 mA cm^{-2} and 24.01 mA cm^{-2} for pristine and reverse biased cell) derived from EQE spectra are consistent with the J_{sc} obtained from the *J-V* curves (Figure 3.7b).

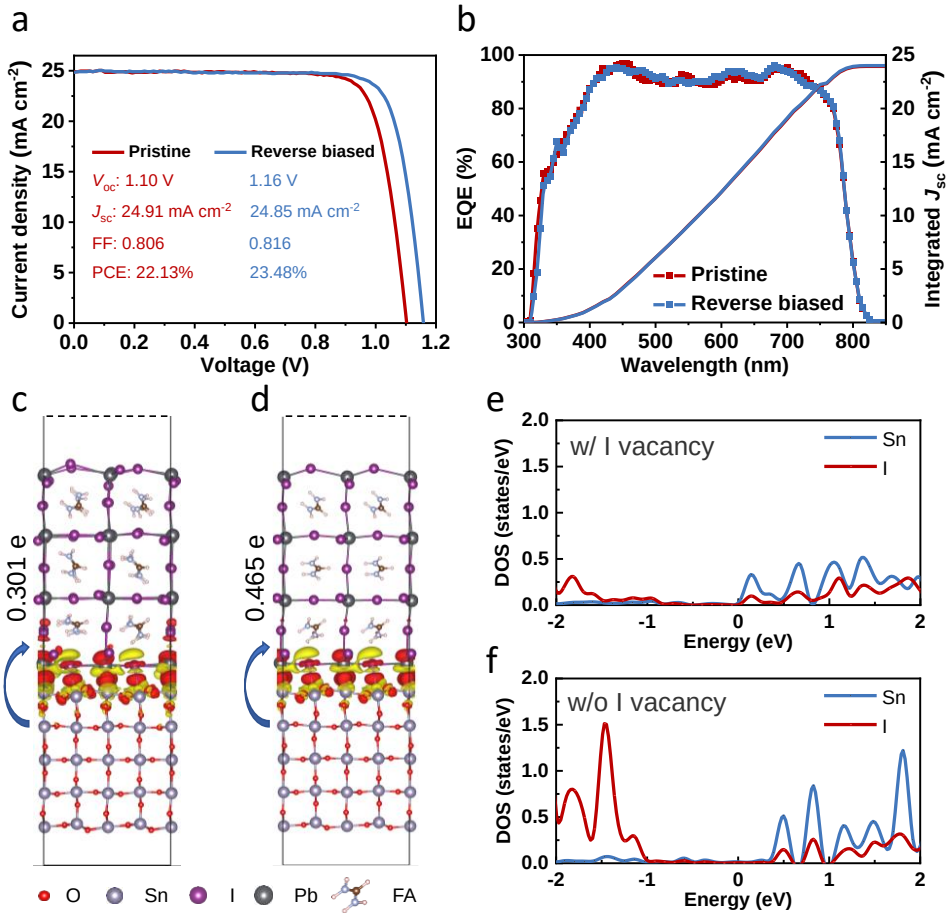

Figure 3.7. *(a) J-V curves of the champion PSC before and after reverse-biasing at -0.4 V for 3 min; (b) EQE spectra of the champion PSC before and after reverse-biasing at -0.4 V for 3 min. Charge density difference coupling with Bader charge analysis (c) with and (d) without I vacancy. Red represents electron accumulation, and yellow represents electron depletion. Density of states of Sn ion and I ion at the SnO_2/perovskite interface (e) with and (f) without I vacancy. The Fermi level is set to 0 eV.*

In order to obtain more information about how migrated iodine ions under reverse bias affect the performance of SnO_2/perovskite interface, first-principles calculations of

SnO_2/perovskite interfaces with and without I vacancy are performed. The charge transfer at the SnO_2/perovskite interfaces with and without I vacancy are shown in Figure 3.7c and Figure 3.7d, respectively. Red represents electron accumulation, and yellow represents electron depletion. The results reveal that a stronger interaction at the SnO_2/perovskite interface is obtained. The Bader charge analysis shows that the electrons flow spontaneously from SnO_2 to perovskite at the interface, which creates a built-in electric field that points from SnO_2 to perovskite. A higher charge transfer at the interface without I vacancy (0.465 e) than that at the interface with I vacancy (0.301 e) demonstrates stronger built-in electric field and better carrier transport capacity at the former interface, which is consistent with experimental results above. The density of states (DOS) of Sn ion and I ion at the SnO_2/perovskite interfaces with and without I vacancy are shown in Figure 3.7e and Figure 3.7f, respectively. The Fermi level is set to 0 eV. The strong orbital coupling between Sn ion and I ion shows that the Sn-I bonds are formed at the interface, which is consistent with the XPS results, facilitating carrier transport at the interface. The orbital coupling at the interface without I vacancy is stronger than that with I vacancy, which demonstrates better carrier transport capacity.

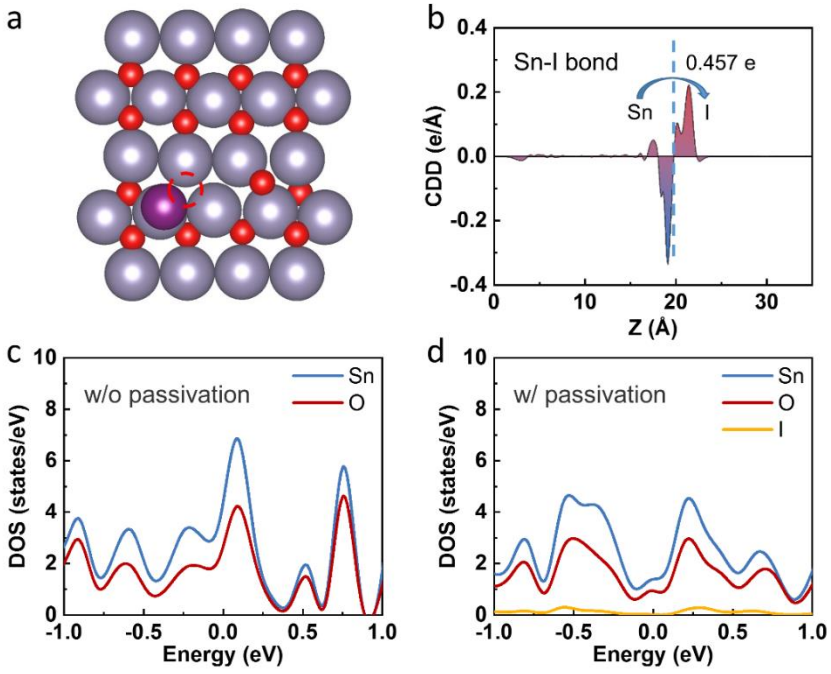

Figure 3.8. *(a) Structure model of relaxed SnO_2 surface with I ion passivating O vacancy. The ions of Sn, O and I are indicated by grey, red and purple balls, respectively. The red dotted circle represents O vacancy. (b) Plane-averaged charge density difference along the Z direction coupling with Bader charge analysis. The dotted blue line represents the middle of Sn-I bond axis. DOS at the SnO_2 surface (c) without and (d) with I ion passivation. The Fermi level is set to 0 eV.*

Previous result shows that the iodide could be driven into the ETL.[100] Iodine ions may migrate through grain boundaries or amorphous regions of polycrystalline films of perovskite and SnO_2, which have been recognized as the main channel of ion migration.[142] Thus, the mechanism how iodine ions crossing the SnO_2/perovskite interface affect the performance of SnO_2 ETL is also explored by using first-principles calculations. It is found that incorporating an I ion into the SnO_2 lattice is very difficult, and it extremely prefers to stay at the surface of SnO_2. Figure 3.8a shows the structure model of relaxed SnO_2 surface with I ion passivating O vacancy, and the I ion is attached to the Sn ion. The plane-averaged charge density difference (CDD) along the direction perpendicular to the surface coupling with Bader charge analysis at SnO_2 surface is calculated, as shown in Figure 3.8b. The I ion gains a lot of electrons, while the Sn ion loses electrons. It shows that the strong Sn-I ionic bond is formed at the O vacancy. The DOS at the SnO_2 surface without and with I ion passivation are shown in Figure 3.8c and Figure 3.8d, respectively, and the Fermi level is set to 0 eV. The surface gap states (as the DOS around the Fermi level) with I ion passivation are smaller than those without I ion passivation. Such weakened surface gap states indicate the reduced carrier recombination at the surface region, which is beneficial to improve the PCEs.

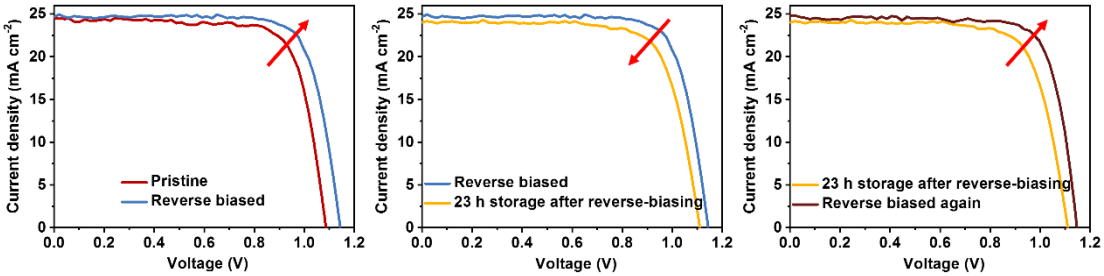

Figure 3.9. *Evolution of J-V curves of the PSC after reverse-biasing and storage in nitrogen.*

It should be pointed out that the performance enhancement induced by reverse-biasing is not permanent or irreversible. The device performance will return to the initial value after being stored in nitrogen for 23 hours, but the performance can be enhanced again by reverse-biasing after the storage (Figure 3.9). It further confirms that the phenomenon found here should be closely related to ion migration. Also, the device performance cannot be improved directly after reverse-biasing, because the ions accumulated at the interface need to migrate back to their own sites. Therefore, multiple *J-V* scans are needed. During this period, the device performance increases gradually and finally stabilizes at a higher value than the initial efficiency (Figure 3.10).

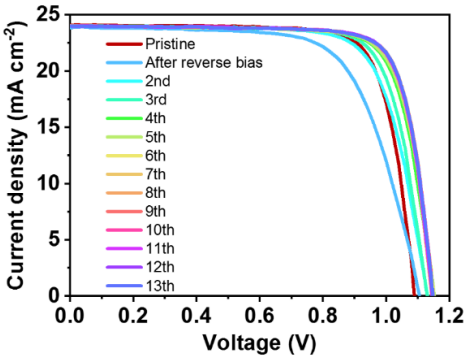

Figure 3.10. *J-V curves for the reverse biased PSC under repeating tests of J-V curves.*

It is noted that the improvement after reverse-biasing cannot be caused by measuring conditions. Generally, PSCs reach the highest efficiency after several *J-V* scans, and will decay or remain stable in subsequent *J-V* scans, as shown in Figure 3.11a-c. The phenomenon observed here is that a higher PCE than the original maximum efficiency can be obtained after reverse-biasing. During all of these *J-V* scans, the measuring conditions are consistent, including light intensity, scan rate, ambient temperature and relative humidity. Apart from that, the enhancement cannot be explained by short-term storage (3 min) in dark, since the device performance is not improved after short-term storage, as shown in Figure 3.11d-f. The phenomenon has been confirmed multiple times, and the results suggest that the improvement in device performance is due to reverse-biasing.

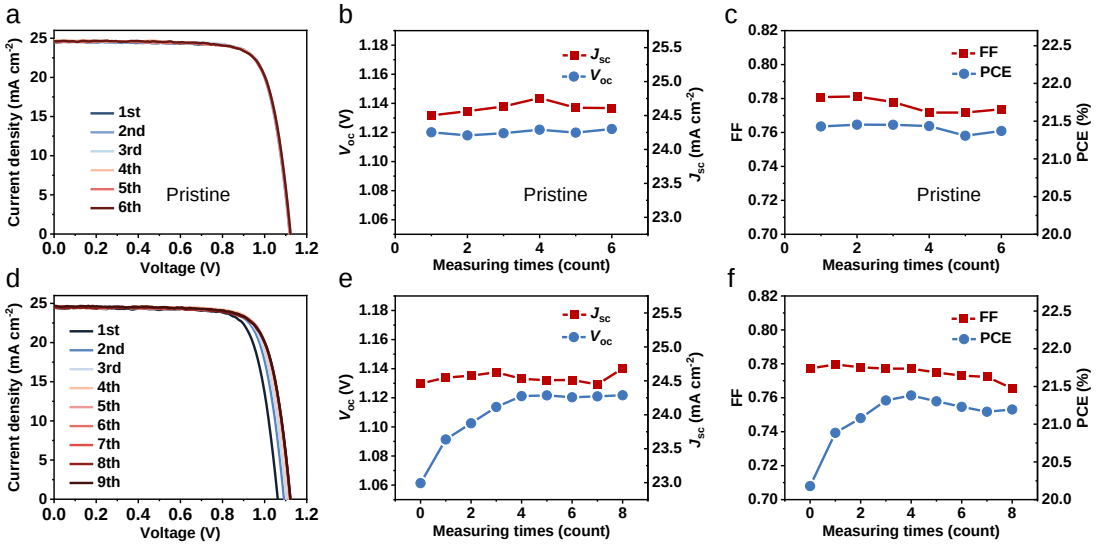

Figure 3.11. *(a) J-V curves, (b) the change in V_{oc} and J_{sc}, (c) the change in FF and PCE of the PSC with repeating J-V scans; (d) J-V curves, (e) the change in V_{oc} and J_{sc}, (f) the change in FF and PCE of the PSC after short-term storage in dark for 3 min. It is noted that these results are derived from the same PSC.*

The research work shows several implications for the whole perovskite community. (*i*) special treatment of PSCs, such as extra light soaking or reverse-biasing, before the scanning of *J-V* curves should be elaborated; (*ii*) ion migration can be utilized to realize the doping or passivation of perovskite, ETL and HTL under external electric field; (*iii*) the materials containing mobile ions can be used as doping for functional films or other materials under external forward or reverse voltage, which could be extended to other research fields such as light emitting diodes, transistors and memristors.

3.3 Conclusion

In summary, the performance of PSCs can be improved by reverse-biasing and its mechanism has been unveiled. The electric field induced by reverse bias will drive ions to move directionally in perovskite films and accumulate at the interface. Part of accumulated iodine ions will fill the I vacancy at the interface and interact with SnO_2, even after reverse-biasing. First-principles calculations prove that the SnO_2/perovskite interface without I vacancies has a higher charge transfer and stronger orbital coupling between Sn ions and I ions, resulting in greater built-in electric field and better carrier transport capacity. When the iodine ions migrate into SnO_2 layers under reverse bias, the strong Sn-I ionic bond is formed at the O vacancy, leading to reduced surface gap states and suppressed charge carrier recombination on SnO_2 surface. According to this strategy, a PCE of over 23% was achieved with a simple planar heterojunction structure, indicating obvious enhancement in efficiency from 22.13% for the reference device. The research work not only brings interesting phenomena to perovskite community, but also provides a new idea and route for utilizing the ion migration and improving the photovoltaic performance and stability of PSCs.

CHAPTER 4

4 Universal strategy with structural and chemical crosslinking interface for efficient and stable perovskite solar cells

According to the results above, the interface (including the SnO_2/perovskite interface) in perovskite solar cells profoundly influences device performance and stability. In this chapter, we propose a universal strategy to enhance the interface between SnO_2 and perovskite. By introducing an additional SnO_2 layer mixed with chloride salt, we observed significant improvements in conductivity without adversely affecting the morphology or crystallinity of SnO_2. Additionally, this approach resulted in reduced trap-state densities in perovskite films and improved energy level alignment between SnO_2 and perovskite. Consequently, perovskite solar cells with the SnO_2/chloride salt layer demonstrated better efficiencies and operational stability compared to control samples. This chapter offers a promising strategy for optimizing perovskite solar cell interfaces, thus advancing their practical applications.

4.1 Introduction

PSCs have been developed rapidly due to the evolution of perovskite films and charge transport layers.[6,143] Generally, there are lots of undercoordinated halide ions and undercoordinated Pb^{2+} ions on the surface of perovskite films,[104] which lead to deep energy level traps and charge carrier recombination centres and deteriorate the photovoltaic performance of PSCs. To solve this problem, 2D perovskite and some other materials such as inactive $(PbI_2)_2RbCl$ and poly(methyl methacrylate) (PMMA) have been applied to the upper surface of perovskite.[51,144-147] These materials passivate the undesired defects via coordinate or ionic bonding. Also, additive engineering has

been employed to perovskite films for some particular purposes including crystallization control and stability enhancement.[70,148]

The rapid development of PSCs also relies on continuous exploration of ETL and HTL. Amongst numerous electron transport materials including TiO_2,[143] ZnO,[47,149] Nb_2O_5,[150] and $PC_{61}BM$,[151] SnO_2 exhibits promising prospects due to its low-temperature solution processibility, intrinsic stability under ultraviolet light, a high mobility up to 240 cm^2 $(V\ s)^{-1}$, inert nature with respect to perovskite, excellent electrical and optical properties.[152,153] Similarly, interface engineering has also been introduced into the SnO_2/perovskite interface. Various materials, such as 4-imidazoleacetic acid hydrochloride (ImAcHCl),[154] 1′2-dichlorobenzene,[155] potassium chloride,[156] rubidium fluoride,[138] $PC_{61}BM$,[151] and biguanide hydrochloride (BGCl),[140] have been introduced. They can act as a linker between SnO_2 and perovskite to assist the charge transfer and reduce interfacial defects, and passivate the iodine vacancies of perovskites at the interface through excess halide ions. Apart from that, additive engineering can be utilized in SnO_2 layers. NH_4Cl,[157] cobalt chloride hexahydrate ($CoCl_2 \cdot 6H_2O$),[158] ethylene diamine tetraacetic acid (EDTA),[132] and heparin potassium,[159] have been employed to improve the electrical properties of SnO_2 or energy level alignment. These strategies focusing on SnO_2/perovskite interface or underlying SnO_2 layers generally affect the quality of perovskite films, so some volatile additives or with low boiling point, such as formamidinium iodide (FAI),[160] and ammonium formate ($HCOONH_4$),[161] can be pre-deposited in SnO_2 layers to improve perovskite quality and enhance interfacial contact. However, all these works were constrained by inherent features of the planar heterojunction of PSCs in which the weak bonding at the SnO_2/perovskite interface and limited contact area would hinder the extraction and transport of charge carriers.[162,163] Delamination between SnO_2 and perovskite can occur, especially during the bending process of flexible PSCs, leading to inferior stability of the cells.[160,161] Therefore, it is critical to propose universal methodology to enhance the interfaces and further stability of PSCs.

Herein, we adopted a double-layer SnO_2 structure and introduced methylenediammonium dichloride ($MDACl_2$) in the second layer. The added material can be dissolved by the perovskite precursor solution, allowing for the construction of structural crosslinking of the SnO_2/perovskite interface. Characterization suggests that residual chlorine ions contribute to the improved conductivity of SnO_2, and enhance the interaction between Sn ions in SnO_2 and halogen ions in perovskite, thereby stabilizing

the SnO_2/perovskite interface. This strategy also led to an improved energy level alignment between SnO_2 and perovskite, due to the downward shift of the conduction band of SnO_2. In addition, the incorporation of $MDACl_2$ improved the quality of perovskite films and reduced the trap-state density of perovskite. The V_{oc} and FF of the PSCs were significantly improved with this strategy. Other chloride salts can be used to replace $MDACl_2$, thereby bringing positive effects on device performance as well. After storage of 11208 h in dry air conditions (relative humidity of ~5% and ~25 °C), the PSCs with the enhanced crosslinking interface maintained 98% of their efficiency. The champion cell utilizing a low bandgap perovskite exhibited an impressive efficiency of 25.28%. This work provides a meaningful direction for further enhancing the interface stability and efficiency of PSCs.

4.2 Experimental section

4.2.1 Materials

All materials were used directly after purchase. SnO_2 precursor (15% in H_2O colloidal dispersion) was from Alfa Aesar. $HC(NH_2)_2I$ (FAI), CH_3NH_3Cl (MACl), CH_3NH_3Br (MABr), 4-methylphenethylammonium chloride (4M-PEACl), phenethylammonium chloride (PEACl), phenethylammonium iodide (PEAI) were from Greatcell Solar. Lead iodide (PbI_2) was from Tokyo Chemical Industry (TCI). Caesium iodide (CsI), methylenediamine dihydrochloride ($MDACl_2$), caesium chloride (CsCl), rubidium chloride (RbCl), *N,N*-dimethylformamide (DMF), isopropanol (IPA), chlorobenzene, dimethyl sulfoxide (DMSO), acetonitrile, lithium bis-(trifluoromethanesulfonyl)imide (Li-TFSI), and 4-tert-Butylpyridine (tBP) were from Sigma-Aldrich. 2,2',7,7'-Tetrakis-(*N,N*-di(4-methoxyphenyl)amino)-9,9'-spirobifluorene (spiro-OMeTAD) was from Lumtec. Poly[bis(4-phenyl)(2,4,6-trimethylphenyl)amine] (PTAA) was from EMNI.

4.2.2 Device fabrication

Glass/ITO was sequentially cleaned by sonication in detergents/H_2O, deionized water, acetone, isopropanol, and ethanol for 50 min, and then dried by N_2 and treated by UV-ozone for 30 min. The SnO_2 colloidal precursor was diluted by deionized water and filtered by a nylon filter (0.22 μm). SnO_2 colloidal precursor was spin-coated at

3000 rpm for 30 s, and then annealed at 150 °C for 30 min in ambient air. The concentration of SnO_2 solution is 3.17% and 2.5% for control and target cells. The second layer for target cells was prepared with the mixture of SnO_2 (3.17%) and $MDACl_2$ (1.5 mg/ml) by spin-coating at 3000 rpm for 30 s, and then annealed at 100 °C for 10 min. For the champion PSC, the concentration of SnO_2 used for the second layer was reduced to 1%. The results of optimizing the concentration of $MDACl_2$ are shown in Figure 4.1a and Table 4.1; the results of optimizing the concentration of SnO_2 used for the second layer are shown in Figure 4.1b and Table 4.2. For the PSCs with the incorporation of other additives (including MACl, CsCl, 4M-PEACl and PEACl) in the second layer, the concentration of these additives is 1 mg/ml. Control samples were subjected to UV-ozone treatment for 30 min before the deposition of perovskite, while target samples had no treatment.

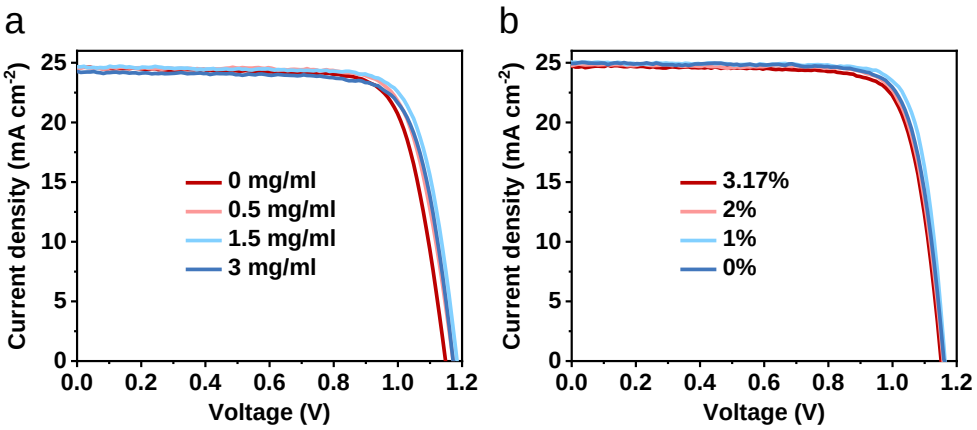

Figure 4.1. *(a) J–V curves of the PSCs with different concentration of $MDACl_2$ in the second layer of SnO_2 (herein, the concentration of SnO_2 for the first and second SnO_2 layer is 2.5% and 3.17%, respectively); (b) J–V curves of the PSCs with different concentration of SnO_2 for the second layer of SnO_2 (herein, the concentration of SnO_2 for the first SnO_2 layer is 2.5% and the concentration of $MDACl_2$ in the second layer of SnO_2 is 1.5 mg/ml).*

Table 4.1. *Performance data for PSCs with different concentration of $MDACl_2$ in the second layer of SnO_2. Herein, the concentration of SnO_2 for the first and second SnO_2 layer is 2.5% and 3.17%, respectively.*

Concentration (mg/ml)	V_{oc} (V)	J_{sc} (mA cm^{-2})	FF	PCE (%)
0	1.147	24.61	0.762	21.52
0.5	1.171	24.54	0.770	22.13
1.5	1.183	24.69	0.775	22.62
3	1.172	24.23	0.769	21.82

Table 4.2. *Performance data for PSCs with different concentration of SnO_2 for the second layer of SnO_2. Herein, the concentration of SnO_2 for the first SnO_2 layer is 2.5% and the concentration of $MDACl_2$ in the second layer of SnO_2 is 1.5 mg/ml.*

Concentration (%)	V_{oc} (V)	J_{sc} (mA cm^{-2})	FF	PCE (%)
3.17	1.151	24.68	0.788	22.40
2	1.156	24.85	0.795	22.84
1	1.163	25.11	0.804	23.47
0	1.161	24.90	0.796	23.02

Subsequently, all samples were transferred to a glove box for the fabrication of perovskite films. PbI_2 (1.3 M) and CsI (0.13 M) were dissolved in mixed solvent (DMF: DMSO, volume ratio = 0.925: 0.075) and stirred heavily at room temperature for 50 min. The precursor solution was spin-coated at 1550 rpm for 30 s, and then annealed at 70 °C for 10 min. The mixed solution for second step was prepared with FAI:MABr:MACl (60 mg: 6 mg: 6 mg in 1 ml isopropanol), which was spin-coated at 1550 rpm for 30 s. After that, all sample were transferred to ambient air (without controlling relative humidity) for annealing at 150 °C for 15 min. Subsequently, 50 mg of spiro-OMeTAD was dissolved in 547 µl of chlorobenzene, in which 19.5 µl tBP, 5 µl of Co(III) TFSI solution (0.25 M in acetonitrile) and 11.5 µl Li-TFSI solution (1.8 M in acetonitrile) were added. The mixed solution was spin-coated at 4000 rpm for 30 s on the perovskite film. Au electrode (100 nm) was prepared via thermal evaporation with a mask under 8×10^{-6} mbar, resulting in an active area of 0.165 cm^2. A shadow mask was utilized to define the effective working area (0.09 cm^2) of the PSCs.

For low bandgap perovskite and highly efficient PSCs, Glass/FTO (FTO: fluorine-doped tin oxide) was used. The bandgap of perovskite (1.53 eV) can be obtained by EQE spectrum. PbI_2 (1.5 M) and RbCl (0.075 M) were dissolved in mixed solvent (DMF: DMSO, volume ratio = 0.925: 0.075) and stirred heavily at room temperature for 50 min. The precursor solution was spin-coated at 1500 rpm for 30 s, and then annealed at 70 °C for 1 min. The mixed solution for second step was prepared with FAI:MABr:MACl (90 mg: 4 mg: 10 mg in 1 ml isopropanol), which was spin-coated at 1800 rpm for 30 s. After that, all samples were transferred to ambient air (without controlling relative humidity) for annealing at 150 °C for 15 min. After cooling the samples to room temperature, PEAI (4 mg/ml in isopropanol) was spin-coated onto perovskite at 5000 rpm for 25 s.

For the fabrication of samples with the structure of Glass/ITO/SnO_2/Perovskite/$PC_{61}BM$/Au, the $PC_{61}BM$ solution (20 mg/ml in chlorobenzene) was spin-coated onto perovskite films at a speed of 3000 rpm for 30 s.

For the measurement of thermal stability of PSCs, PTAA was used to replace spiro-OMeTAD as the HTL. 10 mg of PTAA was dissolved in 1 ml of chlorobenzene, in which 4 µl tBP and 7.5 µl Li-TFSI solution (0.6 M in acetonitrile) were added. The mixed solution was spin-coated at 3500 rpm for 30 s on the perovskite film.

4.2.3 Characterization

Atomic force microscopy (AFM) and conductive atomic-force microscopy (c-AFM) images were obtained by Cypher ES scanning probe microscope equipped with Pt-coated Si tips. For current mapping measurements, a small DC bias of 1 V was applied to the bottom ITO electrode. Absorbance of perovskite layers and SnO_2, and transmittance of the substrate were measured by Lambda 1050 UV/Vis/NIR spectrophotometer (Perkin Elmer) in integrating sphere mode. To measure the absorption spectra of SnO_2, SnO_2 colloidal dispersion was dried into a colloidal substance at 80 ºC, which is then transferred to a quartz substrate and then annealed further. Transmission spectra and reflection spectra of the samples were measured, and then absorption spectra were obtained accordingly. Crystallographic properties of perovskite films and SnO_2 were characterized via X-ray diffraction (D2 Phaser X-Ray Diffractometer). To obtain the XRD patterns of SnO_2, the SnO_2 colloidal precursor was dried to powder at 80 ºC, and then the powder was transferred to a zero diffraction plate (Si, P-type, from MTI Corporation) for testing. Surface morphology of perovskite films and cross-section images of PSCs were characterized by the scanning electron microscope (FEI Verios SEM system). Element distribution and XPS spectra of Glass/ITO/SnO_2 were measured by ESCALAB250Xi (Thermo Scientific, UK) with mono-chromated Al K alpha (energy 1486.68 eV) under the pressure of less than 2×10^{-9} mbar. Ar ion beam (1 keV) was used to etch the samples to obtain depth profile. Etching area was 2.5 mm × 2.5 mm and reference etching rate was 0.18 nm/s. Ultraviolet photoelectron spectroscopy (UPS) spectra were measured by ESCALAB250Xi (Thermo Scientific, UK) with ultraviolet light (He I, 21.22 eV) under the pressure of less than 2×10^{-9} mbar. A bias voltage of -5 V was applied to the sample during UPS measurement. Ar ion beam (1 keV) was used to etch the samples to obtain depth profile. Etching area was 5 mm × 5 mm and reference etching rate was 0.04 nm/s.

Time-of-flight secondary ion mass spectrometry (ToF-SIMS) results were measured by using a dual beam depth profiling with Cs^+ ions for the erosion (1 keV, 72.9 nA) and primary beam Bi^{3+} for the analysis (30 keV, 0.962 pA). Detection area was 100 um × 100 um and the polarity was negative. For photoluminescence (PL) images, the PSCs were measured by a home-made PL imaging system under one sun illumination (~100 mW cm^{-2}) and open-circuit conditions. A Peltier-cooled (-70 °C) Si CCD camera (Princeton Instruments Pixis 1024) with a long-pass filter (750 nm) took the PL image from PSCs with the exposure time of 10 ms. A short period of light soaking (~30 s) was adopted before the measurements. The EQE spectra were measured by an Enlitech (QE-R) EQE measurement system. Nyquist plots were measured by EIS (CHI606D, Chenhua, Shanghai); the measurement was carried out under dark conditions without bias voltage and the frequency range was from 0.1 to 1 × 10^6 Hz; raw data was fitted and analysed by ZSimpWin. *J–V* curves of the PSCs were measured in the range of +1.2 to -0.05 V with a scanning rate of 0.15 V s^{-1} and a voltage step of 10 mV by a potentiostat source (AutolabPGSTAT302N) and solar simulator (#WAVELABS SINUS-220). The light intensity of 100 mW cm^{-2} was calibrated by a FraunhoferCalLab reference cell before measurements. There was no extra treatment for PSCs before testing, except for a short period of light soaking (~20 s). PSCs were kept at ~25 ºC and under nitrogen flow during the measurement of *J–V* curves. For the measurement of steady efficiency, the PSCs under open-circuit conditions were exposed to one sun illumination. After the V_{oc} was saturated, a bias voltage close to maximum power-point voltage was loaded and the current was monitored accordingly. The dry box used for storing PSCs often has a relative humidity of about 3%, but it was opened frequently, during which the relative humidity can rise to over 30%. Thus, its humidity was assumed to be about ~5%. The operational stability of PSCs without encapsulation was measured under LED light (100 mW cm^{-2}) with the protection of nitrogen flow and controlled temperature of ~25 ºC, during which the bias voltage (0.95 V) close to the initial maximum power point was set and the current density was traced.

4.2.4 Statistical analysis

Statistical analyses were performed by Origin 2021. V_{oc} and FF were rounded to three significant digits after the decimal point; J_{sc} and PCE were rounded to two significant digits after the decimal point. For photovoltaic parameters of control and target PSCs, 19 individual devices of each type were plotted. Data presentation was

presented as the mean ± standard deviation. Sample size (n) was shown in the corresponding table. The data derived from AFM, c-AFM, UV–vis, XPS, UPS, ToF-SIMS, SEM, PL, PL images, J–V, EQE, and steady-state efficiency were the original data without normalization. Linear fittings were applied to V_{oc} and J_{sc} versus light intensity plots and the space charge limited current (SCLC). Control and target PSCs were randomly picked for comparison of device stability. The reproducibility was checked by different perovskite compositions and different additive materials.

4.3 Results and discussion

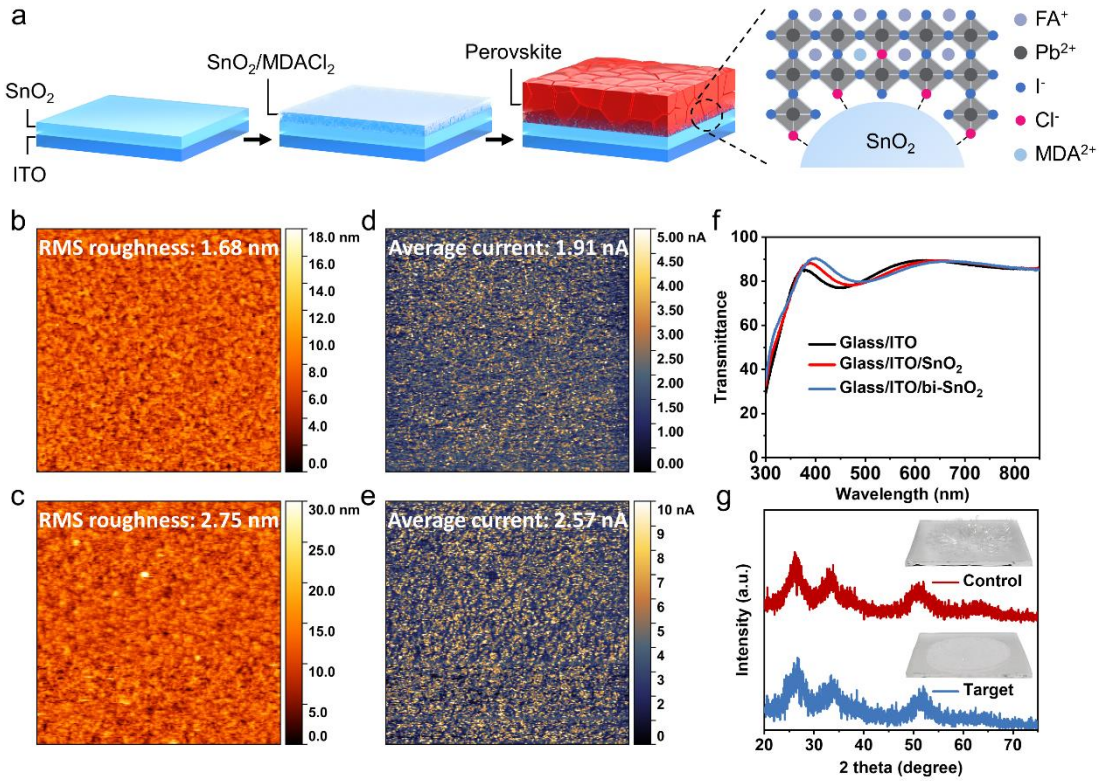

Figure 4.2. *(a) Schematic of the fabrication process of target PSCs, and the schematic of structural and chemical crosslinking SnO_2/perovskite interface; AFM images (5 μm × 5 μm) of (b) control and (c) target SnO_2 films on Glass/ITO; c-AFM images (5 μm × 5 μm) of (d) control and (e) target SnO_2 films on Glass/ITO; (f) transmittance spectra of different substrates; (g) XRD patterns of control and target SnO_2 on silicon (The inset shows the photographs of SnO_2 dried on quartz at 80 °C).*

Figure 4.2a shows the schematic of the fabrication process we proposed. Specifically, another SnO_2 layer mixed with $MDACl_2$ was spin-coated on Glass/ITO/SnO_2. Samples with SnO_2/$MDACl_2$ are denoted as the target, while control

samples adopt single-layer of SnO_2. As shown in Figure 4.2b,c, the surface morphology of the SnO_2 layer has negligible change after the incorporation of $MDACl_2$, although the roughness has increased from 1.68 nm to 2.75 nm. Given the perovskite film thickness of over 500 nm, the slightly increased roughness of SnO_2 films should not deteriorate the quality of perovskite films. Conductive atomic-force microscopy images were measured as well, with the structure of Glass/ITO/SnO_2. As shown in Figure 4.2d,e, the incorporation of $MDACl_2$ increased the average current from 1.91 nA to 2.57 nA, which should be conducive to the carrier transport in PSCs. Previous reports confirm that halogen ions, such as F^-, Cl^- and I^-, can interact with Sn^{4+} of tin dioxide,[138,139,156,164] and may introduce additional free charge carriers and then improve the conductivity of SnO_2.

In addition, the influence of $MDACl_2$ on the transmittance of the substrate is investigated. Figure 4.2f shows that the sample with SnO_2 has higher transmittance than Glass/ITO, which is consistent with previous reports.[39] Importantly, the target sample has a higher transmittance than control one, which should be attributed to the thicker SnO_2 layer.[39] Figure 4.2g shows the XRD patterns of SnO_2. Diffraction peaks at 26.4°, 33.7° and 51.3° have not been changed significantly. This is because the SnO_2 nanoparticles have been synthesized before the spin-coating, so $MDACl_2$ will not affect the crystallization process of SnO_2 nanoparticles. However, when SnO_2 colloidal dispersion was dried on quartz at 80 °C, the incorporation of $MDACl_2$ can affect its aggregation and growth behaviour (the inset in Figure 4.2g). It indicates that there is interaction between them. All in all, the double-layer structure with $MDACl_2$ improves the conductivity and transmittance of the substrate, and does not significantly affect the morphology and crystallinity of the SnO_2 layer.

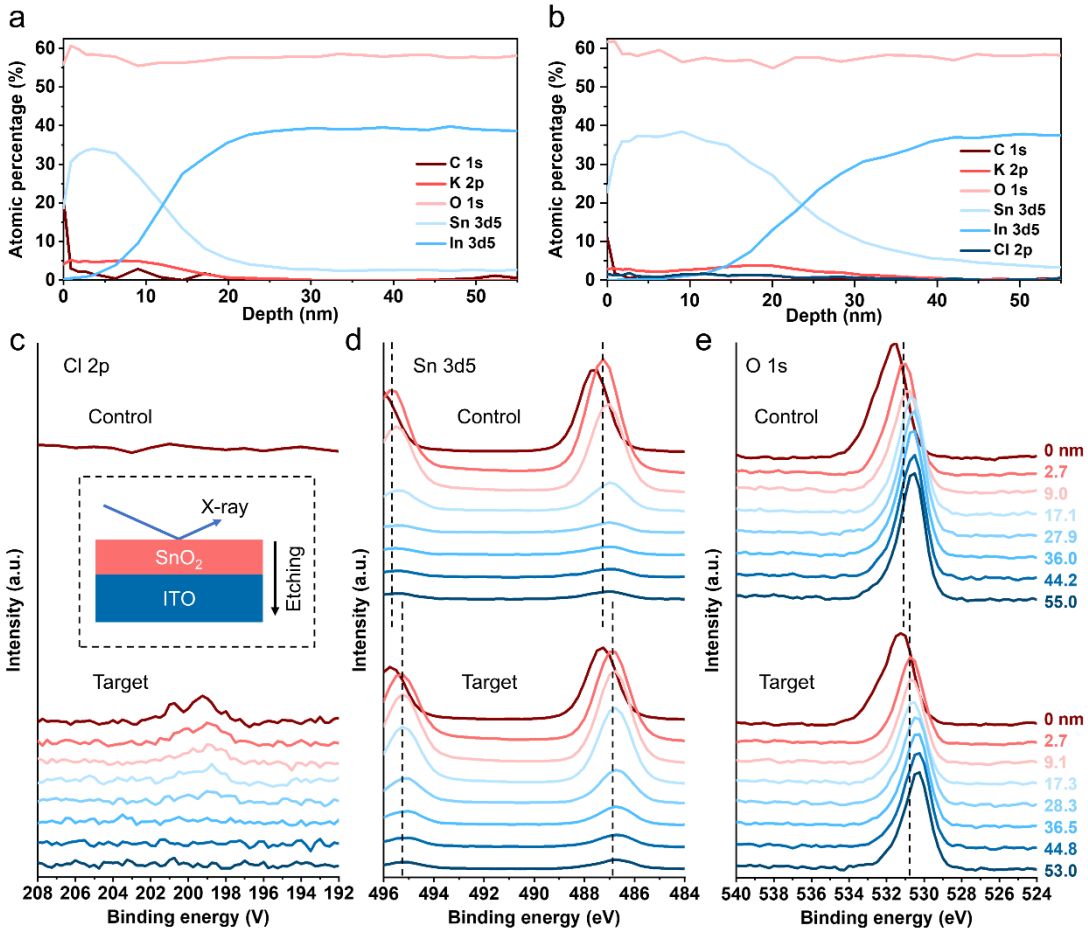

Figure 4.3. *Depth dependence of element distribution of (a) control and (b) target Glass/ITO/SnO_2 samples; depth-dependent XPS spectra of (c) Cl 2p, (d) Sn 3d5 and (e) O 1s in control and target Glass/ITO/SnO_2 samples.*

Depth-dependent XPS spectra were measured to detect element distribution in the samples (Glass/ITO/SnO_2). As shown in Figure 4.3a, the SnO_2 (corresponding to the etching depth within 13.5 nm) in the control sample is mainly composed of Sn and O elements. Nonetheless, the signal of C and K elements has been detected. The carbon on the surface should come from carbon dioxide from air and residual substances from the fabrication process of SnO_2, while the K element comes from the KOH added into SnO_2 colloidal dispersion, which is used to stabilize SnO_2 nanoparticles.[165] Similarly, the elements including Sn, O, K, and C have been detected in the target sample (Figure 4.3b). The target sample, however, has a thicker SnO_2, and chloride ions are also detected. Although $MDACl_2$ is only added to the second layer of SnO_2, chloride ions are detected in the entire double-layer SnO_2 film. This may be attributed to the migration of chloride ions within the layer, especially when the SnO_2 film is composed of tiny nanoparticles (3-4 nm).[152] Chloride ions can migrate through the grain

boundaries of SnO_2, even though it should be difficult for chloride ions to diffuse within the crystal lattice of SnO_2 as the radius of chloride ions is larger than that of oxygen ions.

Figure 4.3c-e shows the XPS spectra of Cl 2p, Sn 3d5, and O 1s at different depths in control and target samples. There is no signal of Cl in the control sample, while an obvious signal of Cl 2p can be observed in the target sample (Figure 4.3c). When the etching depth reaches 36.5 nm, the chloride signal is obviously weakened, which approximately corresponds to the ITO/SnO_2 interface. When it comes to the XPS spectra of Sn and O elements (Figure 4.3d,e), the peak location on the surface layer is obviously different from that after etching for a period of time. It is because the surface is contaminated by CO_2, O_2, H_2O, etc. from air. Thus, the signal change after 15 s of etching (corresponding to etching depth of 2.7 nm) is mainly analysed to avoid spurious signals. Sn 3d5 has a lower binding energy in the target sample, compared with the control sample (Figure 4.3d). Oxygen signal also shows a similar phenomenon, but the shift is much smaller (Figure 4.3e). Previous reports confirm that halogen ions, including F^-, Cl^- and I^-, can bond with tin ions due to their strong electronegativity. [138,139,156,164] Given the results above, it is reasonable to speculate that the Cl^- ion in $MDACl_2$ interacts with the Sn^{4+} in tin dioxide, resulting in the obvious shift of the peak position of Sn elements. Besides, it can be found that Sn and O peaks have shifted slightly during the etching process. This is because the elements around Sn^{4+} and O^{2-} are different in the SnO_2 layer and ITO, which affects the electronic density of states of these two elements.

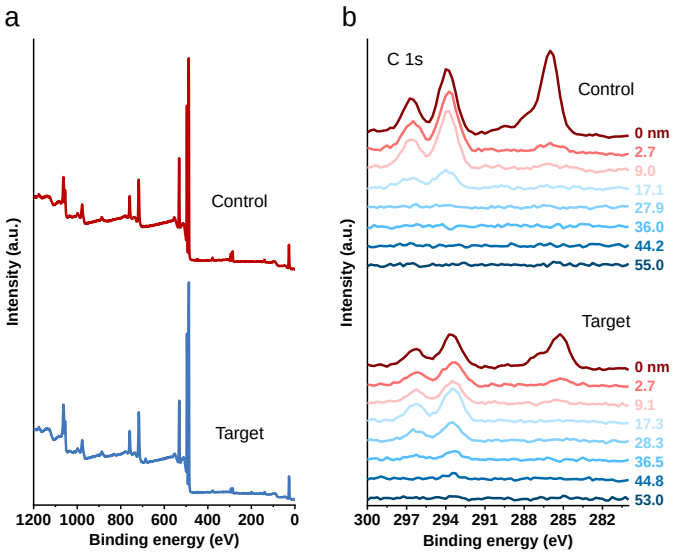

Figure 4.4. *(a) XPS spectra of the surface of control and target Glass/ITO/SnO_2 samples; (b) depth-dependent XPS spectra of C 1s in control and target Glass/ITO/SnO_2 samples.*

It should also be noted that a clear C 1s signal was detected in both types of samples (Figure 4.4). The C 1s signal crossed the entire control SnO_2 film and was even stronger than that of target sample. We speculate that there are residual substances from the fabrication process of SnO_2 colloidal dispersion. Also, the KOH stabilizer can react with carbon dioxide in the air and introduce more carbon elements into the SnO_2 film, thereby affecting the intensity of C 1s signal in XPS spectra. Apart from that, no obvious signal of nitrogen (a characteristic element of $MDACl_2$) was observed in both the control and target XPS spectra. Considering that $MDACl_2$ generally tends to be acidic when dissolved in water and SnO_2 colloidal dispersion exhibits alkalinity,[165] it is speculated that the introduced $MDACl_2$ will react in the SnO_2 dispersion or during the annealing process. Therefore, most of the nitrogen probably left the SnO_2 film in the form of ammonia.

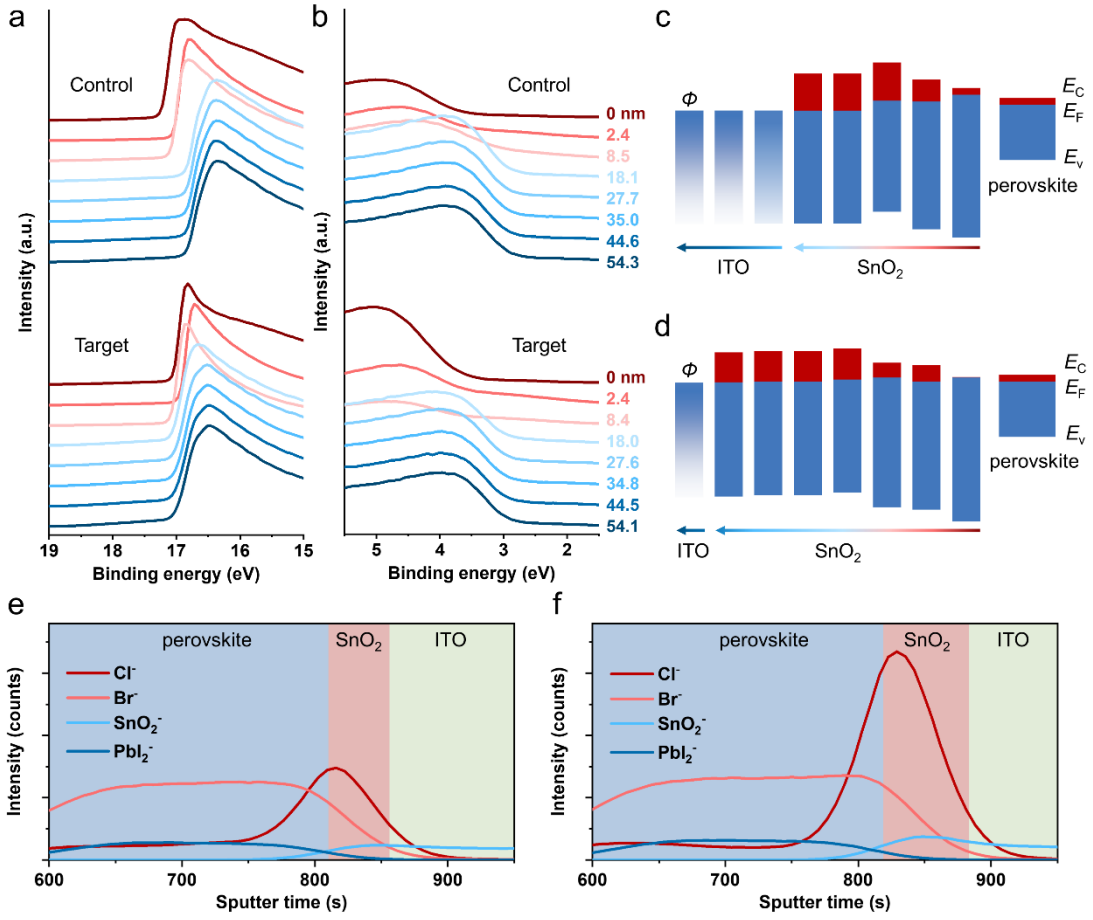

Figure 4.5. *Depth-dependent UPS spectra of control and target Glass/ITO/SnO_2 samples, showing (a) secondary electron cut-off and (b) valance band regions; energy level alignment of (c) control and (d) target samples; ToF-SIMS results of (e) control and (f) target PSCs.*

Figure 4.5a,b show depth-dependent UPS spectra of Glass/ITO/SnO_2 samples with

and without SnO_2/$MDACl_2$ (see more details in Table 4.3). Figure 4.5c,d show the details of energy level alignment of control and target samples, respectively. The Fermi level of SnO_2 is higher than the work function of ITO as the cut-off in UPS spectra shifts to lower binding energy with the etching depth. Fermi levels at different depths in the target sample are almost identical, and they are deeper than those of control sample (Table 4.3). The target sample has deeper conduction bands compared to the control sample, at the same etching depth. This leads to better energy level alignment between SnO_2 and perovskite, and facilitates charge carrier extraction. It should be ascribed to the interaction between Sn ions and chloride ions, and the result is consistent with previous reports.[157,166]

Table 4.3. *Data from UPS results of control and target samples.*

Depth (nm)	Cut-off	E_F-E_V	E_F	VBM	CB
Contol-0	17.12	3.59	4.10	7.69	3.93
2.4	16.95	3.21	4.27	7.48	3.72
8.5	16.97	2.80	4.25	7.04	3.29
18.1	16.72	2.83	4.50	7.33	3.57
27.7	16.72	2.83	4.50	7.33	3.57
35.0	16.72	--	4.50	--	--
44.6	16.72	--	4.50	--	--
54.3	16.72	--	4.50	--	--
Target-0	16.97	3.62	4.25	7.87	4.24
2.4	16.87	3.22	4.35	7.57	3.94
8.4	16.97	3.26	4.25	7.51	3.88
18.0	16.92	2.84	4.30	7.14	3.52
27.6	16.87	2.86	4.35	7.21	3.59
34.8	16.87	2.86	4.35	7.21	3.59
44.5	16.85	2.87	4.37	7.24	3.62
54.1	16.84	--	4.38	--	--

Given the XPS results, there is limited information that can be gained from analysis of the surface of the SnO_2 due to the contamination from air. However, what

can be determined is that due to the introduction of $MDACl_2$, SnO_2 becomes more n-type, and its Fermi level and conduction band move downward (Figure 4.5c,d and Table 4.3). Intriguingly, it is found that the conduction band in the SnO_2 layers of both the control and target samples gradually shifts upwards as the etching depth increases. This is unfavourable for electron transport within the SnO_2 films. Considering the thin SnO_2 layer and its high mobility up to 240 cm^2 $(V\ s)^{-1}$,[167] it should not significantly hinder electron transport.

ToF-SIMS was utilized to investigate the distribution of different elements in final PSCs. The signal of Cl^- ions is relatively low in the perovskite bulk (Figure 4.5e), which should be derived from methylammonium chloride in perovskite precursor solution. On the contrary, it is significantly enhanced at the SnO_2/perovskite interface. This should be attributed to that Sn^{4+} in tin dioxide attract Cl^- ions due to strong Cl-Sn bonds, so that Cl^- ions are anchored at the SnO_2/perovskite interface and in SnO_2 films after the preparation of perovskite films. Compared with the control sample, the target one shows a much stronger signal of Cl^- ions (Figure 4.5f), which should be ascribed to the introduction of $MDACl_2$. A weak increase in SnO_2^- peak is also detected, corresponding to the etching time of ~850 s, which is attributed to the increased thickness of SnO_2 films. Importantly, the signals of Cl^- and SnO_2^- do not reach the peak at the same etching time in both samples. Compared with SnO_2^-, Cl^- reached the highest point with shorter sputtering time in both samples. It suggests that Cl^- ions prefer to stay at SnO_2/perovskite interface in PSCs. All in all, the results above indicate that the incorporation of $MDACl_2$ induces more chloride ions to accumulate at the SnO_2/perovskite interface and in SnO_2 layers. Strong Sn-I ionic bond has been confirmed at the SnO_2 surface previously,[164] and chloride ions have stronger electronegativity as compared to iodine ions. Accordingly, the charge transfer at the SnO_2/perovskite interface and orbital coupling between Sn ion and halide ions may be enhanced, and it may affect charge carrier extraction and transport.

The effect of $MDACl_2$ incorporation on the perovskite film is also investigated. Figure 4.6a,b suggest that the grain size of perovskite is significantly increased as $MDACl_2$ is used as an additive into SnO_2 colloidal dispersion. Average grain size of perovskite increases from 667 to 849 nm (Figure 4.6c). Besides, the white phase on the surface of perovskite is obviously reduced, which is generally regarded as lead iodide decomposed from the perovskite during annealing.[82] These results suggest that inserted SnO_2/$MDACl_2$ layer can improve the quality of perovskite films. This is

because $MDACl_2$ can be dissolved in perovskite precursor solution,[94,168] so MDA^{2+} and Cl^- ions can participate in the crystallization and growth of perovskite. SEM cross-section images of PSCs show that target perovskite grains almost cross the whole perovskite film and the grain boundary becomes indistinguishable after introducing $SnO_2/MDACl_2$ layer (Figure 4.6d).

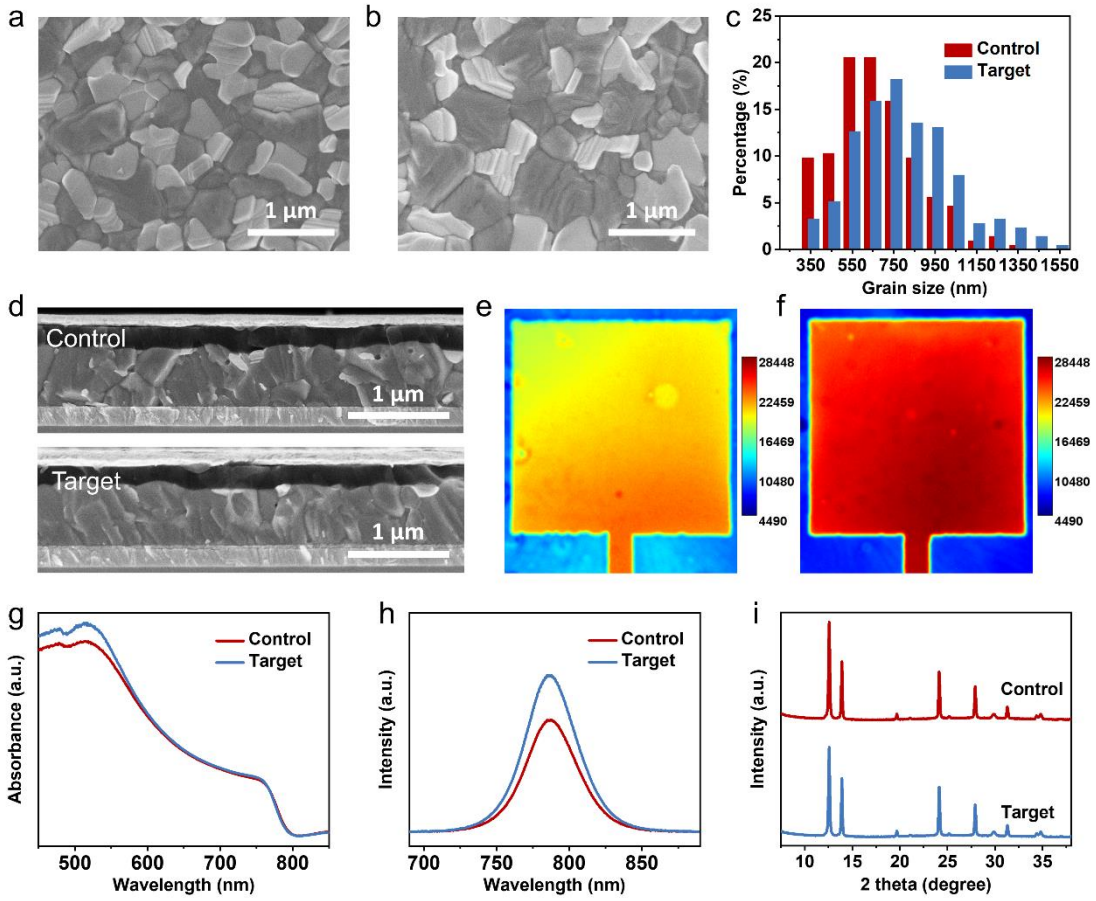

Figure 4.6. *SEM images of perovskite films deposited on (a) control and (b) target SnO_2 films; (c) grain size distribution of perovskite films based on control and target substrate; (d) SEM cross-section images of control and target PSCs; PL images of (e) control and (f) target PSCs; (g) absorbance spectra, (h) steady PL spectra and (i) XRD patterns of control and target perovskite films.*

Photoluminescence images of the PSCs were measured, and the results show that the target cell had a stronger PL intensity (Figure 4.6e,f). This should be ascribed to enlarged perovskite grains and improved film quality, which suppress trap-assisted nonradiative recombination. Figure 4.6g shows that the absorbance of perovskite is slightly enhanced with the incorporation of $SnO_2/MDACl_2$. This should be due to the reduction of white phase in perovskite films. Meanwhile, the steady PL intensity of the perovskite film is improved by $SnO_2/MDACl_2$ (Figure 4.6h), which is consistent with

the results of PL images. XRD patterns suggest that the diffraction peak intensity of perovskite shows negligible change, while the diffraction peak affiliated to PbI_2 at 12.6° was weakened slightly (Figure 4.6i). More specifically, the ratio of diffraction peak intensity between PbI_2 and perovskite decreased from 1.65 to 1.51 after introducing SnO_2/$MDACl_2$. This corresponds to the reduction of white phase in Figure 4.6a,b. It is noted that the diffraction peak affiliated to PbI_2 should be ascribed to the decomposition of perovskite during annealing,[82] and the perovskite film with larger crystal grains generally has better thermal stability. In conclusion, the SnO_2/$MDACl_2$ layer significantly improved the quality of perovskite films, which helps to suppress nonradiative recombination and improve the device performance.

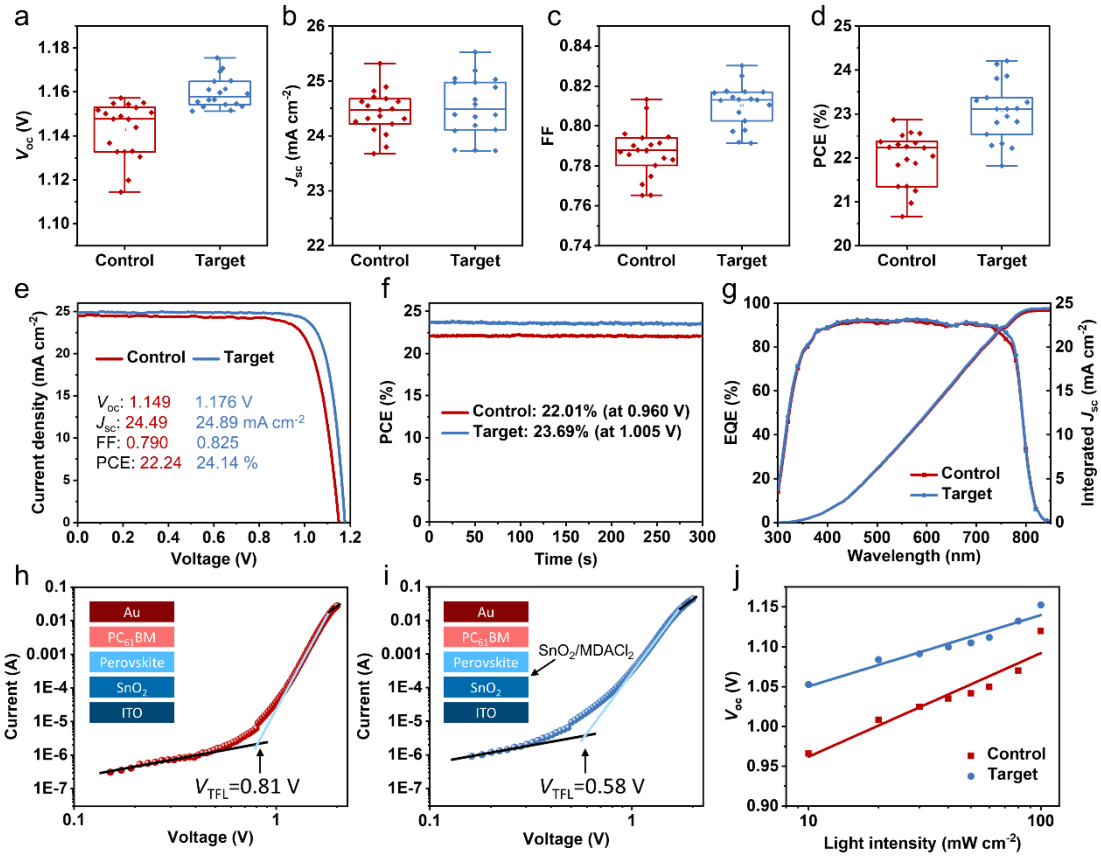

Figure 4.7. *(a) V_{oc}, (b) J_{sc}, (c) FF, and (d) PCE statistics of control and target PSCs; (e) J–V curves, (f) steady-state efficiency, and (g) EQE spectra of control and target PSCs; dark current–voltage curves of the electron-only devices (h) without and (i) with SnO_2/$MDACl_2$ layer; (j) light-dependent of V_{oc} derived from control and target PSCs.*

Based on the structure of Glass/ITO/SnO_2/Perovskite/Spiro-OMeTAD/Au, PSCs with and without SnO_2/$MDACl_2$ layers were fabricated, and statistical results of device performance are shown in Figure 4.7a-d. It is apparent that target PSCs show higher V_{oc}

and FF, leading to increased efficiencies. This should result from the enhanced quality of perovskite films and improved charge carrier transport. Suppression of carrier recombination in perovskite bulk and at the SnO_2/perovskite interface should contribute to it as well. In contrast to V_{oc} and FF, J_{sc} shows negligible difference between control and target cells. As a result, champion PSC is obtained with $MDACl_2$, which yields the efficiency (V_{oc}, J_{sc} and FF) of 24.14% (1.176 V, 24.89 mA cm^{-2} and 0.825), as shown in Figure 4.7e. A steady-state efficiency of 23.69% was achieved under AM 1.5G illumination at the bias voltage of 1.005 V, showing much better performance than control cells (Figure 4.7f). High quantum conversion efficiencies in visible light range were achieved in control and target cells (Figure 4.7g), resulting in integrated J_{sc} of 24.16 and 24.39 mA cm^{-2}, respectively. They are in good agreement with the values obtained from *J–V* curves, showing the J_{sc} discrepancy of less than 3%.

Space charge limited current is used to evaluate the trap-state density of perovskite, with an architecture of ITO/SnO_2/Perovskite/$PC_{61}BM$/Au. As shown in Figure 4.7h,i, the trap-filled limit voltage (V_{TFL}) decreases from 0.81 V to 0.58 V. Accordingly, the trap-state density (N_t) can be obtained via Equation (4-1)

$$N_t = \frac{2\varepsilon_0 \varepsilon V_{TFL}}{eL^2} \quad (4\text{-}1)$$

where ε_0 is the vacuum permittivity, and ε is the relative dielectric constant of $FAPbI_3$ (ε = 46.9),[169] e is the electron charge, and L is the thickness of the perovskite film (~700 nm, Figure 4.6d). Accordingly, the N_t is calculated, and it decreases from 8.58 × 10^{15} cm^{-3} to 6.14 × 10^{15} cm^{-3} after the introduction of SnO_2/$MDACl_2$. This should be attributed to the increased perovskite grain size, reduced grain boundaries and white phase. V_{oc} under different illumination intensity also shows that SnO_2/$MDACl_2$ significantly increases the V_{oc} of the device (Figure 4.7j). Compared with the control sample, the target sample has a smaller deviation between the slope and the value of (kT/q), as shown in Figure 4.7j. Generally, it suggests that trap-assisted carrier recombination has been suppressed.

To explore the carrier dynamics within the cells, the electrical impedance spectroscopy was employed. The results suggest that the R_s increased slightly from 1.36 to 1.86 Ω cm^2 (Figure 4.8). It should be ascribed to the increased thickness of SnO_2 in target PSCs, as compared to control cells. However, the R_{tr} decreased from 951.0 to 409.9 Ω cm^2, while R_{rec} increased from 4.75 × 10^5 to 5.41 × 10^5 Ω cm^2. It suggests that the incorporation of $MDACl_2$ facilitates charge carrier transport and suppresses carrier recombination, which is consistent with the results of *J-V* curves (Figure 4.7a-e). These

results should be attributed to the improved quality of perovskite films and better energy level alignment between SnO_2 and perovskite (Figure 4.6a-d and Figure 4.5a-d).

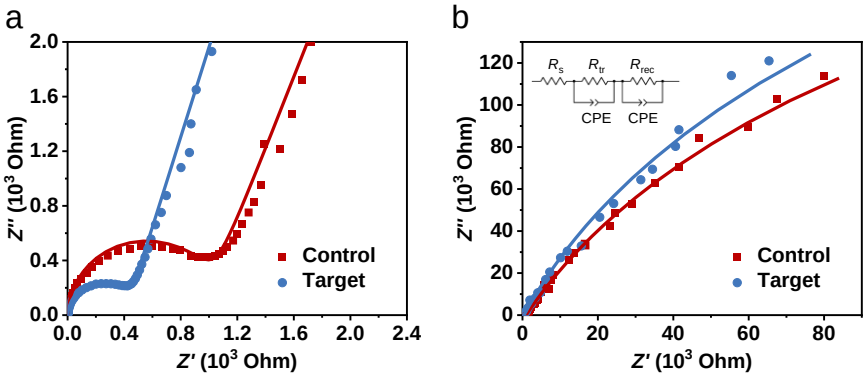

Figure 4.8. *(a) High-frequency and (b) low-frequency region Nyquist plots of control and target PSCs. Points represent raw data and curves are fitting curves. Inset in (b) is the equivalent circuit used to fit the data.*

It is assumed that the increase in device performance is induced by the improvement of Cl-treated SnO_2 and more favourable perovskite, rather than sole one origin. According to the aforementioned results, the insert layer containing SnO_2 nanoparticles and chloride salts improves the conductivity of SnO_2 and leads to a better energy level alignment between SnO_2 and perovskite. Besides, Figure 4.6a,b suggest that perovskite grain size is increased and the white phase is reduced on the surface of perovskite films via our strategy. Figure 4.7h,i further suggest that the proposed strategy reduces the trap-state density of perovskite, which is beneficial to suppress charge carrier recombination in the bulk. Therefore, the change in device performance should result from a combination of the two effects.

To investigate whether the proposed methodology is universal, other materials have been used to replace $MDACl_2$. As shown in Table 4.4, the improvement in efficiency still can be observed when MACl, caesium chloride (CsCl), or 4-methylphenethylammonium chloride (4M-PEACl) were used. These results confirm that the structural and chemical crosslinking interface we proposed here is effective and universal for improving device performance, as long as the transport of charge carriers is not greatly affected. The reproducibility of the strategy was checked by different additive materials, various characterization aforementioned, and different perovskite composition (see it later), demonstrating the promising reproducibility of the strategy we proposed.

Table 4.4. *Performance data for PSCs with the incorporation of different materials into second SnO_2 layer. Each result is derived from at least 5 cells.*

Condition	V_{oc} (V)	J_{sc} (mA cm^{-2})	FF	PCE (%)
Control	1.143 ± 0.013	24.42 ± 0.40	0.788 ± 0.012	22.01 ± 0.60
$MDACl_2$	1.160 ± 0.007	24.53 ± 0.54	0.810 ± 0.011	23.06 ± 0.67
MACl	1.149 ± 0.005	25.00 ± 0.51	0.800 ± 0.014	22.98 ± 0.63
CsCl	1.147 ± 0.011	24.33 ± 0.16	0.802 ± 0.002	22.38 ± 0.28
4M-PEACl	1.154 ± 0.007	24.87 ± 0.88	0.798 ± 0.007	22.89 ± 1.04

The long-term stability of the PSCs is shown in Figure 4.9a. Target cells showed the average efficiency of 22.88% after storage of 11208 h in dry air (relative humidity of ~5% and ~25 °C), corresponding to 98% of the highest value. More importantly, target PSCs show much better stability, especially after the storage of about 4500 h. This should be attributed to the structural crosslinking between perovskite and SnO_2, and the chemical crosslinking between Cl^- and Sn^{4+}, which reduces interfacial defects and stabilizes the SnO_2/perovskite interface.[140,157,166] As shown in Figure 4.9b, target PSCs exhibited slightly improved thermal stability, as compared to control cells. Nonetheless, it is necessary to point out that both they exhibited poor thermal stability, reducing to 80% of the initial efficiency within 300 h. MA^+ cation with relatively volatile nature may gradually leave the perovskite lattice during heat treatment,[85,86] leading to significant structural changes and more defects. This limits thermal stability of PSCs and covers the role of SnO_2/$MDACl_2$ in improving thermal stability of PSCs. As shown in Figure 4.9c, the target cell presented promising operational stability, retaining 85.50% of the initial PCE after 1000 h of illumination of white light-emitting diode (LED) light (100 mA cm^{-2}). In contrast, the control cell showed much worse stability under illumination. We speculate that the improved stability is attributed to the reduced interfacial defects and stronger interaction between chloride ions and lead ions, which reinforces the interface between perovskite and SnO_2. Besides, a reduced amount of white phase on the surface of perovskite films and a lower amount of PbI_2 should also play a vital role in improving the operational stability of PSCs under light. It is because the PbI_2 is prone to decompose into metallic lead under light and then increases nonradiative recombination in perovskite films.[76-78] All in all, these results suggest that the structural and chemical crosslinking interface not only improves device performance but also enhances their stability. However, we want to emphasize that both

PSCs presented a relatively fast decay during the initial stage of illumination, known as "burn-in" degradation.[170-172] More research should focus on this and the thermal stability of PSCs, which is of great significance for practical applications of perovskite solar modules, but it is beyond the scope here.

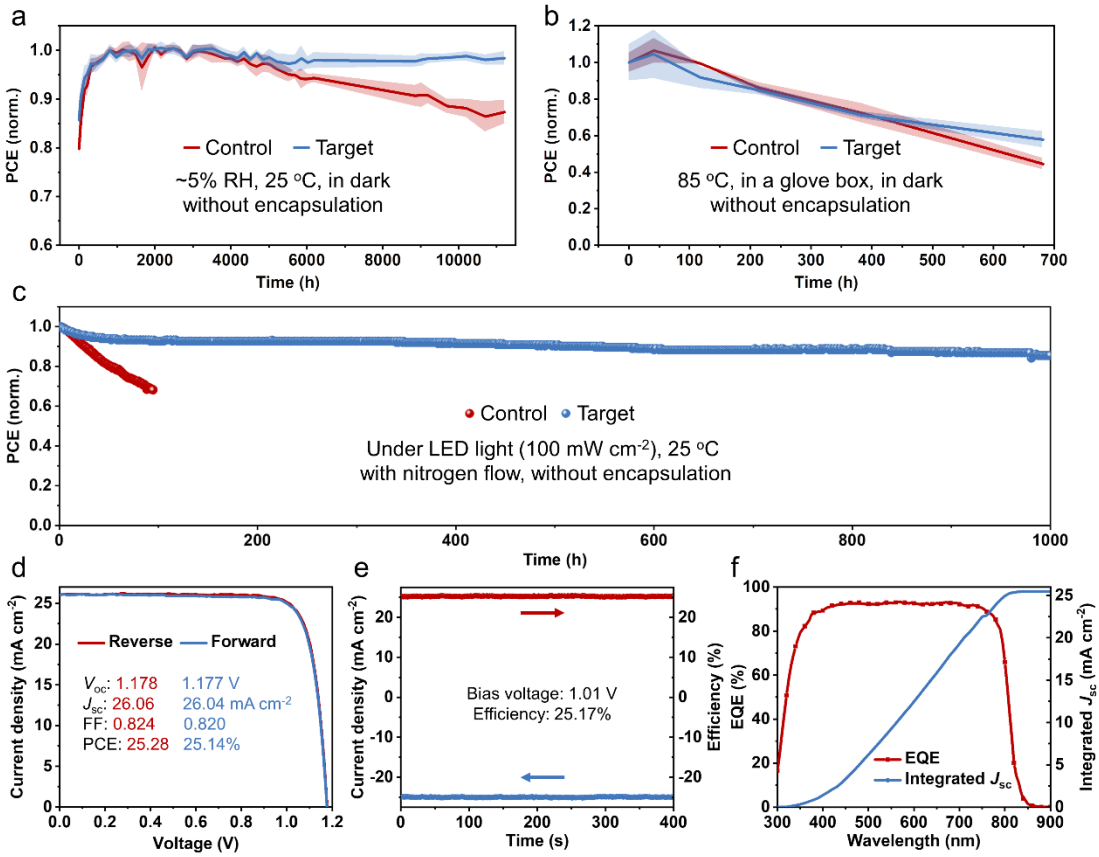

Figure 4.9. *(a) Long-term stability of the unencapsulated PSCs (5 cells for each condition) stored in dry air (relative humidity of ~5% and ~25 °C); (b) thermal stability of the unencapsulated PSCs (3 cells for each condition) kept at 85 °C in a glove box; (c) operational stability of the unencapsulated PSCs under LED light, with the protection of N_2 flow; performance of target PSCs with low bandgap perovskite, including (d) J–V curves, (e) steady-state efficiency and (f) EQE spectrum.*

Low bandgap perovskite (1.53 eV) was also used to further improve the device performance and confirm whether the strategy is still applicable to other compositions of perovskite. As shown in Figure 4.9d, the champion cell with SnO_2/$MDACl_2$ layer presented the efficiency of 25.28% (reverse scan), and showed negligible hysteresis, which is much higher than that of the control cell (Figure 4.10). Steady-state current density and efficiency were 24.92 mA cm^{-2} and 25.17% respectively, at the bias voltage of 1.01 V (Figure 4.9e). The efficiency is promising and impressive as compared to those of single junction n-i-p PSCs reported so far (Table 4.5). Integrated J_{sc} from EQE

spectrum was 25.49 mA cm^{-2} (Figure 4.9f), corresponding to 97.8% of the J_{sc} value (26.06 mA cm^{-2}) obtained from *J-V* curves (Figure 4.9d). The results above indicate that the strategy we proposed can be applied to different types of perovskites.

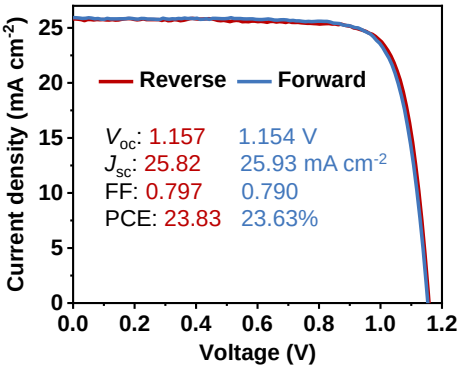

Figure 4.10. *J–V curves of the control PSC based on low bandgap perovskite (1.53 eV) under the illumination of 1 sun.*

Table 4.5. *A summary of recent progress of single junction n-i-p PSCs.*

Cell configuration	Key point	Perovskite coating method	Active area (cm^2)	PCE (%)	Reference
FTO/SnO_2/KCl/FA-perovskite/Spiro-OMeTAD/Au	Tuning the CBD SnO_2	Anti-solvent method	0.09370	25.4	[121]
FTO/SnO_2/KFAMDA-perovskite/MeO-PEAI/Spiro-OMeTAD/Au	Coherent interlayer ($FASnCl_x$)	Anti-solvent method	0.09540	25.83	[172]
FTO/c-TiO_2/m-TiO_2/$FAPbI_3$/OAI/Spiro-OMeTAD/Au	Ion-modulated radical doping	Anti-solvent method	0.06	25.15	[173]
FTO/TiO_xN_y/m-TiO_2/PMMA:PCBM/$Cs_{0.05}FA_{0.9}MA_{0.05}PbI_{2.74}Br_{0.26}$/PMMA/P3HT:CuPc/Au	Nitrogen-doped TiO_2	Vacuum flash treatment	1.0189	23.36	[143]
FTO/SnO_2/$FAPbI_3$/PEAI/Spiro-OMeTAD/Au	Inactive $(PbI_2)_2RbCl$	Two-step spin-coating	0.07414	26.1	[51]
ITO/SnO_2/BGCl/FAMA-perovskite/PEAI/Spiro-OMeTAD/MoO_3/Ag	Interfacial modification via BGCl	Two-step spin-coating	0.08	24.42	[140]
ITO/SnO_2/FAMACs-perovskite/PPEAI/Spiro-OMeTAD/Au	Rb-based perovskitoid scaffold	Anti-solvent method	0.0706	25.14	[174]
ITO/SnO_2/$FA_xMA_{1-x}PbI_3$/OACl/Spiro-OMeTAD/Au	Pre-annealing treatment	Two-step spin-coating	0.058424	24.95	[175]

FTO/c-TiO_2/SnO_2/$Cs_{0.05}MA_{0.05}FA_{0.9}PbI_3$/PEAI/Spiro-OMeTAD/Au	Pentanamidine hydrochloride (PAD) additive	Vacuum flash treatment	0.06	25.4	[176]
FTO/SnO_2/KCl/$FAPbI_3$/Spiro-OMeTAD/Au	Volatile alkylammonium chlorides	Anti-solvent method	0.09597	26.08	[43]
FTO/SnO_2/$FAPbI_3$/Phenylethanamine salt/Spiro-OMeTAD/Au	Anion–π interactions	Two-step spin-coating	0.08313	26.07	[177]
ITO/$SrSnO_3$/$Cs_{0.05}(FAMA)_{0.95}PbI_3$/OATsO/Spiro-OMeTAD/Au	$SrSnO_3$ electron transport layer	Two-step spin-coating	0.049	25.17	[178]
PI/ITO/SnO_2/FAMACs-perovskite/PPAI/Spiro-OMeTAD/Au	Interfacial modification via PF	Anti-solvent method	0.0601	24.61	[52]
ITO/SnO_2/FAMACs-perovskite/Spiro-OMeTAD/Au	All-interface defect passivation	Two-step spin-coating	0.1196	25.43	[179]
FTO/SnO_2/KCl/FAMACsRb-perovskite/PEAI/Spiro-OMeTAD/MoO_3/Ag	Dibromosuccinic acid (DBSA) additive	Anti-solvent method	0.09	25.41	[180]
FTO/c-TiO_2/SnO_2/$FAPbI_3$/OAI/Spiro-OMeTAD/Au	Intrinsic Cl-doped SnO_2	Anti-solvent method	0.085	24.98	[181]
FTO/SnO_2/$FAPbI_3$/PEAI/ Spiro-OMeTAD/MoO_3/Ag	IP-TFSI initiator	Two-step spin-coating	0.062	25.16	[182]
FTO/SnO_2/GDA/$FAPbI_3$/HABr/ Spiro-OMeTAD/MoO_3/Ag	Glycocyamine (GDA) molecular bridge	Anti-solvent method	0.08	24.70	[183]
FTO/c-TiO_2/SnO_2/$FAPbI_3$/ $H_2C_2O_4$/Spiro-OMeTAD/Au	Lead oxalate (PbC_2O_4) compact layer	Anti-solvent method	0.067	25.39	[184]
FTO/TiO_2/$FAPbI_3$/PEAI/ Spiro-OMeTAD/Au	Laser derived electron transport layers	Anti-solvent method	0.045	25.05	[185]
FTO/SnO_2/$FAPbI_3$/PFACl/Spiro-OMeTAD/Au	PFACl post-treatment	Two-step spin-coating	0.148	24.9	[186]
FTO/c-TiO_2/SnO_2/ $FA_{0.92}Cs_{0.08}PbI_3$/EDTMP/ Spiro-OMeTAD/Au	Subsurface lattice reconstruction via EDTMP	Anti-solvent method	0.1	25.20	[187]
FTO/SnO_2/ $FAPbI_3$/OAI/Spiro-OMeTAD/Au	Trimethylsulfoxonium iodide (TMSOI) additive	Two-step spin-coating	0.125	24.65	[188]
FTO/SnO_2/RbFAMA-perovskite/PEAI/Spiro-OMeTAD/Au	Structural and chemical crosslinking Interface	Two-step spin-coating	0.09	25.28	This work

4.4 Conclusion

In summary, structural and chemical crosslinking SnO_2/perovskite interface was constructed by utilizing a double layer of SnO_2 and incorporating $MDACl_2$, which can be dissolved by perovskite precursor solution. The chloride ions derived from $MDACl_2$ can penetrate the entire SnO_2 film, thereby improving its conductivity. The incorporation of $MDACl_2$ leads to more n-type SnO_2 and better energy level alignment between SnO_2 and perovskite, which facilitates electron extraction from perovskite to SnO_2. Chloride ion exhibits strong interaction with Sn^{4+}, which inhibits iodine vacancies at the interface and oxygen vacancies on the surface of SnO_2. Furthermore, the introduction of $MDACl_2$ significantly improved the quality of perovskite films and charge carrier dynamics within the cell. Consequently, the PSC with an efficiency of over 25% was obtained via this strategy. The operational stability and long-term stability of the PSCs were substantially improved. This work provides valuable guidelines for the design of multifunctional and stable interfaces between perovskite and charge transport layer.

CHAPTER 5

5 Summary and Outlook

5.1 Summary

5.1.1 Sparkling hot spots in perovskite solar cells under reverse bias

The stability of PSCs under reverse is important for their commercialization and application. The sparkling hot spots of PSCs under reverse bias have been found and revealed by in-suit infrared micro-thermography. The results indicate that there is a close relationship between the changes in local temperature and the changes in reverse current inside the reverse biased PSCs. By characterizing the morphology of each layer, it has been confirmed that sparkling hot spots are derived from abnormal bulges in perovskite films. Elemental analysis indicates that the bulge originates from PbI_2 clusters in PbI_2 layer, namely the first step of the fabrication of perovskite films. Additionally, the appearance and disappearance of hot spots were explained by band bending and tunnelling current caused by ion accumulation under reverse bias. These results provide guidance for the study of the behaviour of PSCs under reverse bias.

5.1.2 Manipulating the migration of iodine ions via reverse-biasing for boosting photovoltaic performance of perovskite solar cells

The ion migration in perovskites is generally a notorious issue, which can lead to the degradation of perovskites and hysteresis of *J-V* curves. However, it was found that the performance of PSCs can be improved by precise control of the value and loading time of reverse bias. The enhancement in V_{oc} and PCE was observed after the PSCs are subjected to reverse bias, for example, at -0.4 V for 3 min in dark. Characterization suggests that the reverse-biasing improved the charge carrier dynamics, including the increased recombination resistance, suppressed nonradiative recombination, and

enhanced built-in electric field. According to the results of XPS spectra and activation energy, we speculated that iodine ions would migrate and accumulate at the SnO_2/perovskite interface under reverse bias, so parts of the iodine vacancies at the interface would be filled. First-principles calculations suggest that larger built-in electric field and improved charge transport can be obtained when the iodine vacancies at SnO_2/perovskite interface were passivated. Also, it has been confirmed that the interaction between I^- ions and Sn^{4+} within SnO_2 layers is able to passivate oxygen vacancies on the surface of SnO_2. These results may help researchers reassess the role and impact of ion migration in perovskites, and are of great significance to investigate the physics of PSCs under electric field.

5.1.3 Universal strategy with structural and chemical crosslinking interface for efficient and stable perovskite solar cells

The planar heterojunction structure has been widely adopted in high-performance PSCs, but its drawbacks may not have been fully recognized. Herein, structural and chemical crosslinking interface was proposed and constructed, leading to the enhanced interaction and increased contact area between perovskite and SnO_2. Due to the incorporation of chloride salts that can be dissolved by perovskite precursors, more chloride ions were observed at the SnO_2/perovskite interface. Accordingly, the electrical properties of SnO_2 and perovskite films have been improved, and the strategy leads to preferable energy level alignment between SnO_2 and perovskite, thus improving the carrier dynamics within PSCs. As a result, the performance of n-i-p single-junction PSCs has been improved, especially the V_{oc} and FF. PSCs with over 10000 h of self-stability have been obtained, retaining 98% of initial efficiencies after the storage in dry air (~5% relative humidity). Besides, the operational stability of PSCs was enhanced, maintaining 85.50% of the initial efficiency after 1000 h of operation under light. By adopting the narrow-bandgap perovskite (1.53 eV), this strategy boosted the efficiency of PSCs to 25.28%. This work reveals the importance of interfaces in PSCs and provides new insights for interface engineering.

5.2 Outlook

This thesis mainly focuses on two directions including the behaviour of PSCs under reverse bias and interface engineering for efficient and stable PSCs. The research

in both directions can deepened, and the related outlook is presented below.

The initial motivation of the research about reverse bias is to improve the stability of perovskite solar panels under reverse bias caused by partial shading. There are two research routes we can choose. In the first approach, shaded cells should have the reverse current density equal to the value of current density of illuminated cells. To minimize the resistive losses and the cell degradation induced by resultant localised heating, the breakdown voltage of the PSCs should be as small as possible, and the reverse current should not cause permanent device degradation. It means that the shaded parts can recover gradually after removing the reverse bias. In the second approach, we can require the PSCs to withstand a large reverse bias voltage. It may range from -10 to -20 V, which depends on how many sub-cells are connected in series in the perovskite module. It also requires the PSCs to keep stable under such a large reverse bias, and then fewer bypass diodes can be used for the perovskite solar panels, which significantly reduces production costs and simplifies the fabrication process. However, strategies related to these two routes have not been proposed in the literature. It can be attributed to the fact that the physical mechanism of PSCs under reverse bias is still unclear. For example, device structures can affect the behaviour of PSCs under reverse bias, and the reasons for this have not been presented.[101] Therefore, it is necessary to investigate the effect of charge transport layers and their thicknesses on the behaviour of reverse biased PSCs. Given the ionic nature of perovskites, it is meaningful to use different perovskite materials including all-inorganic perovskites, single crystal perovskites, and 2D perovskites, to explore their influence on the reverse bias behaviour of PSCs. In addition, simulation of devices should be introduced, which is beneficial to analyse the potential distribution in PSCs and the electric field strength in each layer. It enables the specific optimization such as nanoscale localized contacts or porous insulator contact at the interface.[189,190] Accordingly, applying more potential to stable layers or interfaces and reducing the electric field strength in the perovskite layer can be realized, which should be beneficial to the stability of PSCs under reverse bias.

In previous reports, the PSCs were subject to reverse bias voltage in dark.[100-102,131,164] However, the situation in actual field is much more complicated. For example, the sub-cells are connected in series in perovskite modules, rather than each device working separately. In addition, the shaded area in the module is not fixed, indicating that the value of reverse bias may change as time goes by. In actual field, the shaded parts are not in a completely dark state. Given the high V_{oc} generated by the PSCs under

weak illumination,[191] it is necessary to investigate the reverse bias behaviour of PSCs under the light with low intensity. In addition, the shaded cell will heat up due to the reverse bias, as shown in Figure 2.2d. The more sub-cells connected in series in the perovskite module, the greater the reverse bias voltage and the more power dissipated in the shaded sub-cells. There is little research on the increased temperature caused by reverse bias, and its solution is absent. Apart from that, perovskite modules can be used to study their behaviour under partial shading as the efficiency of perovskite modules is over 20%.[192,193] Besides, the monolithic 2-terminal perovskite/silicon, perovskite/perovskite, and perovskite/organic tandem solar cells, are growing rapidly and show great application prospects. However, research on the behaviour and stability of these cells under reverse bias is still very limited.[194,195] Considering the complicated structure in tandem solar cells, device simulation should be introduced to simplify the experiment process and reveal the mechanism of cell degradation induced by reverse bias. The research aforementioned should be necessary for improving the stability of PSCs under reverse bias.

When it comes to interface engineering, there are many research works related to this thesis that can be carried out. Currently, the interface engineering for perovskite is mainly focusing on the passivation of surface defects, which significantly improves the device performance. However, the passivation of interface defects and enhancement in interface contact need to be balanced carefully, especially for the mechanical stability of flexible PSCs. Introducing the structural crosslinking interface with an interface passivation layer may be a feasible approach. In addition, the metal electrodes (especially the silver electrode) can be peeled off from the PSCs, indicating weak contact between the metal electrode and the underneath charge transport layer. It is detrimental to the mechanical stability of flexible PSCs and the charge carrier transport at the interface. It is necessary to adopt some methods to enhance the stability of the interface between metal electrodes and the underneath charge transport layers.

Irrespective of the rapid development of PSCs and wide application of perovskite materials in solar cells, photodetector, and light-emitting diodes, there are several key issues for perovskites to be solved. They are still limiting the application and commercialization of PSCs. Thus, an outlook focusing on these issues is presented.

(1) The degradation of perovskites and PSCs induced by external stimuli. Although PSCs with operational stability exceeding 1000 h and robust long-term stability have been reported, perovskite active layers and PSCs are still vulnerable to

external stimuli, including light, high-energy radiation, heat, strain, humidity, oxygen, and bias voltage. Among them, humidity and oxygen can be blocked by encapsulation, but other stimuli still exist as long as the perovskite module is under operation. Therefore, it is necessary to further investigate the degradation mechanism of PSCs induced by external stimuli, and accordingly provide related solutions. Ion migration within perovskite films and devices is an intrinsic issue for the operation of PSCs. Suitable methods or characterization are urgent for in-situ observation of ion migration within the device, and then more information about ion migration and phase segregation can be obtained. It should be beneficial to improve the operational stability of PSCs.

(2) Large-area printing of PSCs. The PSCs with record efficiencies are still based on small active area (~0.1 cm^2). For the large-scale application and commercialization of PSCs, it is necessary to utilize printing technology including doctor-blading, slot-die coating, and roll-to-roll microgravure printing to fabricate PSCs. Yet, the efficiency of large-area and printed PSCs is still limited. More efforts should be devoted to this direction, to optimize the facilities, printing process, and perovskite precursor solution. Since perovskite/silicon and perovskite/perovskite tandem solar cells exhibit higher efficiency and the properties of the substrate used for perovskite deposition varies significantly, it is necessary to develop the printing methodology of perovskite films for tandem solar cells.

(3) Toxicity of lead-based perovskite and the oxidation of divalent tin. High-performance PSCs generally contain lead elements. It is a potential risk for the environment, especially when PSCs are applied to building integrated photovoltaics. Therefore, it is necessary to manage lead leakage in PSCs or replace lead with tin elements. Compared to lead-based perovskites, Sn-Pb mixed perovskites have narrower bandgap, which is closer to the ideal bandgap of the active layer of single-junction solar cells, so Sn-Pb mixed perovskites can be used to achieve higher efficiency. In addition, Sn-Pb mixed perovskites can be used to the bottom sub-cell of perovskite/perovskite tandem photovoltaics and approach to the Shockley−Queisser limit of the PSCs. However, divalent tin can be oxidized into tetravalent tin, leading to the degradation of perovskite. Therefore, the mechanisms and inhibition methods of the oxidation of divalent tin within PSCs need further exploration.

Bibliography

[1] The Paris Agreement, The United Nations Framework Convention on Climate Change, https://unfccc.int/process-and-meetings/the-paris-agreement?gclid=Cj0KCQiAh8OtBhCQARIsAIkWb6-VcMp7mnX0BMCe4DlUH0GFVTl_rfGECsw9cyM2_FB-Oox-_mRDZ-IaApkAEALw_wcB.

[2] World Energy Transitions Outlook 2023, International Renewable Energy Agency, https://www.irena.org/Digital-Report/World-Energy-Transitions-Outlook-2023#page-0.

[3] Solar resource maps of World, Solargis, https://solargis.com/maps-and-gis-data/download/world.

[4] The Australian Concentrating Solar Thermal Value Proposition, Fichtner Australia Pty Ltd, Australian Solar Thermal Research Institute, https://assets-global.website-files.com/62f0907dd19c8b7e8ca7c71a/65277571ffb6ccecd3d53187_Final%20Report%20-%20CST%20Value%20Proposition%20web.pdf.

[5] Photovoltaics Report (February 2023), Fraunhofer ISE, https://www.ise.fraunhofer.de/de/veroeffentlichungen/studien/photovoltaics-report.html.

[6] Best Research-Cell Efficiency Chart, National Renewable Energy Laboratory, https://www.nrel.gov/pv/cell-efficiency.html (accessed: June 2024).

[7] Lin, H.; Yang, M.; Ru, X.; Wang, G.; Yin, S.; Peng, F.; Hong, C.; Qu, M.; Lu, J.; Fang, L.; Han, C.; Procel, P.; Isabella, O.; Gao, P.; Li, Z.; Xu, X. Silicon Heterojunction Solar Cells with up to 26.81% Efficiency Achieved by Electrically Optimized Nanocrystalline-Silicon Hole Contact Layers. *Nature Energy* **2023**, *8*, 789–799.

[8] Yu, C.; Gao, K.; Peng, C.; He, C.; Wang, S.; Shi, W.; Allen, V.; Zhang, J.; Wang, D.; Tian, G.; Zhang, Y.; Jia, W.; Song, Y.-H.; Hu, Y.; Colwell, J.; Xing, C.; Ma, Q.; Wu, H.; Guo, L. J.; Dong, G. Industrial-Scale Deposition of Nanocrystalline Silicon Oxide for 26.4%-Efficient Silicon Heterojunction Solar Cells with Copper Electrodes. *Nature Energy* **2023**, *8* (12), 1375–1385.

[9] Richter, A.; Müller, R.; Benick, J.; Feldmann, F.; Steinhauser, B.; Reichel, C.; Fell, A.; Bivour, M.; Hermle, M.; Glunz, S. W. Design Rules for High-Efficiency Both-Sides-Contacted Silicon Solar Cells with Balanced Charge Carrier Transport and Recombination Losses. *Nature Energy* **2021**, *6* (4), 429–438.

[10] Zhang, X.; Dumbrell, R.; Li, W.; Xu, M.; Yan, D.; Jin, J.; Wang, Z.; Zheng, P.; Liu, C.; Yang, J. Mass Production of Crystalline Silicon Solar Cells with Polysilicon-Based Passivating Contacts: An Industrial Perspective. *Progress in Photovoltaics: Research and Applications* **2022**, *31* (4), 369–379.

[11] Green, M. A.; Ho-Baillie, A.; Snaith, H. J. The Emergence of Perovskite Solar Cells. *Nature Photonics* **2014**, *8* (7), 506–514.

[12] Green, M. A.; Keevers, M. J. Optical Properties of Intrinsic Silicon at 300 K. *Progress in Photovoltaics: Research and Applications* **1995**, *3* (3), 189–192.

[13] Li, Y.; Ru, X.; Yang, M.; Zheng, Y.; Yin, S.; Hong, C.; Peng, F.; Qu, M.; Xue, C.; Lu, J.; Fang, L.; Su, C.; Chen, D.; Xu, J.; Yan, C.; Li, Z.; Xu, X.; Shao, Z. Flexible Silicon Solar Cells with High Power-To-Weight Ratios. *Nature* **2024**, *626* (7997), 105–110.

[14] Lee, M. M.; Teuscher, J.; Miyasaka, T.; Murakami, T. N.; Snaith, H. J. Efficient Hybrid Solar Cells Based on Meso-Superstructured Organometal Halide Perovskites. *Science* **2012**, *338* (6107), 643–647.

[15] Li, Z.; Yang, M.; Park, J.-S.; Wei, S.-H.; Berry, J. J.; Zhu, K. Stabilizing Perovskite Structures by Tuning Tolerance Factor: Formation of Formamidinium and Cesium Lead Iodide Solid-State Alloys. *Chemistry of Materials* **2015**, *28* (1), 284–292.

[16] Stranks, S. D.; Eperon, G. E.; Grancini, G.; Menelaou, C.; Alcocer, M. J. P.; Leijtens, T.; Herz, L. M.; Petrozza, A.; Snaith, H. J. Electron-Hole Diffusion Lengths Exceeding 1 Micrometer in an Organometal Trihalide Perovskite Absorber. *Science* **2013**, *342* (6156), 341–344.

[17] Miyata, A.; Mitioglu, A.; Plochocka, P.; Portugall, O.; Wang, J. T.-W.; Stranks, S. D.; Snaith, H. J.; Nicholas, R. J. Direct Measurement of the Exciton Binding Energy and Effective Masses for Charge Carriers in Organic–Inorganic Tri-Halide Perovskites. *Nature Physics* **2015**, *11* (7), 582–587.

[18] Im, J.-H.; Lee, C.-R.; Lee, J.-W.; Park, S.-W.; Park, N.-G. 6.5% Efficient Perovskite Quantum-Dot-Sensitized Solar Cell. *Nanoscale* **2011**, *3* (10), 4088.

[19] Park, N.-G. Perovskite Solar Cell: Research Direction for next 10 Years. *ACS Energy Letters* **2019**, *4* (12), 2983–2985.

[20] Shockley, W; Queisser, H. J. Detailed Balance Limit of Efficiency of *p-n* Junction Solar Cells. *Journal of Applied Physics* **1961***, 32* (3), 510–519.

[21] Köhnen, E.; Jošt, M.; Morales-Vilches, A. B.; Tockhorn, P.; Al-Ashouri, A.; Macco, B.; Kegelmann, L.; Korte, L.; Rech, B.; Schlatmann, R.; Stannowski, B.; Albrecht, S. Highly Efficient Monolithic Perovskite Silicon Tandem Solar Cells: Analyzing the Influence of Current Mismatch on Device Performance. *Sustainable Energy & Fuels* **2019**, *3* (8), 1995–2005.

[22] Leijtens, T.; Bush, K. A.; Prasanna, R.; McGehee, M. D. Opportunities and Challenges for Tandem Solar Cells Using Metal Halide Perovskite Semiconductors. *Nature Energy* **2018**, *3* (10), 828–838.

[23] Hoke, E. T.; Slotcavage, D. J.; Dohner, E. R.; Bowring, A. R.; Karunadasa, H. I.; McGehee, M. D. Reversible Photo-Induced Trap Formation in Mixed-Halide Hybrid Perovskites for Photovoltaics. *Chemical Science* **2015**, *6* (1), 613–617.

[24] Brennan, M. C.; Draguta, S.; Kamat, P. V.; Kuno, M. Light-Induced Anion Phase Segregation in Mixed Halide Perovskites. *ACS Energy Letters* **2017**, *3* (1), 204–213.

[25] Slotcavage, D. J.; Karunadasa, H. I.; McGehee, M. D. Light-Induced Phase Segregation in Halide-Perovskite Absorbers. *ACS Energy Letters* **2016**, *1* (6), 1199–1205.

[26] Ahmed, Y.; Khan, B.; Faheem, M. Bilal.; Huang, K.; Gao, Y.; Yang, J. Organic Additives in All-Inorganic Perovskite Solar Cells and Modules: From Moisture Endurance to Enhanced Efficiency and Operational Stability. *Journal of Energy Chemistry* **2022**, *67*, 361–390.

[27] Fu, W.; Chen, H.; Jen, A. K.-Y. Two-Dimensional Perovskites for Photovoltaics. *Materials Today Nano* **2021**, *14*, 100117.

[28] Cui, S.; Wang, J.; Xie, H.; Zhao, Y.; Li, Z.; Luo, S.; Ke, L.; Gao, Y.; Meng, K.; Ding, L.; Yuan, Y. Rubidium Ions Enhanced Crystallinity for Ruddlesden–Popper Perovskites. *Advanced Science* **2020**, *7* (24), 2002445.

[29] Hu, J.; Oswald, I. W. H.; Stuard, S. J.; Nahid, M. M.; Zhou, N.; Williams, O. F.; Guo, Z.; Yan, L.; Hu, H.; Chen, Z.; Xiao, X.; Lin, Y.; Yang, Z.; Huang, J.; Moran, A. M.; Ade, H.; Neilson, J. R.; You, W. Synthetic Control over Orientational Degeneracy of Spacer Cations Enhances Solar Cell Efficiency in Two-Dimensional Perovskites. *Nature Communications* **2019**, *10* (1), 1276.

[30] Lai, H.; Kan, B.; Liu, T.; Zheng, N.; Xie, Z.; Zhou, T.; Wan, X.; Zhang, X.; Liu, Y.; Chen, Y. Two-Dimensional Ruddlesden–Popper Perovskite with Nanorod-like Morphology for Solar Cells with Efficiency Exceeding 15%. *Journal of the American Chemical Society* **2018**, *140* (37), 11639–11646.

[31] Kojima, A.; Teshima, K.; Shirai, Y.; Miyasaka, T. Organometal Halide Perovskites as Visible-Light Sensitizers for Photovoltaic Cells. *Journal of the American Chemical Society* **2009**, *131* (17), 6050–6051.

[32] Kim, H.-S.; Lee, C.-R.; Im, J.-H.; Lee, K.-B.; Moehl, T.; Marchioro, A.; Moon, S.-J.; Humphry-Baker, R.; Yum, J.-H.; Moser, J. E.; Grätzel, M.; Park, N.-G. Lead Iodide Perovskite Sensitized All-Solid-State Submicron Thin Film Mesoscopic Solar Cell with Efficiency Exceeding 9%. *Scientific Reports* **2012**, *2* (1), 591.

[33] Liu, M.; Johnston, M. B.; Snaith, H. J. Efficient Planar Heterojunction Perovskite Solar Cells by Vapour Deposition. Nature **2013**, 501 (7467), 395–398.

[34] Breakthrough of the Year 2013, Science, https://www.science.org/content/article/breakthrough-year-2013.

[35] Mei, A.; Li, X.; Liu, L.; Ku, Z.; Liu, T.; Rong, Y.; Xu, M.; Hu, M.; Chen, J.; Yang, Y.; Grätzel, M.; Han, H. A Hole-Conductor-Free, Fully Printable Mesoscopic Perovskite Solar Cell with High Stability. *Science* **2014**, *345* (6194), 295–298.

[36] Bai, Y.; Yang, S.; Yang, S. Interface Engineering for Highly Efficient and Stable Planar p-i-n Perovskite Solar Cells. *Advanced Energy Materials* **2018**, *8* (5), 1701883.

[37] Yang, W. S.; Park, B.-W.; Jung, E. H.; Jeon, N. J.; Kim, Y. C.; Lee, D. U.; Shin, S. S.; Seo, J.; Kim, E. K.; Noh, J. H.; Seok, S. I. Iodide Management in Formamidinium-Lead-Halide–Based Perovskite Layers for Efficient Solar Cells. *Science* **2017**, *356* (6345), 1376–1379.

[38] Jeon, N. J.; Na, H.; Jung, E. H.; Yang, T.-Y.; Lee, Y. G.; Kim, G.; Shin, H.-W.; Seok, S. I.; Lee, J.; Seo, J. A Fluorene-Terminated Hole-Transporting Material for Highly Efficient and Stable Perovskite Solar Cells. *Nature Energy* **2018**, *3* (8), 682–689.

[39] Huang, K.; Peng, Y.; Gao, Y.; Shi, J.; Li, H.; Mo, X.; Huang, H.; Gao, Y.; Ding, L.; Yang, J. High-Performance Flexible Perovskite Solar Cells via Precise Control of Electron Transport Layer. *Advanced Energy Materials* **2019**, *9* (44), 1901419.

[40] Gong, C.; Tong, S.; Huang, K.; Li, H.; Huang, H.; Zhang, J.; Yang, J. Flexible Planar Heterojunction Perovskite Solar Cells Fabricated via Sequential Roll-To-Roll Microgravure Printing and Slot-Die Coating Deposition. *Solar RRL* **2019**, *4* (2), 1900204.

[41] Jiang, Q.; Tong, J.; Xian, Y.; Kerner, R. A.; Dunfield, S. P.; Xiao, C.; Scheidt, R. A.; Kuciauskas, D.; Wang, X.; Hautzinger, M. P.; Tirawat, R.; Beard, M. C.; Fenning, D. P.; Berry, J. J.; Larson, B. W.; Yan, Y.; Zhu, K. Surface Reaction for Efficient and Stable Inverted Perovskite Solar Cells. *Nature* **2022**, *611*, 278–283.

[42] Chen, P.; Xiao, Y.; Hu, J.; Li, S.; Luo, D.; Su, R.; Caprioglio, P.; Kaienburg, P.; Jia, X.; Chen, N.; Wu, J.; Sui, Y.; Tang, P.; Yan, H.; Huang, T.; Yu, M.; Li, Q.; Zhao, L.; Hou, C.-H.; You, Y.-W. Multifunctional Ytterbium Oxide Buffer for Perovskite Solar Cells. *Nature* **2024**, *625* (7995), 516–522.

[43] Park, J.; Kim, J.; Yun, H.-S.; Paik, M. J.; Noh, E.; Mun, H. J.; Kim, M. G.; Shin, T. J.; Seok, S. I. Controlled Growth of Perovskite Layers with Volatile Alkylammonium Chlorides. *Nature* **2023**, *616*, 724–730.

[44] Zhu, P.; Wang, D.; Zhang, Y.; Liang, Z.; Li, J.; Zeng, J.; Zhang, J.; Xu, Y.; Wu, S.; Liu, Z.; Zhou, X.; Hu, B.; He, F.; Zhang, L.; Pan, X.; Wang, X.; Park, N.-G.; Xu, B. Aqueous Synthesis of Perovskite Precursors for Highly Efficient Perovskite Solar Cells. *Science* **2024**, *383* (6682), 524–531.

[45] Jiang, Q.; Tong, J.; Scheidt, R. A.; Wang, X.; Louks, A. E.; Xian, Y.; Tirawat, R.; Palmstrom, A. F.; Hautzinger, M. P.; Harvey, S. P.; Johnston, S.; Schelhas, L. T.; Larson, B. W.; Warren, E. L.; Beard, M. C.; Berry, J. J.; Yan, Y.; Zhu, K. Compositional Texture Engineering for Highly Stable Wide-Bandgap Perovskite Solar Cells. *Science* **2022**, *378* (6626), 1295–1300.

[46] Li, M.; Xie, Y.; Lin, F. R.; Li, Z.; Yang, S.; Jen, A. K. - Y. Self-Assembled Monolayers as Emerging Hole-Selective Layers Enable High-Performance Thin-Film Solar Cells. *The Innovation* **2023**, *4* (1), 100369.

[47] Altinkaya, C.; Aydin, E.; Ugur, E.; Isikgor, F. H.; Subbiah, A. S.; De Bastiani, M.; Liu, J.; Babayigit, A.; Allen, T. G.; Laquai, F.; Yildiz, A.; De Wolf, S. Tin Oxide Electron-Selective Layers for Efficient, Stable, and Scalable Perovskite Solar Cells. *Advanced Materials* **2021**, *33* (15), 2005504.

[48] Ke, W.; Fang, G.; Liu, Q.; Xiong, L.; Qin, P.; Tao, H.; Wang, J.; Lei, H.; Li, B.; Wan, J.; Yang, G.; Yan, Y. Low-Temperature Solution-Processed Tin Oxide as an Alternative Electron Transporting Layer for Efficient Perovskite Solar Cells. *Journal of the American Chemical Society* **2015**, *137* (21), 6730–6733.

[49] Baena, J. P. C.; Steier, L.; Tress, W.; Saliba, M.; Neutzner, S.; Matsui, T.; Giordano, F.; Jacobsson, T. J.; Kandada, A. R. S.; Zakeeruddin, S. M.; Petrozza, A.; Abate, A.; Nazeeruddin, M. K.; Grätzel, M.; Hagfeldt, A. Highly Efficient Planar Perovskite Solar Cells through Band Alignment Engineering. *Energy & Environmental Science* **2015**, *8* (10), 2928–2934.

[50] Jiang, Q.; Zhang, L.; Wang, H.; Yang, X.; Meng, J.; Liu, H.; Yin, Z.; Wu, J.; Zhang, X.; You, J. Enhanced Electron Extraction Using SnO_2 for High-Efficiency Planar-Structure $HC(NH_2)_2PbI_3$-Based Perovskite Solar Cells. *Nature Energy* **2016**, *2* (1), 16177.

[51] Zhao, Y.; Ma, F.; Qu, Z.; Yu, S.; Shen, T.; Deng, H.-X.; Chu, X.; Peng, X.; Yuan, Y.; Zhang, X.; You, J. Inactive $(PbI_2)_2RbCl$ Stabilizes Perovskite Films for Efficient Solar Cells. *Science* **2022**, *377* (6605), 531–534.

[52] Xu, R.; Pan, F.; Chen, J.; Li, J.; Yang, Y.; Sun, Y.; Zhu, X.; Li, P.; Cao, X.; Xi, J.; Xu, J.; Yuan, F.; Dai, J.; Zuo, C.; Ding, L.; Dong, H.; Jen, A. K. -Y.; Wu, Z. Optimizing the Buried Interface in Flexible Perovskite Solar Cells to Achieve over 24% Efficiency and Long-Term Stability. *Advanced Materials* **2023**, 2308039.

[53] Löper, P.; Moon, S.-J.; Nicolas, S. M. de; Niesen, B.; Ledinsky, M.; Nicolay, S.; Bailat, J.; Yum, J.-H.; Wolf, S. D.; Ballif, C. Organic–Inorganic Halide Perovskite/Crystalline Silicon Four-Terminal Tandem Solar Cells. *Physical Chemistry Chemical Physics* **2015**, *17* (3), 1619–1629.

[54] Bailie, C. D.; Christoforo, M. G.; Mailoa, J. P.; Bowring, A. R.; Unger, E. L.; Nguyen, W. H.; Burschka, J.; Pellet, N.; Lee, J. Z.; Grätzel, M.; Noufi, R.; Buonassisi, T.; Salleo, A.; McGehee, M. D. Semi-Transparent Perovskite Solar

Cells for Tandems with Silicon and CIGS. *Energy & Environmental Science* **2015**, *8* (3), 956–963.

[55] Werner, J.; Dubuis, G.; Walter, A.; Löper, P.; Moon, S.-J.; Nicolay, S.; Morales-Masis, M.; De Wolf, S.; Niesen, B.; Ballif, C. Sputtered Rear Electrode with Broadband Transparency for Perovskite Solar Cells. *Solar Energy Materials and Solar Cells* **2015**, *141*, 407–413.

[56] Zheng, J.; Duan, W.; Guo, Y.; Zhao, Z. C.; Yi, H.; Ma, F.; Caro, L. G.; Yi, C.; Bing, J.; Tang, S.; Qu, J.; Fong, K. C.; Cui, X.; Zhu, Y.; Yang, L.; Lambertz, A.; Mahmud, M. A.; Chen, H.; Liao, C.; Wang, G. Efficient Monolithic Perovskite–Si Tandem Solar Cells Enabled by an Ultra-Thin Indium Tin Oxide Interlayer. *Energy and Environmental Science* **2023**, *16* (3), 1223–1233.

[57] Mailoa, J. P.; Bailie, C. D.; Johlin, E. C.; Hoke, E. T.; Akey, A. J.; Nguyen, W. H.; McGehee, M. D.; Buonassisi, T. A 2-Terminal Perovskite/Silicon Multijunction Solar Cell Enabled by a Silicon Tunnel Junction. *Applied Physics Letters* **2015**, *106* (12), 121105.

[58] Duan, L.; Walter, D.; Chang, N.; Bullock, J.; Kang, D.; Phang, S. P.; Weber, K.; White, T.; Macdonald, D.; Catchpole, K.; Shen, H. Stability Challenges for the Commercialization of Perovskite–Silicon Tandem Solar Cells. *Nature Reviews Materials* **2023**, *8*, 261–281.

[59] Aydın, E.; Allen, T. G.; Bastiani, M. D.; Razzaq, A.; Xu, L.; Ugur, E.; Liu, J.; Wolf, S. D. Pathways toward Commercial Perovskite/Silicon Tandem Photovoltaics. *Science* **2024**, *383* (6679), eadh3849.

[60] Duong, T.; Nguyen, T.; Huang, K.; Pham, H. T. M.; Adhikari, S. G.; Khan, M. R.; Duan, L.; Liang, W.; Fong, K. C.; Shen, H.; Bui, A. D.; Mayon, A. O.; Truong, T. N.; Tabi, G. D.; Ahmad, V. U.; Surve, S.; Tong, J.; Kho, T.; Trần-Phú, T.; Lü, T. Bulk Incorporation with 4-Methylphenethylammonium Chloride for Efficient and Stable Methylammonium-Free Perovskite and Perovskite-Silicon Tandem Solar Cells. *Advanced Energy Materials* **2023**, *13* (9), 2203607.

[61] Chin, X. Y.; Turkay, D.; Steele, J. A.; Tabean, S.; Eswara, S.; Mensi, M.; Peter, F.; Wolff, C.; Paracchino, A.; Artuk, K.; Jacobs, D. A.; Guesnay, Q.; Sahli, F.; Andreatta, G.; Boccard, M.; Jeangros, Q.; Ballif, C. Interface Passivation for 31.25%-Efficient Perovskite/Silicon Tandem Solar Cells. *Science* **2023**, *381* (6653), 59–63.

[62] Aydin, E.; Ugur, E.; Yildirim, B. K.; Allen, T. G.; Dally, P.; Razzaq, A.; Cao, F.; Xu, L.; Vishal, B.; Yazmaciyan, A.; Said, A. A.; Zhumagali, S.; Azmi, R.; Babics, M.; Fell, A.; Xiao, C.; De Wolf, S. Enhanced Optoelectronic Coupling for Perovskite-Silicon Tandem Solar Cells. *Nature* **2023**, *623*, 732–738.

[63] Mariotti, S.; Köhnen, E.; Scheler, F.; Sveinbjörnsson, K.; Zimmermann, L.; Piot, M.; Yang, F.; Li, B.; Warby, J.; Musiienko, A.; Menzel, D.; Lang, F.; Keßler, S.; Levine, I.; Mantione, D.; Al-Ashouri, A.; Härtel, M. S.; Xu, K.; Cruz, A.;

Kurpiers, J. Interface Engineering for High-Performance, Triple-Halide Perovskite–Silicon Tandem Solar Cells. *Science* **2023**, *381* (6653), 63–69.

[64] Said, A. A.; Aydin, E.; Ugur, E.; Xu, Z.; Deger, C.; Vishal, B.; Vlk, A.; Dally, P.; Yildirim, B. K.; Azmi, R.; Liu, J.; Jackson, E. A.; Johnson, H. M.; Gui, M.; Richter, H.; Pininti, A. R.; Bristow, H.; Babics, M.; Razzaq, A.; Allen, T. G. Sublimed C_{60} for Efficient and Repeatable Perovskite-Based Solar Cells. *Nature Communications* **2024**, *15* (1), 708.

[65] Vos, A. D. Detailed Balance Limit of the Efficiency of Tandem Solar Cells. *Journal of Physics D: Applied Physics* **1980**, *13* (5), 839–846.

[66] Miller, O. D.; Yablonovitch, E.; Kurtz, S. R. Strong Internal and External Luminescence as Solar Cells Approach the Shockley–Queisser Limit. *IEEE Journal of Photovoltaics* **2012**, *2* (3), 303–311.

[67] Sha, W. E. I.; Ren, X.; Chen, L.; Choy, W. C. H. The Efficiency Limit of $CH_3NH_3PbI_3$ Perovskite Solar Cells. *Applied Physics Letters* **2015**, *106* (22), 221104.

[68] You, J.; Yang, Y. (Michael); Hong, Z.; Song, T.-B.; Meng, L.; Liu, Y.; Jiang, C.; Zhou, H.; Chang, W.-H.; Li, G.; Yang, Y. Moisture Assisted Perovskite Film Growth for High Performance Solar Cells. *Applied Physics Letters* **2014**, *105* (18), 183902.

[69] Huang, K.; Wang, C.; Zhang, C.; Tong, S.; Li, H.; Liu, B.; Gao, Y.; Dong, Y.; Gao, Y.; Peng, Y.; Yang, J. Efficient and Stable Planar Heterojunction Perovskite Solar Cells Fabricated under Ambient Conditions with High Humidity. *Organic Electronics* **2018**, *55*, 140–145.

[70] Li, H.; Feng, X.; Huang, K.; Lu, S.; Wang, X.; Feng, E.; Chang, J.; Long, C.; Gao, Y.; Chen, Z.; Yi, C.; He, J.; Yang, J. Constructing Additives Synergy Strategy to Doctor-Blade Efficient $CH_3NH_3PbI_3$ Perovskite Solar Cells under a Wide Range of Humidity from 45% to 82%. *Small* **2023**, *19* (24), 2300374.

[71] Huang, K.; Li, H.; Zhang, C.; Gao, Y.; Liu, T.; Zhang, J.; Gao, Y.; Peng, Y.; Ding, L.; Yang, J. Highly Efficient Perovskite Solar Cells Processed under Ambient Conditions Using in Situ Substrate-Heating-Assisted Deposition. *Solar RRL* **2019**, *3* (3), 1800318.

[72] Cheng, Y.; Xu, X.; Xie, Y.; Li, H.-W.; Qing, J.; Ma, C.; Lee, C.-S.; So, F.; Tsang, S.-W. 18% High-Efficiency Air-Processed Perovskite Solar Cells Made in a Humid Atmosphere of 70% RH. *Solar RRL* **2017**, *1* (9), 1700097.

[73] Wang, Z.; Jin, J.; Zheng, Y.; Zhang, X.; Zhu, Z.; Zhou, Y.; Cui, X.; Li, J.; Shang, M.; Zhao, X.; Liu, S.; Tai, Q. Achieving Efficient and Stable Perovskite Solar Cells in Ambient Air through Non-Halide Engineering. *Advanced Energy Materials* **2021**, *11* (42), 2102169.

[74] Tai, Q.; You, P.; Sang, H.; Liu, Z.; Hu, C.; Chan, H. L. W.; Yan, F. Efficient and

Stable Perovskite Solar Cells Prepared in Ambient Air Irrespective of the Humidity. *Nature Communications* **2016**, *7* (1), 11105.

[75] Zhao, J.; O. Fürer, S.; P. McMeekin, D.; Lin, Q.; Lv, P.; Ma, J.; Liang Tan, W.; Wang, C.; Tan, B.; R. Chesman, A. S.; Yin, H.; D. Scully, A.; R. McNeill, C.; Mao, W.; Lu, J.; Cheng, Y.-B.; Bach, U. Efficient and Stable Formamidinium–Caesium Perovskite Solar Cells and Modules from Lead Acetate-Based Precursors. *Energy & Environmental Science* **2023**, *16* (1), 138–147.

[76] Tang, X.; Brandl, M.; May, B.; Levchuk, I.; Hou, Y.; Richter, M.; Chen, H.; Chen, S.; Kahmann, S.; Osvet, A.; Maier, F.; Steinrück, H.-P.; Hock, R.; Matt, G. J.; Brabec, C. J. Photoinduced Degradation of Methylammonium Lead Triiodide Perovskite Semiconductors. *Journal of Materials Chemistry A* **2016**, *4* (41), 15896–15903.

[77] Liang, J.; Hu, X.; Wang, C.; Liang, C.; Chen, C.; Xiao, M.; Li, J.; Tao, C.; Xing, G.; Yu, R.; Ke, W.; Fang, G. Origins and Influences of Metallic Lead in Perovskite Solar Cells. *Joule* **2022**, *6* (4), 816–833.

[78] Tumen-Ulzii, G.; Qin, C.; Klotz, D.; Leyden, M. R.; Wang, P.; Auffray, M.; Fujihara, T.; Matsushima, T.; Lee, J.; Lee, S.; Yang, Y.; Adachi, C. Detrimental Effect of Unreacted PbI_2 on the Long-Term Stability of Perovskite Solar Cells. *Advanced Materials* **2020**, *32* (16), 1905035.

[79] Xie, L.; Liu, J.; Li, J.; Liu, C.; Pu, Z.; Xu, P.; Wang, Y.; Meng, Y.; Yang, M.; Ge, Z. A Deformable Additive on Defects Passivation and Phase Segregation Inhibition Enables the Efficiency of Inverted Perovskite Solar Cells over 24%. *Advanced Materials* **2023**, *35* (38), 2302752.

[80] Zheng, Y.; Wu, X.; Liang, J.; Zhang, Z.; Jiang, J.-H.; Wang, J.; Huang, Y.; Tian, C.; Wang, L.; Chen, Z.; Chen, C. Downward Homogenized Crystallization for Inverted Wide-Bandgap Mixed-Halide Perovskite Solar Cells with 21% Efficiency and Suppressed Photo-Induced Halide Segregation. *Advanced Functional Materials* **2022**, *32* (29), 2200431.

[81] Wei, J.; Wang, Q.; Huo, J.; Gao, F.; Gan, Z.; Zhao, Q.; Li, H. Mechanisms and Suppression of Photoinduced Degradation in Perovskite Solar Cells. *Advanced Energy Materials* **2020**, *11* (3), 2002326.

[82] Jiang, Q.; Chu, Z.; Wang, P.; Yang, X.; Liu, H.; Wang, Y.; Yin, Z.; Wu, J.; Zhang, X.; You, J. Planar-Structure Perovskite Solar Cells with Efficiency beyond 21%. *Advanced Materials* **2017**, *29* (46), 1703852.

[83] Roose, B.; Dey, K.; Chiang, Y.-H.; Friend, R. H.; Stranks, S. D. Critical Assessment of the Use of Excess Lead Iodide in Lead Halide Perovskite Solar Cells. *The Journal of Physical Chemistry Letters* **2020**, *11* (16), 6505–6512.

[84] Jacobsson, T. J.; Correa-Baena, J.-P.; Anaraki, E. H.; Philippe, B.; Stranks, S. D.; Bouduban, M. E. F.; Tress, W.; Schenk, K.; Teuscher, J.; Moser, Jacques-E.;

Rensmo, H.; Hagfeldt, A. Unreacted PbI_2 as a Double-Edged Sword for Enhancing the Performance of Perovskite Solar Cells. *Journal of the American Chemical Society* **2016**, *138* (32), 10331–10343.

[85] Conings, B.; Drijkoningen, J.; Gauquelin, N.; Babayigit, A.; D'Haen, J.; D'Olieslaeger, L.; Ethirajan, A.; Verbeeck, J.; Manca, J.; Mosconi, E.; Angelis, F. D.; Boyen, H.-G. Intrinsic Thermal Instability of Methylammonium Lead Trihalide Perovskite. *Advanced Energy Materials* **2015**, *5* (15), 1500477.

[86] Turren-Cruz, S.-H.; Hagfeldt, A.; Saliba, M. Methylammonium-Free, High-Performance, and Stable Perovskite Solar Cells on a Planar Architecture. *Science* **2018**, *362* (6413), 449–453.

[87] Malinauskas, T.; Tomkute-Luksiene, D.; Sens, R.; Daskeviciene, M.; Send, R.; Wonneberger, H.; Jankauskas, V.; Bruder, I.; Getautis, V. Enhancing Thermal Stability and Lifetime of Solid-State Dye-Sensitized Solar Cells via Molecular Engineering of the Hole-Transporting Material Spiro-OMeTAD. *ACS Applied Materials & Interfaces* **2015**, *7* (21), 11107–11116.

[88] Jena, A. K.; Numata, Y.; Ikegami, M.; Miyasaka, T. Role of Spiro-OMeTAD in Performance Deterioration of Perovskite Solar Cells at High Temperature and Reuse of the Perovskite Films to Avoid Pb-Waste. *Journal of Materials Chemistry A* **2018**, *6* (5), 2219–2230.

[89] Miyazawa, Y.; Ikegami, M.; Miyasaka, T.; Ohshima, T.; Imaizumi, M.; Hirose, K. Evaluation of Radiation Tolerance of Perovskite Solar Cell for Use in Space. *IEEE 42nd Photovoltaic Specialist Conference (PVSC)* **2015**. DOI: 10.1109/PVSC.2015.7355859.

[90] Lang, F.; Nickel, N. H.; Bundesmann, J.; Seidel, S.; Denker, A.; Albrecht, S.; Brus, V. V.; Rappich, J.; Rech, B.; Landi, G.; Neitzert, H. C. Radiation Hardness and Self-Healing of Perovskite Solar Cells. *Advanced Materials* **2016**, *28* (39), 8726–8731.

[91] Yang, S.; Xu, Z.; Xue, S.; Kandlakunta, P.; Cao, L.; Huang, J. Organohalide Lead Perovskites: More Stable than Glass under Gamma-Ray Radiation. *Advanced Materials* **2018**, *31* (4), 1805547.

[92] Yang, K.; Huang, K.; Li, X.; Zheng, S.; Hou, P.; Wang, J.; Guo, H.; Song, H.; Li, B.; Li, H.; Liu, B.; Zhong, X.; Yang, J. Radiation Tolerance of Perovskite Solar Cells under Gamma Ray. *Organic Electronics* **2019**, *71*, 79–84.

[93] Huang, K.; Yang, K.; Li, H.; Zheng, S.; Wang, J.; Guo, H.; Peng, Y.; Zhong, X.; Yang, J. γ-Ray Radiation on Flexible Perovskite Solar Cells. *ACS Applied Energy Materials* **2020**, *3* (8), 7318–7324.

[94] Kim, G.; Min, H.; Lee, K. S.; Lee, D. Y.; Yoon, S. M.; Seok, S. I. Impact of Strain Relaxation on Performance of α-Formamidinium Lead Iodide Perovskite Solar Cells. *Science* **2020**, *370* (6512), 108–112.

[95] Zhao, J.; Deng, Y.; Wei, H.; Zheng, X.; Yu, Z.; Shao, Y.; Shield, J. E.; Huang, J. Strained Hybrid Perovskite Thin Films and Their Impact on the Intrinsic Stability of Perovskite Solar Cells. *Science Advances* **2017**, *3* (11), eaao5616.

[96] Zhu, C.; Niu, X.; Fu, Y.; Li, N.; Hu, C.; Chen, Y.; He, X.; Na, G.; Liu, P.; Zai, H.; Ge, Y.; Lu, Y.; Ke, X.; Bai, Y.; Yang, S.; Chen, P.; Li, Y.; Sui, M.; Zhang, L.; Zhou, H. Strain Engineering in Perovskite Solar Cells and Its Impacts on Carrier Dynamics. *Nature Communications* **2019**, *10* (1), 815.

[97] Wang, H.; Zhu, C.; Liu, L.; Ma, S.; Liu, P.; Wu, J.; Shi, C.; Du, Q.; Hao, Y.; Xiang, S.; Chen, H.; Chen, P.; Bai, Y.; Zhou, H.; Li, Y.; Chen, Q. Interfacial Residual Stress Relaxation in Perovskite Solar Cells with Improved Stability. *Advanced Materials* **2019**, *31* (48), 1904408.

[98] Zhou, Q.; Duan, J.; Yang, X.; Duan, Y.; Tang, Q. Interfacial Strain Release from the $WS_2/CsPbBr_3$ van Der Waals Heterostructure for 1.7 V Voltage All-Inorganic Perovskite Solar Cells. *Angewandte Chemie International Edition* **2020**, *59* (49), 21997–22001.

[99] Chen, Y.; Lei, Y.; Li, Y.; Yu, Y.; Cai, J.; Chiu, M.-H.; Rao, R.; Gu, Y.; Wang, C.; Choi, W.; Hu, H.; Wang, C.; Li, Y.; Song, J.; Zhang, J.; Qi, B.; Lin, M.; Zhang, Z.; Islam, A. E.; Maruyama, B. Strain Engineering and Epitaxial Stabilization of Halide Perovskites. *Nature* **2020**, *577* (7789), 209–215.

[100] Razera, R. A. Z.; Jacobs, D. A.; Fu, F.; Fiala, P.; Dussouillez, M.; Sahli, F.; Yang, T. C. J.; Ding, L.; Walter, A.; Feil, A. F.; Boudinov, H. I.; Nicolay, S.; Ballif, C.; Jeangros, Q. Instability of P–I–N Perovskite Solar Cells under Reverse Bias. *Journal of Materials Chemistry A* **2020**, *8* (1), 242–250.

[101] Bowring, A. R.; Bertoluzzi, L.; O'Regan, B. C.; McGehee, M. D. Reverse Bias Behavior of Halide Perovskite Solar Cells. *Advanced Energy Materials* **2017**, *8* (8), 1702365.

[102] Bertoluzzi, L.; Patel, J. B.; Bush, K. A.; Boyd, C. C.; Kerner, R. A.; O'Regan, B. C.; McGehee, M. D. Incorporating Electrochemical Halide Oxidation into Drift-Diffusion Models to Explain Performance Losses in Perovskite Solar Cells under Prolonged Reverse Bias. *Advanced Energy Materials* **2021**, *11* (10), 2002614.

[103] Ni, Z.; Jiao, H.; Fei, C.; Gu, H.; Xu, S.; Yu, Z.; Yang, G.; Deng, Y.; Jiang, Q.; Liu, Y.; Yan, Y.; Huang, J. Evolution of Defects during the Degradation of Metal Halide Perovskite Solar Cells under Reverse Bias and Illumination. *Nature Energy* **2021**, *7* (1), 65–73.

[104] Chen, B.; Rudd, P. N.; Yang, S.; Yuan, Y.; Huang, J. Imperfections and Their Passivation in Halide Perovskite Solar Cells. *Chemical Society Reviews* **2019**, *48* (14), 3842–3867.

[105] Rajagopal, A.; Williams, S. T.; Chueh, C.-C.; Jen, A. K.-Y. Abnormal Current–Voltage Hysteresis Induced by Reverse Bias in Organic–Inorganic Hybrid

Perovskite Photovoltaics. *The Journal of Physical Chemistry Letters* **2016**, *7* (6), 995–1003.

[106] Ma, C.; Kim, B.; Kang, D.-H.; Kim, S. H.; Park, N.-G. Nonchemical *N*- and *P*-Type Charge Transfer Doping of $FAPbI_3$ Perovskite. *ACS Energy Letters* **2021**, *6* (8), 2817–2824.

[107] Heo, S.; Roh, K.; Zhang, F.; Tignor, S. E.; Bocarsly, A. B.; Kahn, A.; Rand, B. P. Electrochemically n-Doped $CsPbBr_3$ Nanocrystal Thin Films. *ACS Energy Letters* **2021**, *7* (1), 211–216.

[108] Wu, J.; Li, Y.; Tan, S.; Yu, B.; Li, H.; Li, Y.; Shi, J.; Wu, H.; Luo, Y.; Li, D.; Meng, Q. Enhanced Perovskite Solar Cell Efficiency via the Electric-Field-Induced Approach. *ACS Applied Materials & Interfaces* **2020**, *12* (24), 27258–27267.

[109] Jeong, K.; Byeon, J.; Jang, J.; Ahn, N.; Choi, M. Pulsatile Therapy for Perovskite Solar Cells. *Joule* **2022**, *6* (5), 1087–1102.

[110] Domanski, K.; Roose, B.; Matsui, T.; Saliba, M.; Turren-Cruz, S.-H.; Correa-Baena, J.-P.; Carmona, C. R.; Richardson, G.; Foster, J. M.; De Angelis, F.; Ball, J. M.; Petrozza, A.; Mine, N.; Nazeeruddin, M. K.; Tress, W.; Grätzel, M.; Steiner, U.; Hagfeldt, A.; Abate, A. Migration of Cations Induces Reversible Performance Losses over Day/Night Cycling in Perovskite Solar Cells. *Energy & Environmental Science* **2017**, *10* (2), 604–613.

[111] Domanski, K.; Alharbi, E. A.; Hagfeldt, A.; Grätzel, M.; Tress, W. Systematic Investigation of the Impact of Operation Conditions on the Degradation Behaviour of Perovskite Solar Cells. *Nature Energy* **2018**, *3* (1), 61–67.

[112] Saliba, M. Perovskite Solar Cells Must Come of Age. *Science* **2018**, *359* (6374), 388–389.

[113] Yun, J. H.; Kim, J.; Young, T. M.; Patterson, R.; Kim, D. H.; Seidel, J.; Lim, S.; Green, M. A.; Huang, S.; Ho-Baillie, A. Humidity-Induced Degradation via Grain Boundaries of $HC(NH_2)_2$ PbI_3 Planar Perovskite Solar Cells. *Advanced Functional Materials* **2018**, *28* (11), 1705363.

[114] Bruijnaers, B. J.; Schiepers, E.; Weijtens, C. H. L.; Meskers, S. C. J.; Wienk, M. M.; Janssen, R. A. J. The Effect of Oxygen on the Efficiency of Planar P–I–N Metal Halide Perovskite Solar Cells with a PEDOT:PSS Hole Transport Layer. *Journal of Materials Chemistry A* **2018**, *6* (16), 6882–6890.

[115] Wan, F.; Qiu, X.; Chen, H.; Liu, Y.; Xie, H.; Shi, J.; Huang, H.; Yuan, Y.; Gao, Y.; Zhou, C. Accelerated Electron Extraction and Improved UV Stability of TiO_2 Based Perovskite Solar Cells by SnO_2 Based Surface Passivation. *Organic Electronics* **2018**, *59*, 184–189.

[116] Xu, L.; Wan, F.; Rong, Y.; Chen, H.; He, S.; Xu, X.; Liu, G.; Han, H.; Yuan, Y.; Yang, J.; Gao, Y.; Yang, B.; Zhou, C. Stable Monolithic Hole-Conductor-Free Perovskite Solar Cells Using TiO_2 Nanoparticle Binding Carbon Films. *Organic*

Electronics **2017**, *45*, 131–138.

[117] Chen, H.; Chen, Y.; Zhang, T.; Liu, X.; Wang, X.; Zhao, Y. Advances to High-Performance Black-Phase $FAPbI_3$ Perovskite for Efficient and Stable Photovoltaics. *Small Structures* **2021**, *2* (5), 2000130.

[118] Silverman, T. J.; Deceglie, M. G.; Sun, X.; Garris, R. L.; Alam, M. A.; Deline, C.; Kurtz, S. Thermal and Electrical Effects of Partial Shade in Monolithic Thin-Film Photovoltaic Modules. *IEEE Journal of Photovoltaics* **2015**, *5* (6), 1742–1747.

[119] Wang, C.; Zhang, C.; Wang, S.; Liu, G.; Xia, H.; Tong, S.; He, J.; Niu, D.; Zhou, C.; Ding, K.; Gao, Y.; Yang, J. Low-Temperature Processed, Efficient, and Highly Reproducible Cesium-Doped Triple Cation Perovskite Planar Heterojunction Solar Cells. *Solar RRL* **2018**, *2* (2), 1700209.

[120] Jiang, Q.; Zhao, Y.; Zhang, X.; Yang, X.; Chen, Y.; Chu, Z.; Ye, Q.; Li, X.; Yin, Z.; You, J. Surface Passivation of Perovskite Film for Efficient Solar Cells. *Nature Photonics* **2019**, *13* (7), 460–466.

[121] Yoo, J. J.; Seo, G.; Chua, M. R.; Park, T. G.; Lu, Y.; Rotermund, F.; Kim, Y.-K.; Moon, C. S.; Jeon, N. J.; Correa-Baena, J.-P.; Bulović, V.; Shin, S. S.; Bawendi, M. G.; Seo, J. Efficient Perovskite Solar Cells via Improved Carrier Management. *Nature* **2021**, *590* (7847), 587–593.

[122] Li, S.; Zhang, P.; Chen, H.; Wang, Y.; Liu, D.; Wu, J.; Sarvari, H.; Chen, Z. D. Mesoporous PbI_2 Assisted Growth of Large Perovskite Grains for Efficient Perovskite Solar Cells Based on ZnO Nanorods. *Journal of Power Sources* **2017**, *342*, 990–997.

[123] Liu, Z.; Hu, J.; Jiao, H.; Li, L.; Zheng, G.; Chen, Y.; Huang, Y.; Zhang, Q.; Shen, C.; Chen, Q.; Zhou, H. Chemical Reduction of Intrinsic Defects in Thicker Heterojunction Planar Perovskite Solar Cells. *Advanced Materials* **2017**, *29* (23), 1606774.

[124] Kim, T. W.; Kim, M.; Cojocaru, L.; Uchida, S.; Segawa, H. Direct Observation of the Tunneling Phenomenon in Organometal Halide Perovskite Solar Cells and Its Influence on Hysteresis. *ACS Energy Letters* **2018**, *3* (11), 2743–2749.

[125] Zhang, H.; Xiao, J.; Shi, J.; Su, H.; Luo, Y.; Li, D.; Wu, H.; Cheng, Y.-B.; Meng, Q. Self-Adhesive Macroporous Carbon Electrodes for Efficient and Stable Perovskite Solar Cells. *Advanced Functional Materials* **2018**, *28* (39), 1802985.

[126] Hafner, J. Ab-Initiosimulations of Materials Using VASP: Density-Functional Theory and Beyond. *Journal of Computational Chemistry* **2008**, *29* (13), 2044–2078.

[127] Perdew, J. P.; Burke, K.; Ernzerhof, M. Generalized Gradient Approximation Made Simple. *Physical Review Letters* **1996**, *77* (18), 3865–3868.

[128] Csonka, G. I.; Perdew, J. P.; Ruzsinszky, A.; Philipsen, P. H. T.; Lebègue, S.; Paier,

J.; Vydrov, O. A.; Ángyán, J. G. Assessing the Performance of Recent Density Functionals for Bulk Solids. *Physical Review B* **2009**, *79* (15), 155107.

[129] Gao, Y.; Huang, K.; Long, C.; Ding, Y.; Chang, J.; Zhang, Y.; Etgar, L.; Liu, M.; Zhang, J.; Yang, J. Flexible Perovskite Solar Cells: From Materials and Device Architectures to Applications. *ACS energy letters* **2022**, *7* (4), 1412–1445.

[130] Chang, J.; Liu, K.; Lin, S.; Yuan, Y.; Zhou, C.; Yang, J. Solution-Processed Perovskite Solar Cells. *Journal of Central South University* **2020**, *27* (4), 1104–1133.

[131] Li, W.; Huang, K.; Chang, J.; Hu, C.; Long, C.; Zhang, H.; Maldague, X.; Liu, B.; Meng, J.; Duan, Y.; Yang, J. Sparkling Hot Spots in Perovskite Solar Cells under Reverse Bias. *ChemPhysMater* **2022**, *1* (1), 71–76.

[132] Yang, D.; Yang, R.; Wang, K.; Wu, C.; Zhu, X.; Feng, J.; Ren, X.; Fang, G.; Priya, S.; Liu, S. High Efficiency Planar-Type Perovskite Solar Cells with Negligible Hysteresis Using EDTA-Complexed SnO_2. *Nature Communications* **2018**, *9* (1), 3239.

[133] Liu, Y.; He, B.; Duan, J.; Zhao, Y.; Ding, Y.; Tang, M.; Chen, H.; Tang, Q. Poly(3-Hexylthiophene)/Zinc Phthalocyanine Composites for Advanced Interface Engineering of 10.03%-Efficiency $CsPbBr_3$ Perovskite Solar Cells. *Journal of Materials Chemistry A* **2019**, *7* (20), 12635–12644.

[134] Zhao, Y.; Zhou, W.; Tan, H.; Fu, R.; Li, Q.; Lin, F.; Yu, D.; Walters, G.; Sargent, E. H.; Zhao, Q. Mobile-Ion-Induced Degradation of Organic Hole-Selective Layers in Perovskite Solar Cells. *The Journal of Physical Chemistry C* **2017**, *121* (27), 14517–14523.

[135] Bae, S.; Kim, S.; Lee, S.-W.; Cho, K. J.; Park, S.; Lee, S.; Kang, Y.; Lee, H.-S.; Kim, D. Electric-Field-Induced Degradation of Methylammonium Lead Iodide Perovskite Solar Cells. *The Journal of Physical Chemistry Letters* **2016**, *7* (16), 3091–3096.

[136] Haruyama, J.; Sodeyama, K.; Han, L.; Tateyama, Y. First-Principles Study of Ion Diffusion in Perovskite Solar Cell Sensitizers. *Journal of the American Chemical Society* **2015**, *137* (32), 10048–10051.

[137] Azpiroz, J. M.; Mosconi, E.; Bisquert, J.; Angelis, F. D. Defect Migration in Methylammonium Lead Iodide and Its Role in Perovskite Solar Cell Operation. *Energy & Environmental Science* **2015**, *8* (7), 2118–2127.

[138] Zhuang, J.; Mao, P.; Luan, Y.; Chen, N.; Cao, X.; Niu, G.; Jia, F.; Wang, F.; Cao, S.; Wang, J. Rubidium Fluoride Modified SnO_2 for Planar N-I-P Perovskite Solar Cells. *Advanced Functional Materials* **2021**, *31* (17), 2010385.

[139] Bi, H.; Liu, B.; He, D.; Bai, L.; Wang, W.; Zang, Z.; Chen, J. Interfacial Defect Passivation and Stress Release by Multifunctional KPF_6 Modification for Planar Perovskite Solar Cells with Enhanced Efficiency and Stability. *Chemical*

Engineering Journal **2021**, *418*, 129375.

[140] Xiong, Z.; Chen, X.; Zhang, B.; Odunmbaku, G. O.; Ou, Z.; Guo, B.; Yang, K.; Kan, Z.; Lu, S.; Chen, S.; Ouedraogo, N. A. N.; Cho, Y.; Yang, C.; Chen, J.; Sun, K. Simultaneous Interfacial Modification and Crystallization Control by Biguanide Hydrochloride for Stable Perovskite Solar Cells with PCE of 24.4%. *Advanced Materials* **2022**, *34* (8), 2106118.

[141] Oranskaia, A.; Schwingenschlögl, U. Suppressing X-Migrations and Enhancing the Phase Stability of Cubic $FAPbX_3$ (X = Br, I). *Advanced Energy Materials* **2019**, *9* (32), 1901411.

[142] Yun, J. H.; Seidel, J.; Kim, J.; Soufiani, A. M.; Huang, S.; Lau, J. C.; Jeon, N. J.; Seok, S. I.; Green, M. A.; Ho-Baillie, A. Critical Role of Grain Boundaries for Ion Migration in Formamidinium and Methylammonium Lead Halide Perovskite Solar Cells. *Advanced Energy Materials* **2016**, *6* (13), 1600330.

[143] Peng, J.; Kremer, F.; Walter, D.; Wu, Y.; Ji, Y.; Xiang, J.; Liu, W.; Duong, T.; Shen, H.; Lu, T.; Brink, F.; Zhong, D.; Li, L.; Lem, O. L. C.; Liu, Y.; Weber, K. J.; White, T. P.; Catchpole, K. R. Centimetre-Scale Perovskite Solar Cells with Fill Factors of More than 86 per Cent. *Nature* **2022**, *601* (7894), 573–578.

[144] Duong, T.; Pham, H.; Kho, T. C.; Phang, P.; Fong, K. C.; Yan, D.; Yin, Y.; Peng, J.; Mahmud, M. A.; Gharibzadeh, S.; Nejand, B. A.; Hossain, I. M.; Khan, M. R.; Mozaffari, N.; Wu, Y.; Shen, H.; Zheng, J.; Mai, H.; Liang, W.; Samundsett, C. High Efficiency Perovskite-Silicon Tandem Solar Cells: Effect of Surface Coating versus Bulk Incorporation of 2D Perovskite. *Advanced Energy Materials* **2020**, *10* (9), 1903553.

[145] Peng, J.; Wu, Y.; Ye, W.; Jacobs, D. A.; Shen, H.; Fu, X.; Wan, Y.; Duong, T.; Wu, N.; Barugkin, C.; Nguyen, H. T.; Zhong, D.; Li, J.; Lu, T.; Liu, Y.; Lockrey, M. N.; Weber, K. J.; Catchpole, K. R.; White, T. P. Interface Passivation Using Ultrathin Polymer–Fullerene Films for High-Efficiency Perovskite Solar Cells with Negligible Hysteresis. *Energy & Environmental Science* **2017**, *10* (8), 1792–1800.

[146] Long, C.; Huang, K.; Chang, J.; Zuo, C.; Gao, Y.; Luo, X.; Liu, B.; Xie, H.; Chen, Z.; He, J.; Huang, H.; Gao, Y.; Ding, L.; Yang, J. Creating a Dual-Functional 2D Perovskite Layer at the Interface to Enhance the Performance of Flexible Perovskite Solar Cells. *Small* **2021**, *17* (32), 2102368.

[147] Choi, E.; Lee, J.; Anaya, M.; Mirabelli, A.; Shim, H.; Strzalka, J.; Lim, J.; Yun, S.; Dubajić, M.; Lim, J.; Seidel, J.; Agbenyeke, R. E.; Kim, C. G.; Jeon, N. J.; Soufiani, A. M.; Park, H. H.; Yun, J. S. Synergetic Effect of Aluminum Oxide and Organic Halide Salts on Two-Dimensional Perovskite Layer Formation and Stability Enhancement of Perovskite Solar Cells. *Advanced Energy Materials* **2023**, *13* (39), 2301717.

[148] Zai, S.; Han, R.; Zhao, W.; Ma, C.; Huang, W.; Liu, S. Room-Temperature Molten

Salt-Mediated $CsPbI_3$ Growth for Excellent Photovoltaic Performance. *Advanced Energy Materials* **2023**, *14* (1), 2303264.

[149] Sbeta, M.; Atilgan, A.; Atli, A.; Yildiz, A. Influence of the Spin Acceleration Time on the Properties of ZnO:Ga Thin Films Deposited by Sol–Gel Method. *Journal of Sol-Gel Science and Technology* **2018**, *86* (2), 513–520.

[150] Yang, S.; Song, X.; Gao, L.; Wang, N.; Ding, X.; Wang, S.; Ma, T. Seamless Interfacial Formation by Solution-Processed Amorphous Hydroxide Semiconductor for Highly Efficient Electron Transport. *ACS Applied Energy Materials* **2018**, *1* (9), 4564–4571.

[151] Ke, W.; Zhao, D.; Xiao, C.; Wang, C.; Cimaroli, A. J.; Grice, C. R.; Yang, M.; Li, Z.; Jiang, C.-S.; Al-Jassim, M.; Zhu, K.; Kanatzidis, M. G.; Fang, G.; Yan, Y. Cooperative Tin Oxide Fullerene Electron Selective Layers for High-Performance Planar Perovskite Solar Cells. *Journal of Materials Chemistry A* **2016**, *4* (37), 14276–14283.

[152] Jiang, Q.; Zhang, X.; You, J. SnO_2: A Wonderful Electron Transport Layer for Perovskite Solar Cells. *Small* **2018**, *14* (31), 1801154.

[153] Park, S. Y.; Zhu, K. Advances in SnO_2 for Efficient and Stable N–I–P Perovskite Solar Cells. *Advanced Materials* **2022**, *34* (27), 2110438.

[154] Chen, J.; Zhao, X.; Kim, S.; Park, N. Multifunctional Chemical Linker Imidazoleacetic Acid Hydrochloride for 21% Efficient and Stable Planar Perovskite Solar Cells. *Advanced Materials* **2019**, *31* (39), 1902902.

[155] Ren, X.; Liu, Y.; Lee, D. G.; Kim, W. B.; Han, G. S.; Jung, H. S.; Liu, S. (Frank). Chlorine-Modified SnO_2 Electron Transport Layer for High-Efficiency Perovskite Solar Cells. *InfoMat* **2019**, *2* (2), 401–408.

[156] Liu, X.; Zhang, Y.; Shi, L.; Liu, Z.; Huang, J.; Yun, J. S.; Zeng, Y.; Pu, A.; Sun, K.; Hameiri, Z.; Stride, J. A.; Seidel, J.; Green, M. A.; Hao, X. Exploring Inorganic Binary Alkaline Halide to Passivate Defects in Low-Temperature-Processed Planar-Structure Hybrid Perovskite Solar Cells. *Advanced Energy Materials* **2018**, *8* (20), 1800138.

[157] Liu, Z.; Deng, K.; Hu, J.; Li, L. Coagulated SnO_2 Colloids for High-Performance Planar Perovskite Solar Cells with Negligible Hysteresis and Improved Stability. *Angewandte Chemie* **2019**, *131* (33), 11621–11628.

[158] Wang, P.; Chen, B.; Li, R.; Wang, S.; Ren, N.; Li, Y.; Mazumdar, S.; Shi, B.; Zhao, Y.; Zhang, X. Cobalt Chloride Hexahydrate Assisted in Reducing Energy Loss in Perovskite Solar Cells with Record Open-Circuit Voltage of 1.20 V. *ACS Energy Letters* **2021**, *6* (6), 2121–2128.

[159] You, S.; Zeng, H.; Ku, Z.; Wang, X.; Wang, Z.; Rong, Y.; Zhao, Y.; Zheng, X.; Luo, L.; Li, L.; Zhang, S.; Li, M.; Gao, X.; Li, X. Multifunctional Polymer-Regulated SnO_2 Nanocrystals Enhance Interface Contact for Efficient and Stable

Planar Perovskite Solar Cells. *Advanced Materials* **2020**, *32* (43), 2003990.

[160] Dong, Q.; Zhu, C.; Chen, M.; Jiang, C.; Guo, J.; Feng, Y.; Dai, Z.; Yadavalli, S. K.; Hu, M.; Cao, X.; Li, Y.; Huang, Y.; Liu, Z.; Shi, Y.; Wang, L.; Padture, N. P.; Zhou, Y. Interpenetrating Interfaces for Efficient Perovskite Solar Cells with High Operational Stability and Mechanical Robustness. *Nature Communications* **2021**, *12* (1), 973.

[161] Zheng, Z.; Li, F.; Gong, J.; Ma, Y.; Gu, J.; Liu, X.; Chen, S.; Liu, M. Pre-Buried Additive for Cross-Layer Modification in Flexible Perovskite Solar Cells with Efficiency Exceeding 22%. *Advanced Materials* **2022**, *34* (21), 2109879.

[162] Chung, J.; Shin, S. S.; Hwang, K.; Kim, G.; Kim, K. W.; Lee, D. S.; Kim, W.; Ma, B. S.; Kim, Y.-K.; Kim, T.-S.; Seo, J. Record-Efficiency Flexible Perovskite Solar Cell and Module Enabled by a Porous-Planar Structure as an Electron Transport Layer. *Energy & Environmental Science* **2020**, *13* (12), 4854–4861.

[163] Xiong, L.; Qin, M.; Chen, C.; Wen, J.; Yang, G.; Guo, Y.; Ma, J.; Zhang, Q.; Qin, P.; Li, S.; Fang, G. Fully High-Temperature-Processed SnO_2 as Blocking Layer and Scaffold for Efficient, Stable, and Hysteresis-Free Mesoporous Perovskite Solar Cells. *Advanced Functional Materials* **2018**, *28* (10), 1706276.

[164] Huang, K.; Feng, X.; Li, H.; Long, C.; Liu, B.; Shi, J.; Meng, Q.; Weber, K.; Duong, T.; Yang, J. Manipulating the Migration of Iodine Ions via Reverse-Biasing for Boosting Photovoltaic Performance of Perovskite Solar Cells. *Advanced Science* **2022**, *9* (35), 2204163.

[165] Bu, T.; Li, J.; Zheng, F.; Chen, W.; Wen, X.; Ku, Z.; Peng, Y.; Zhong, J.; Cheng, Y.-B.; Huang, F. Universal Passivation Strategy to Slot-Die Printed SnO_2 for Hysteresis-Free Efficient Flexible Perovskite Solar Module. *Nature Communications* **2018**, *9* (1), 4609.

[166] Li, Y.; Meng, J.; Duan, P.; Wu, R.; Shi, Y.; Zhang, L.; Yan, C.; Deng, J.; Zhang, X. Transport Layer Engineering by Hydrochloric Acid for Efficient Perovskite Solar Cells with a High Open-Circuit Voltage. *ACS Applied Materials & Interfaces* **2023**, *15* (19), 23208–23216.

[167] Xiong, L.; Guo, Y.; Wen, J.; Liu, H.; Yang, G.; Qin, P.; Fang, G. Review on the Application of SnO_2 in Perovskite Solar Cells. *Advanced Functional Materials* **2018**, *28* (35), 1802757.

[168] Min, H.; Kim, M.; Lee, S.-U.; Kim, H.; Kim, G.; Choi, K.; Lee, J. H.; Seok, S. I. Efficient, Stable Solar Cells by Using Inherent Bandgap of α-Phase Formamidinium Lead Iodide. *Science* **2019**, *366* (6466), 749–753.

[169] Han, Q.; Bae, S.; Sun, P.; Hsieh, Y.; Yang, Y. (Michael); Rim, Y. S.; Zhao, H.; Chen, Q.; Shi, W.; Li, G.; Yang, Y. Single Crystal Formamidinium Lead Iodide ($FAPbI_3$): Insight into the Structural, Optical, and Electrical Properties. *Advanced Materials* **2016**, *28* (11), 2253–2258.

[170] Ding, C.; Yin, L.; Wang, J.; Larini, V.; Zhang, L.; Huang, R.; Nyman, M.; Zhao, L.; Zhao, C.; Li, W.; Luo, Q.; Shen, Y.; Österbacka, R.; Grancini, G.; Yang, J. Boosting Perovskite Solar Cells Efficiency and Stability: Interfacial Passivation of Crosslinked Fullerene Eliminates the "Burn-In" Decay. *Advanced Materials* **2022**, *35* (2), 2207656.

[171] Lin, Y.-H.; Sakai, N.; Da, P.; Wu, J.; Sansom, H. C.; Ramadan, A. J.; Mahesh, S.; Liu, J.; Oliver, R. D. J.; Lim, J.; Aspitarte, L.; Sharma, K.; Madhu, P. K.; Morales-Vilches, A. B.; Nayak, P. K.; Bai, S.; Gao, F.; Grovenor, C. R. M.; Johnston, M. B.; Labram, J. G. A Piperidinium Salt Stabilizes Efficient Metal-Halide Perovskite Solar Cells. *Science* **2020**, *369* (6499), 96–102.

[172] Min, H.; Lee, D. Y.; Kim, J.; Kim, G.; Lee, K. S.; Kim, J.; Paik, M. J.; Kim, Y. K.; Kim, K. S.; Kim, M. G.; Shin, T. J.; Seok, S. I. Perovskite Solar Cells with Atomically Coherent Interlayers on SnO_2 Electrodes. *Nature* **2021**, *598* (7881), 444–450.

[173] Zhang, T.; Wang, F.; Kim, H.-B.; Choi, I.; Wang, C.; Cho, E.; Konefal, R.; Puttisong, Y.; Terado, K.; Kobera, L.; Chen, M.; Yang, M.; Bai, S.; Yang, B.; Suo, J.; Yang, S.-C.; Liu, X.; Fu, F.; Yoshida, H.; Chen, W. Ion-Modulated Radical Doping of Spiro-OMeTAD for More Efficient and Stable Perovskite Solar Cells. *Science* **2022**, *377* (6605), 495–501.

[174] Chen, J.; Dong, H.; Li, J.; Zhu, X.; Xu, J.; Pan, F.; Xu, R.; Xi, J.; Jiao, B.; Hou, X.; NG, K. W.; Wang, S.-P.; Wu, Z. Solar Cell Efficiency Exceeding 25% through Rb-Based Perovskitoid Scaffold Stabilizing the Buried Perovskite Surface. *ACS Energy Letters* **2022**, *7* (10), 3685–3694.

[175] Wang, H.; Ye, F.; Liang, J.; Liu, Y.; Hu, X.; Zhou, S.; Chen, C.; Ke, W.; Tao, C.; Fang, G. Pre-Annealing Treatment for High-Efficiency Perovskite Solar Cells via Sequential Deposition. *Joule* **2022**, *6* (12), 2869–2884.

[176] Shi, P.; Ding, Y.; Ding, B.; Xing, Q.; Kodalle, T.; Sutter-Fella, C. M.; Yavuz, I.; Yao, C.; Fan, W.; Xu, J.; Tian, Y.; Gu, D.; Zhao, K.; Tan, S.; Zhang, X.; Yao, L.; Dyson, P. J.; Slack, J. L.; Yang, D.; Xue, J. Oriented Nucleation in Formamidinium Perovskite for Photovoltaics. *Nature* **2023**, *620* (7973), 323–327.

[177] Huang, Z.; Bai, Y.; Huang, X.; Li, J.; Wu, Y.; Chen, Y.; Li, K.; Niu, X.; Li, N.; Liu, G.; Yu, Z.; Zai, H.; Chen, Q.; Lei, T.; Wang, L.; Zhou, H. Anion–π Interactions Suppress Phase Impurities in $FAPbI_3$ Solar Cells. *Nature* **2023**, *623*, 531–537.

[178] Luo, C.; Zheng, G.; Gao, F.; Wang, X.; Zhan, C.; Gao, X.; Zhao, Q. Engineering the Buried Interface in Perovskite Solar Cells via Lattice-Matched Electron Transport Layer. *Nature Photonics* **2023**, *17*, 856–864.

[179] Shen, L.; Song, P.; Zheng, L.; Wang, L.; Zhang, X.; Liu, K.; Liang, Y.; Tian, W.; Luo, Y.; Qiu, J.; Tian, C.; Xie, L.; Wei, Z. Ion-Diffusion Management Enables All-Interface Defect Passivation of Perovskite Solar Cells. *Advanced Materials*

2023, *35* (39), 2301624.

[180] Wang, Q.; Chen, Y.; Chen, X.; Tang, W.; Qiu, W.; Xu, X.; Wu, Y.; Peng, Q. Tailored Succinic Acid-Derived Molecular Structures toward 25.41%-Efficiency and Stable Perovskite Solar Cells. *Advanced Materials* **2023**, 2307709.

[181] Wang, Y.; Feng, M.; Chen, H.; Ren, M.; Wang, H.; Miao, Y.; Chen, Y.; Zhao, Y. Highly Crystalized Cl-Doped SnO_2 Nanocrystals for Stable Aqueous Dispersion toward High-Performance Perovskite Photovoltaics. *Advanced Materials* **2023**, *36* (5), 2305849.

[182] Yang, H.; Xu, T.; Chen, W.; Wu, Y.; Guo, X.; Shen, Y.; Ding, C.; Chen, X.; Chen, H.; Ding, J.; Wu, X.; Zeng, G.; Zhang, Z.; Li, Y.; Li, Y. Iodonium Initiators: Paving the Air-Free Oxidation of Spiro-OMeTAD for Efficient and Stable Perovskite Solar Cells. *Angewandte Chemie International Edition* **2023**, *63* (5), e202316183.

[183] Guo, H.; Xiang, W.; Fang, Y.; Li, J.; Lin, Y. Molecular Bridge on Buried Interface for Efficient and Stable Perovskite Solar Cells. *Angewandte Chemie* **2023**, *62* (34), e202304568.

[184] Chen, T.; Xie, J.; Wen, B.; Yin, Q.; Lin, R.; Zhu, S.; Gao, P. Inhibition of Defect-Induced α-to-δ Phase Transition for Efficient and Stable Formamidinium Perovskite Solar Cells. *Nature Communications* **2023**, *14* (1), 6125.

[185] Zhao, W.; Guo, P.; Liu, C.; Jia, N.; Fang, Z.; Ye, L.; Ye, Q.; Xu, Y.; Glotov, A. P.; Novikov, A. A.; Vinokurov, V. A.; Harvey, D.; Shchukin, D.; Wang, H. Laser Derived Electron Transport Layers with Embedded P–N Heterointerfaces Enabling Planar Perovskite Solar Cells with Efficiency over 25%. *Advanced Materials* **2023**, *35* (31), 2300403.

[186] Ye, F.; Tian, T.; Su, J.; Jiang, R.; Li, J.; Jin, C.; Tong, J.; Bai, S.; Huang, F.; Müller-Buschbaum, P.; Cheng, Y.; Bu, T. Tailoring Low-Dimensional Perovskites Passivation for Efficient Two-Step-Processed $FAPbI_3$ Solar Cells and Modules. *Advanced Energy Materials* **2023**, *14* (4), 2302775.

[187] Gao, Z.-W.; Wang, Y.; Chen, X.; Jiang, Z.; Qin, M.; Ning, W.; Hu, B.; Lu, X.; Yin, W.-J.; Yang, D.; Xu, B.; Choy, W. C. H. Reconstructing Subsurface Lattice for Stable Perovskite Photovoltaics. *Joule* **2023**, *8* (1), 255–266.

[188] Zhang, Y.; Yang, T.; Lee, S.-U.; Liu, S.; Zhao, K.; Park, N.-G. Stabilizing α-Phase $FAPbI_3$ Perovskite Induced by an Ordered Solvated Quasi-Crystalline PbI_2. *ACS Energy Letters* **2023**, *9* (1), 159–167.

[189] Peng, J.; Walter, D.; Ren, Y.; Tebyetekerwa, M.; Wu, Y.; Duong, T.; Lin, Q.; Li, J.; Lu, T.; Mahmud, M. A.; Lem, O. L. C.; Zhao, S.; Liu, W.; Liu, Y.; Shen, H.; Li, L.; Kremer, F.; Nguyen, H. T.; Choi, D.-Y.; Weber, K. J. Nanoscale Localized Contacts for High Fill Factors in Polymer-Passivated Perovskite Solar Cells. *Science* **2021**, *371* (6527), 390–395.

[190] Peng, W.; Mao, K.; Cai, F.; Meng, H.; Zhu, Z.; Li, T.; Yuan, S.; Xu, Z.; Feng, X.; Xu, J.; McGehee, M. D.; Xu, J. Reducing Nonradiative Recombination in Perovskite Solar Cells with a Porous Insulator Contact. *Science* **2023**, *379* (6633), 683–690.

[191] Muhammad, B. T.; Kar, S.; Stephen, M.; Leong, W. L. Halide Perovskite-Based Indoor Photovoltaics: Recent Development and Challenges. *Materials Today Energy* **2022**, *23*, 100907.

[192] Ding, Y.; Ding, B.; Kanda, H.; Usiobo, O. J.; Gallet, T.; Yang, Z.; Liu, Y.; Huang, H.; Sheng, J.; Liu, C.; Yang, Y.; Queloz, V. I. E.; Zhang, X.; Audinot, J.-N.; Redinger, A.; Dang, W.; Mosconic, E.; Luo, W.; Angelis, F. D.; Wang, M. Single-Crystalline TiO_2 Nanoparticles for Stable and Efficient Perovskite Modules. *Nature Nanotechnology* **2022**, *17* (6), 598–605.

[193] Zhu, P.; Chen, C.; Dai, J.; Zhang, Y.; Mao, R.; Chen, S.; Huang, J.; Zhu, J. Towards the Commercialization of Perovskite Solar Modules. *Advanced Materials* **2024**, 2307357.

[194] Xu, Z.; Bristow, H.; Babics, M.; Vishal, B.; Aydin, E.; Azmi, R.; Ugur, E.; Yildirim, B. K.; Liu, J.; Kerner, R. A.; Wolf, S. D.; Rand, B. P. Reverse-bias resilience of monolithic perovskite/silicon tandem solar cells. *Joule* **2023**, *7* (9), 1992–2002.

[195] Bogachuk, D.; Feldmann, F.; Do perovskites need silicon to be stable under reverse bias? *Joule* **2023**, *7* (11), 2423–2426.

Achievements

1. Articles

[1] Weiqi Li†, **Keqing Huang† (co-first author)**, Jianhui Chang, Caiqi Hu, Caoyu Long, Hai Zhang, Xavier Maldague, Biao Liu, Jianqiao Meng, Yuxia Duan*, Junliang Yang*, Sparkling hot spots in perovskite solar cells under reverse bias, *ChemPhysMater* **2022**, *1*, 71–76.

[2] **Keqing Huang**†, Xiangxiang Feng†, Hengyue Li, Caoyu Long, Biao Liu, Jiangjian Shi, Qingbo Meng, Klaus Weber, The Duong*, Junliang Yang*, Manipulating the Migration of Iodine Ions via Reverse-Biasing for Boosting Photovoltaic Performance of Perovskite Solar Cells, *Adv. Sci.*, **2022**, *9*, 2204163.

[3] **Keqing Huang**, Lichun Chang, Yihui Hou, Wenzhong Ji, Thanh Tran-Phu, Anh Dinh Bui, Azul Osorio Mayon, Wei Wang, Olivier Lee Cheong Lem, Dang-Thuan Nguyen, Grace Dansoa Tabi, Leiping Duan, Yun Liu, Heping Shen, Junliang Yang, Thomas P. White, Kylie R. Catchpole, Klaus J. Weber*, The Duong*, Universal Strategy with Structural and Chemical Crosslinking Interface for Efficient and Stable Perovskite Solar Cells, *Adv. Energy Mater.*, **2024**, *14*, 2304073.

[4] **Keqing Huang**†, Kaixin Yang†, Hengyue Li, Shuaizhi Zheng, Jinbin Wang, Hongxia Guo, Yongyi Peng, Xiangli Zhong*, Junliang Yang*, *γ*-ray Radiation on Flexible Perovskite Solar Cells, *ACS Appl. Energy Mater.*, **2020**, *3*, 7318-7324.

[5] Caoyu Long†, Ning Wang†, **Keqing Huang† (co-first author)**, Hengyue Li, Biao Liu, Junliang Yang*, Two-step processed efficient perovskite solar cells via improving perovskite/PTAA interface using solvent engineering in PbI_2 precursor, *Chin. Phys. B* **2020**, *29*, 048801.

[6] Hengyue Li, Xiangxiang Feng, **Keqing Huang**, Siyuan Lu, Xinyue Wang, Erming Feng, Jianhui Chang, Caoyu Long, Yuanji Gao, Zhihui Chen, Chenyi Yi, Jun He, Junliang Yang*, Constructing Additives Synergy Strategy to Doctor-Blade Efficient $CH_3NH_3PbI_3$ Perovskite Solar Cells under a Wide Range of Humidity from 45% to 82%, *Small* **2023**, *19*, 2300374.

[7] The Duong*, Thuan Nguyen, **Keqing Huang**, Huyen Pham, Sunita Gautam Adhikari, Motiur Rahman Khan, Leiping Duan, Wensheng Liang, Kean Chern Fong, Heping Shen, Anh Dinh Bui, Azul Osorio Mayon, Thien Truong, Grace Tabi, Viqar Ahmad, Sachin Surve, Jingnan Tong, Teng Kho, Thanh Tran-Phu, Teng Lu, Jianghui Zheng, Ulrich W. Paetzold, Uli Lemmer, Anita Ho Baillie, Yun Liu, Gunther Andersson, Thomas White, Klaus Weber, Kylie Catchpole, Bulk Incorporation with 4-Methylphenethylammonium Chloride for Efficient and Stable Methylammonium-Free Perovskite and Perovskite-Silicon Tandem Solar Cells, *Adv. Energy Mater.*, **2023**, *13*, 2203607.

[8] Erming Feng, Yunfei Han, Jianhui Chang, Hengyue Li, **Keqing Huang**, Lixiu Zhang, Qun Luo, Jidong Zhang, Changqi Ma, Yingping, Zou, Liming Ding*, Junliang Yang*, 26.75 cm^2 organic solar modules demonstrate a certified efficiency of 14.34%, *J. Semicond.*, **2022**, *43*, 100501.

[9] Yuanji Gao, Xiangxiang Feng, Jianhui Chang, Caoyu Long, Yang Ding, Hengyue Li, **Keqing Huang**, Biao Liu, Junliang Yang*, Surface ion exchange and targeted passivation with cesium fluoride for enhancing the efficiency and stability of perovskite solar cells, *Appl. Phys. Lett.*, **2022**, *121*, 073902.

[10] Yuanji Gao, **Keqing Huang**, Caoyu Long, Yang Ding, Jianhui Chang, Dou Zhang, Lioz Etgar, Mingzhen Liu, Jian Zhang, Junliang Yang*, Flexible Perovskite Solar Cells: From Materials and Device Architectures to Applications, *ACS Energy Lett.*, **2022**, *7*, 1412–1445.

[11] Yang Xiang, Xindi Mo, Xing Li, **Keqing Huang**, Pei He, Guozhang Dai*, Junliang Yang, Progress on growth of metal halide perovskites by vapor-phase synthesis and their applications, *J. Phys. D: Appl. Phys.*, **2021**, *55*, 073001.

[12] Yameen Ahmed, Bilawal Khan, M. Bilal Faheem, **Keqing Huang**, Yuanji Gao, Junliang Yang*, Progress on growth of metal halide perovskites by vapor-phase synthesis and their applications, *J. Energy Chem.*, **2022**, *67*, 361–390.

[13] Caoyu Long, **Keqing Huang**, Jianhui Chang, Chuantian Zuo, Yuanji Gao, Xin Luo, Biao Liu, Haipeng Xie, Zhihui Chen, Jun He, Han Huang, Yongli Gao, Liming Ding*, Junliang Yang*, Creating a Dual-Functional 2D Perovskite Layer at the Interface to Enhance the Performance of Flexible Perovskite Solar Cells, *Small* **2021**, *17*, 2102368.

[14] Hengyue Li, **Keqing Huang**, Yanan Dong, Xiaotong Guo, Yu Yang, Qun Luo, Chang-Qi Ma, Dongfan Li, Guanghao Lu, Jian Xiong, Jian Zhang, Yingguo Yang, Xingyu Gao, Junliang Yang*, Efficient organic solar cells with the active layer fabricated from glovebox to ambient condition, *Appl. Phys. Lett.*, **2020**, *117*, 133301.

[15] Yongyi Peng, Feilong Zeng, Yudiao Cheng, Chunhua Wang, **Keqing Huang**, Pengshan Xie, Haipeng Xie, Yongli Gao, Junliang Yang, Fully Doctor-bladed efficient perovskite solar cells in ambient condition via composition engineering, *Org. Electron.*, **2020**, *83*, 105736.

2. Conference

[1] Asia-Pacific Solar Research Conference, 5-7, December, 2023.

[2] The 10th Conference on Science and Technology of Emerging Solar Energy Materials, 5-7, May, 2023.

3. Award

[1] 2022 Chinese Government Award for Outstanding Self-financed Students Abroad.